Universidad Nacional Autónoma de México
Posgrado en Astrofísica
Instituto de Astronomía

Análisis Cinemático y Químico de Nebulosas Planetarias en NGC 6822 y NGC 3109

Tesis

que para optar por el grado de:

doctor en ciencias (astrofísica)

Presenta:
Sheila Nathanya Flores Durán

Directora de tesis:

Dra. Miriam del Carmen Peña Cárdenas
Instituto de Astronomía

Ciudad Universitaria, Cd. Mx. Agosto 2017

Análisis Cinemático y Químico de Nebulosas Planetarias en NGC 6822 y NGC 3109

Sheila Nathanya Flores Durán

Recopilación de Artículos

Agosto 2017

"In the beginning there was nothing, which exploded."

Terry Pratchet

Este trabajo de investigación se ha podido realizar gracias a una beca de posgrado por la Comisión Nacional de Ciencia y Tecnología, CONACyT México. También está financiado por DGAPA-PAPIIT mediante los proyectos IN-105511 e IN-109614.

Agradecimientos

Miriam gracias por compartir conmigo tu sabiduría, por tu enorme paciencia y gracias por el apoyo que me haz brindado todos estos años.

A todos los miembros del jurado Alberto López, Silvana Navaro, Gerado Ramos, Jorge García Rojas, y Gloria Delgado Inglada por darme su tiempo revisando este trabajo y por sus invaluable comentarios.

Querida familia sin ustedes no sé que haría, son mi apoyo incondicional. Están siempre presentes en mi corazón, los amo.

Le agradezco a todos mis amigos por compartir conmigo mÃ¡s de una cerveza, por todas las rodadas y por todas las buenas charlas. Gracias por ayudarme a mantener la cordura.

A la máxima casa de estudios la UNAM, mi segundo hogar. Al Instituto de Astronomía que me enseño el verdadero camino a las estrellas. A todos los que llevan este posgrado, que siempre están al pendiente de nosotros, en especial a Leti Carigi, Bertha Vázquez y Heike Breunig.

Acrónimos

AGB	Rama asintótica de las gigantes
AP	Ángulo de posición
CG	Cúmulo Globular
dIrr	Galaxia irregular enana
GL	Grupo Local
GTC	Gran Telescopio de Canarias
H-R	Hertzsprung-Russel
ICF	Factores de corrección por ionización
KINCAT	Kinematic Catalogue: Extragalactic Planetary Nebulae
LCO	Observatorio de las Campanas
ΛCDM	Lambda-Cold Dark-Matter
MES	Manchester Echelle Spectrometer
MI	Medio interestelar
MIKE	Magellan Inamori Kyocera Echelle
NP	Nebulosa planetaria
NPs	Nebulosas planetarias
OSIRIS	Optical System for Imaging and low-Intermediate-Resolution Integrated Spectroscopy
SMC	Nube menor de Magallanes
SPM	San Pedro Mártir

Resumen

La cinemática y la química de las Nebulosas Planetarias (NPs) en galaxias externas y en la nuestra, es clave para entender el comportamiento de estrellas de masa baja-intermedia y su relación con otros componentes de las galaxias. Es posible estudiarlas gracias a la gran intensidad de sus líneas en emisión. A partir de la obtención de espectros profundos de las NPs es posible estudiar su comportamiento cinemático y determinar su composición química. Para esta tesis se obtuvieron datos espectroscópicos de alta resolución de varias NPs y regiones H II pertenecientes a dos galaxias enanas irregulares (dIrr) NGC 6822 y NGC 3109.

El objetivo principal de la tesis es analizar la relación cinemática entre las NPs y los discos de H I pertenecientes a NGC 6822 y NGC 3109. Conjuntamente se estudió la cinemática de regiones H II. Así fue posible describir la relación cinemática de dos tipos diferentes de poblaciones estelares con los discos de gas H I. Los datos de alta resolución utilizados para medir las velocidades radiales de las NPs y regiones H II tienen una buena precisión, en el caso de NGC 6822 presentan errores de 5-6 km s^{-1} y para NGC 3109 los errores son mejores que 7.8 km s^{-1}. También se estudió la composición química de NPs y regiones H II de estas dos galaxias, en algunos casos a partir de nuevas observaciones y también a través de una revisión de la literatura, y se comparó con modelos de evolución estelar. Esta información en conjunto revela la conexión cinemática y química que existe entre las distintas poblaciones estelares y sus galaxias.

Para ambas galaxias, los datos espectroscópicos de alta resolución fueron obtenidos con dos espectrógrafos. El primero es el Magellan Inamori Kyocera Echelle (MIKE) en el telescopio Magallanes de 6.5 m del Observatorio de las Campanas (LCO), Chile. El se-

gundo es el Manchester Echelle Spectrometer (MES) en el telescopio de 2.1 m en el Observatorio Astronómico Nacional (OAN) en San Pedro Mártir (SPM), México. Únicamente para el análisis de la composición química de las NPs de NGC 6822 se obtuvieron datos de baja resolución con el Optical System for Imaging and low-Intermediate-Resolution Integrated Spectroscopy (OSIRIS) en el Gran Telescopio de Canarias (GTC).

Los resultados más importantes obtenidos fueron:

En NGC 6822 la cinemática de las NPs muestran un comportamiento cinemático distinto al del disco de H I y más similar al del elipsoide de estrellas de C, de edad intermedia. Las regiones H II siguen el comportamiento cinemático del gas H I. Las NPs presentan composiciones químicas variadas, desde objetos pobres, 12+log O/H = 7.4 hasta objetos con abundancias similares a la población de regiones H II en la galaxia, 12+log O/H = 8.2.

En NGC 3109 la cinemática de las NPs concuerda con la de regiones H II y del disco de H I. Sus abundancias son anómalas en el sentido de que muestran abundancias de O/H mayores por 0.43 dex que la de regiones H II cuyo valor es de 12+log O/H = 7.74.

La presente tesis es una compilación de los artículos que fueron publicados durante la realización de mi doctorado.

Artículos publicados y aquí presentados:

a) Kinematic study of planetary nebulae in NGC 6822. S. N. Flores-Durán, M. Peña, L. Hernández-Martínez, J. García-Rojas, & M. T. Ruiz. *A&A* **2014**, *568*, A82.

b) The planetary nebulae and H II regions in NGC 6822 revisited. J. García-Rojas, M. Peña, S. N. Flores-Durán, and L. Hernández-Martínez. **2016**, *A&A 586*, A59.

c) Kinematic and chemical study of planetary nebulae and H II regions in NGC 3109. S. N. Flores-Durán, M. Peña, and M. T. Ruiz. Aceptado **2017**. *A&A 601*, A147.

Índice general

1

Introducción

En esta sección daremos una breve descripción de las NPs, su formación y su existencia en otras galaxias. También se presenta a las dos galaxias del interés de este trabajo, NGC 6822 y NGC 3109.

1.1. Las Nebulosas Planetarias

La primera NP fue observada en 1764 por Charles Messier quien le asignó el número 27 en su catálogo, esta NP también es conocida como la nebulosa Dumbbell. En la versión final del catálogo de Messier (1784) se encuentran 4 NPs. El nombre fue introducido por William Herschell en 1785, quien observo que la apariencia de estos objetos se asemejaba a un disco verdoso, como lo que se veía al observar un planeta. En su apariencia las NPs se distinguen de otros objetos nebulosos porque tienen una estructura bien definida y a menudo se les asocia una estrella central. La diferencia con otros objetos es evidente al obtener su espectro, el cual está dominado por líneas de emisión intensas y delgadas.

En sus espectros encontramos las líneas de recombinación como las del hidrógeno, el helio y algunas líneas débiles de otros elementos y líneas de emisión por excitación colisional, siendo estas las más dominantes. Entre estas podemos encontrar las líneas de emisión de [O III] λ5007, [N II] λ6583, [Ne III]λ 3869, [S II]λ6717 y [Ar III]λ7136 entre otras.

El análisis de sus espectros nos da información sobre la cinemática, la temperatura y densidad electrónica del gas, así como de la abundancia de los elementos. Utilizando el corrimiento Doppler de las líneas de emisión es posible determinar las velocidades radiales de estos objetos. La temperatura electrónica puede aproximarse usando el diagnóstico [O III] (λ4959 + λ5007)/λ4363 o [N II] (λ6548 + λ6583)/λ5755 por ejemplo. Los mejores ejemplos de líneas que pueden ser usadas para medir la densidad electrónica son [O II] λ3729/λ3726 y [S II] λ6716/λ6731.

La temperatura electrónica característica de una NP es del orden de 10^4 K. La densidad del gas de la nebulosa es muy baja, puede variar desde 10^5 cm^{-3} para objetos compactos y 1 cm^{-3} para nebulosas muy extendidas. A partir del corrimiento Doppler de sus líneas, se encuentra que el gas se expande a velocidades típicas entre 10-30 km

s^{-1} (Schönberner et al., 2010; Pereyra et al., 2013), por lo que se espera que se disipen en aproximadamente 30,000 años.

Estudiar las NPs nos da información sobre las poblaciones estelares de masa baja e intermedia. Es posible encontrarlas a grandes distancias tales como 50-100 Mpc (Gerhard et al., 2007; Ventimiglia et al., 2011). Su estudio nos da información precisa sobre la luminosidad, edad, metalicidad, dinámica y la etapa final de la evolución de sus estrellas progenitoras. Es por esto que son muy útiles para probar distintas teorías sobre la evolución de estrellas, galaxias e incluso se pueden utilizar sus propiedades para probar modelos de Lambda-Cold Dark-Matter (ΛCDM) (Coccato et al., 2009; McNeil-Moylan et al., 2012).

1.1.1. Evolución de una estrella de masa baja a intermedia

Las NPs son producidas al final de la evolución de las estrellas cuyas masas van de $\sim$1 $M_\odot$ a $\sim$8 $M_\odot$ (Iben & Renzini, 1983; Dopita et al., 1997) y se estima que las edades de sus estrellas progenitoras se encuentran entre 0.1 y 9 Ga (Allen et al., 1998). Al final de la evolución de una estrella de masa baja-intermedia, su atmósfera es eyectada formando un cascarón y dejando expuesto el núcleo de la estrella. El núcleo remanente tiene una temperatura que va desde 25,000 K hasta 200,000 K y emite radiación ultravioleta capaz de ionizar el cascarón en expansión.

La evolución de las estrellas de masa baja a intermedia y su camino en el diagrama de luminosidad-temperatura es ilustrado en la fig.1.1. Al terminar la fase de secuencia principal en la evolución de estrellas con masa baja a intermedia el núcleo ahora de He comienza a contraerse y el H que se encuentra alrededor se quema en un cascarón. En estrellas de masa $<2M_\odot$ (Osterbrock & Ferland, 2006), en la zona más caliente de este cascarón comienza a quemar el H y progresivamente agrega He al núcleo aumentando su masa. Su luminosidad aumenta, la envolvente de la estrella se expande lentamente y la temperatura efectiva decrece, transformando a la estrella en una gigante roja. en esta etapa la estrella pierde una cantidad significativa de masa de su capas exteriores. El núcleo de He continua contrayéndose y se vuelve degenerado, es decir, la densidad se vuelve lo suficientemente alta haciendo que los átomos se acerquen cada vez más,

de acuerdo con el principio de exclusión de Pauli no pueden existir dos fermiones (en este caso electrones) con el mismo spin en el mismo estado cuántico, entonces los niveles electrónicos de menor energía en los átomos se llenan, aumentando la presión electrónica. Cuando hay degeneración la presión electrónica no depende de la temperatura.

El núcleo rico en He de la estrella se contrae y calienta mientras el cascarón donde se quema el H agrega masa al núcleo hasta que finalmente el núcleo comienza a quemar el He. Esto ocurre cuando la temperatura central alcanza temperaturas típicas alrededor de 10^8 K (Kwok, 2000). Un incremento en la densidad del borde del núcleo y el cascarón, resultado de la contracción del núcleo, incrementa la tasa de la quema de H en el cascarón. Esto envía rápidamente a la estrella a la rama de gigantes rojas (RGB, por sus siglas en inglés). El calor generado por el cascarón calienta el núcleo degenerado hasta el punto en que la fusión del He a C comienza a través del proceso triple alfa (Karttunen et al., 2003).

La quema de He comienza simultáneamente en toda la región central causando un aumento repentino en la temperatura. Al estar degenerado el núcleo no puede expandirse, a pesar de que la temperatura aumenta, y esto conduce a que la tasa de reacciones nucleares aumente. Unos pocos segundos después de que comience la quema de He, hay una explosión conocida como flash de He. El flash termina cuando la temperatura se eleva lo suficiente para hacer que niveles de energía más altos estén disponibles para los electrones, permitiendo que el núcleo se expanda.

Las estrellas más masivas (2 $M_\odot$ <M < $8M_\odot$) no forman núcleos degenerados de He pues su temperatura central es mayor y la densidad menor, por lo que no presentan flash de He. Entonces, la quema He comienza de una manera no catastrófica mientras la región central se contrae (Osterbrock & Ferland, 2006).

Una vez que todo el He del núcleo se ha consumido, este se compone de C y O. El núcleo esta rodeado de un cascarón de He y las capas exteriores de la estrella son de H. Entonces la estrella evoluciona a lo largo de la rama asintótica de las gigantes (AGB, por sus siglas en inglés), en esta etapa su luminosidad aumenta y su temperatura disminuye (Salaris & Cassisi, 2006). En esta época la estrella es más brillante de lo que era en la primer fase de gigante roja.

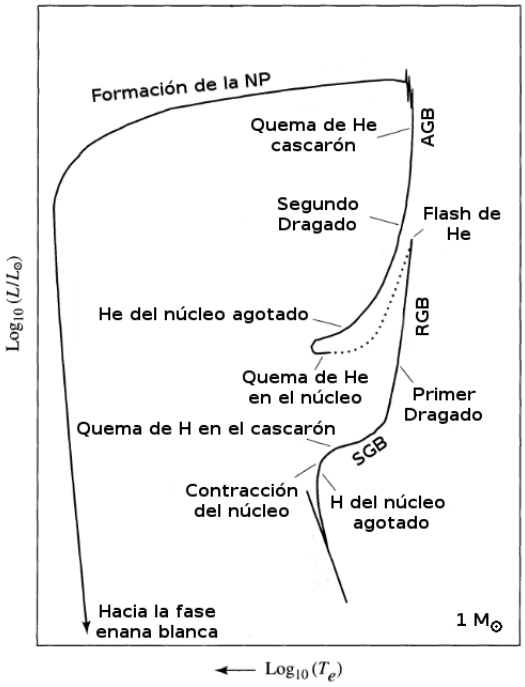

Figura 1.1: Diagrama esquematico de luminosodad-temperatura efectiva que muestra la evolución de una estrella con ∼1 $M_\odot$, después de dejar la secuencia principal. Imagen adaptada de Carroll & Ostlie (2007)

Las estrellas AGB tienen vientos estelares fuertes que causan que la estrella pierda masa a un ritmo acelerado cerca del final de su fase de perdida de masa; hasta $10^{-4} M_\odot$ por año. Este viento es denso y forma una envolvente gaseosa alrededor de la estrella (Kwok, 2000).

La enorme nube que rodea a la estrella AGB continua expandiéndose hasta que se vuelve ópticamente delgada, exponiendo a la estrella central. Durante la etapa final de perdida de masa la envolvente remanente de la estrella es expulsada, mostrando los restos producidos durante su larga historia de reacciones nucleares. Los cascarones remanentes donde se queman H y He son apagados y expulsados con sólo una delgada capa de material dejada ahora encima de la estrella. La envolvente expulsada se observa como una NP, que se mantendrá visible como un cascarón brillante durante un trayecto con

luminosidad casi constante, hacia la izquierda en el diagrama H-R. El núcleo con una temperatura superficial de 30,000 grados y evoluciona hacia temperaturas más altas, alcanzando hasta 200,000 K es expuesto y emite radiación ultravioleta suficientemente intensa para ionizar el cascarón en expansión. La luminosidad del núcleo remanente de la estrella cae rápidamente y enfría gradualmente hasta convertirse en una estrella enana blanca.

1.2. Las Nebulosas Planetarias extragalácticas

Las primeras NPs extragalácticas identificadas en galaxias cercanas fueron identificadas ópticamente en M31 por Baade (1955). Detectó 5 NPs en el suroeste del centro de M31 en [O III]λ5007 con un filtro de rango que va de λ4900 a λ6400 y el telescopio Palomar de 5 m.

El estudio de las NPs en galaxias externas nos da información sobre diversos temas. Sirven como trazadores de la dinámica interna y de la distribución de masa de sus galaxias (Teodorescu et al., 2011), permiten trazar la migración radial en los discos galácticos y dan información sobre los gradientes de metalicidad (Magrini et al., 2016), también permiten conocer la distancia a las galaxias en las que se encuentran a través de la función de luminosidad de las NPs (por ejemplo Kreckel et al. (2017)). En este trabajo se presenta el uso de las las NPs para trazar la cinemática de dos galaxias irregulares (NGC 6822 y NGC 3109) y a partir de su análisis químico se muestra su utilidad para poner a prueba modelos de evolución estelar.

El valor de las NPs como trazadores de la cinemática de objetos extragalácticos fue demostrado por Nolthenius & Ford (1986), combinando mediciones de las velocidades radiales con modelos dinámicos de M32, para determinar las órbitas estelares y la masa de la galaxia. Cada NP es observada como un objeto discreto y es fácil medir su velocidad radial tomando su espectro.

Conocer la composición química de las NPs en galaxias externas nos da información sobre la nucleosíntesis estelar en diferentes condiciones, por ejemplo estudiar la evolución estelar en ambientes con distinta metalicidad (ver, Stasińska et al. (1998);Stasińska et

al. (2013)).

La manera de encontrar NPs extragalácticas es tomar un par de imágenes, una con un filtro en [O III] λ5007 y otra en su contínuo. Cuando se utilizan telescopios en la superficie de la Tierra, las NPs en galaxias más lejanas que las nubes de Magallanes no pueden ser resueltas, se observan como objetos puntuales, entonces en la imagen del contínuo las NPs estarán ausentes mientras que en la imagen de [O III] aparecen muy brillantes. Es posible confundirlas con regiones H II, nebulosas de reflexión, galaxias de emisión entre otros. La identificación definitiva de las NPs se basa en la espectroscopía, ya que éstas presentan líneas de emisión intensas con muy poco o sin continuo. La radiación ionizante de la estrella central de un NP tiene la energía necesaria para que en su espectro se encuentren líneas del He II. El [O III] λ5007 es muy brillante y presentan un cociente de intensidades I(5007)/I(Hα) muy característico, tal que en galaxias con formación estelar el [O III] debe ser al menos 1.6 veces más brillante que Hα (Ciardullo et al., 2002).

En las galaxias del grupo local se conocen muchas NPs (Corradi & Magrini, 2006), entre estas hay algunas galaxias irregulares como LCM, SMC, IC 10, NGC 6822, NGC 3109, Sextans A y Sextans B. La cinemática de las NPs extragalácticas ha sido muy estudiadas en galaxias espirales (ver Herrmann et al. (2009)), elípticas (por ejemplo, Méndez et al. (2009)) y en el medio intracúmulo (por ejemplo, Ventimiglia et al. (2008)). En galaxias irregulares la cinemática de las NPs ha sido menos estudiada. Antes de este trabajo se podía encontrar información para LMC e IC 10. En la LMC (Olsen & Salyk, 2002; Reid & Parker, 2006) reportan que las NPs forman parte de un disco torcido más extenso que el de su disco de H I y con mayor dispersión. En IC 10 encontraron que las NPs tienen un comportamiento cinemático similar al de su disco de H I (Gonçalves et al., 2012).

El análisis de abundancias químicas de NPs extragalácticas es un campo muy estudiado. En particular para NGC 6822 existen varios estudios sobre las abundancias químicas de sus NPs (Richer & McCall, 2007; Hernández-Martínez et al., 2009), modelos sobre la evolución química (Hernández-Martínez et al., 2011). Y para NGC 3109 se reporta la química de sus NPs en Peña et al. (2007).

1.2.1. NGC 6822

En 1884 con un telescopio refractor de 5 pulgadas E. E. Barnard descubrió la galaxia NGC 6822, en sus observaciones la describe como un objeto nebuloso y muy débil. Esta galaxia fue el primer objeto en ser identificado como un sistema que no pertenece a la Vía Láctea (Hubble, 1925). Es una galaxia irregular (dIrr) que pertenece al Grupo Local (GL). Sus coordenadas ecuatoriales son (J2000) AR 19h 44m 56.6s y Dec -14° 48' 04.5". Es comparable en tamaño a la nube menor de Magallanes (SMC) pero con una metalicidad un poco mayor (Muschielok et al., 1999; Venn et al., 2001). Su velocidad sistémica es de -57 ± 2 km s^{-1} (Mateo, 1998; Koribalski et al., 2004).

Se encuentra a una distancia de 460±10 kpc (Mateo, 1998), está localizada en un lugar relativamente aislado del Grupo Local (GL). La forma de esta galaxia en el óptico está dominada por una barra (Hodge, 1977) aproximadamente de 8' de largo y con un ángulo de posición (AP) de 10°. Ha sido catalogada como una galaxia "anillo-polar"(Demers et al., 2006) y se le han determinado al menos dos sistemas dinámicos: el primero, un disco de H I que mide 6×13 kpc (aproximadamente 1° × 2°) con un AP de 110° que muestra rotación de cuerpo rígido (de Blok & Walter, 2000, 2006); (Weldrake et al., 2003). El segundo, corresponde a una gran estructura estelar esferoidal con un AP de 64.5°, compuesto principalmente por estrellas de edad intermedia (Letarte et al., 2002; Battinelli et al., 2006). Este esferoide estelar significativamente más extendido que el disco de H I, fue mapeado por (Battinelli et al., 2006), quienes reportaron un semi eje mayor de 36'; así la distribución de estrellas viejas es esencialmente diferente a la del disco de H I.

En esta galaxia se conocen 26 NPs (Hernández-Martínez & Peña, 2009) y de acuerdo al análisis de sus abundancias químicas (Hernández-Martínez et al., 2009) pertenecen a dos grupos de edades diferentes, uno de NPs jóvenes con edades de 1 a 3 Ga y el segundo de NPs viejas con edades en el rango de 4-9 Ga. Las NPs jóvenes muestran una composición química similar a la del medio interestelar (MI) mientras que las más viejas tienen abundancias menores por un factor de 2. También estudiaron las abundancias en regiones H II y estas muestran que el MI en los 2 kpc alrededor del centro de la galaxia es químicamente homogéneo, con una abundancia de 12+log(O/H) = 8.06±0.04.

1.2.2. NGC 3109

NGC 3109 fue descubierta por John Herschel en 1835. Es una galaxia irregular tipo Magallanica clasificada como una espiral tipo tardío SB(s)m (de Vaucouleurs et al., 1991) que se encuentra en la orilla del GL. Sus coordenadas ecuatoriales son (J2000) RA 10h 03m 06.9s y Dec -26° 09' 34". Es el miembro dominante de un pequeño grupo de galaxias enanas pobres en metales que incluyen Sextans A, Sextans B, y Antlia. Su velocidad sistémica estimada es de 404±2 km s^{-1}.

Esta galaxia posee una estructura compleja, en el óptico parece tener un disco rico en gas rotando y un halo de estrellas viejas (Minniti et al., 1999). Este disco está orientado de costado y asemeja una forma tipo cigarro alineada casi E-O, con una extensión aproximada de 17.4×3.5 arcmin. Posee un enorme disco de H I, que está alineado y rodeando al disco óptico, fue mapeado por Barnes & de Blok (2001), encontrando que el disco está torcido y sugieren que esto puede ser evidencia de un posible encuentro con la galaxia enana Antlia hace aproximadamente 10^9 años. Presenta huellas de una estructura espiral (Demers et al., 1985). De estudios recientes de poblaciones de Ceféidas, Soszyński et al. (2006) derivaron un modulo de distancia de 25.571 ± 0.024 (1.30 ± 0.02 Mpc) en concordancia con resultados previos.

A la distancia de NGC 3109, un arcsec corresponde a 6.4 pc. Típicamente las NPs tienen diámetros más pequeños que 1 pc, por lo que se observan como objetos puntuales.

La cinemática del disco de H I fue presentada con gran detalle por Ott et al. (2012) y analizada extensamente por Carignan et al. (2013), quién amplió el análisis hasta una extensión de 58×27 arcmin. La formación estelar ha estado muy activa en NGC 3109 como indica el gran número de regiones H II que contiene.

Se sabe que esta es una galaxia de muy baja metalicidad (Z≃0.0015), Peña et al. (2007) estudiaron 12 regiones H II distribuidas a lo largo de toda la galaxia y mostraron que la composición química derivada de estos objetos es muy homogénea, en promedio para estos objetos se tiene que 12+log(O/H) = 7.77±0.07, resultado que está de acuerdo con lo encontrado por Evans et al. (2007) para estrellas B supergigantes. De acuerdo con estos resultados NGC 3109 tiene una metalicidad menor que la SMC, donde para esta última se tiene que 12+log(O/H) = 8.00 (Dennefeld, 1989; Garnett, 1999).

En esta galaxia se conocen 20 NPs (Peña et al., 2007) y del análisis de las abundancias químicas de regiones H II y algunas de estas NPs, se reportó (Peña et al., 2007) que la abundancia de O en todas las NPs estudiadas es sistemáticamente superior que la de las regiones H II, en promedio es mayor por 0.39 dex.

El estudio de la cinemática de las NPs NGC 3109 está enfocado a determinar cómo se relacionan las poblaciones estelares de edad intermedia a vieja con el disco de gas de H I que envuelve a esta galaxia.

2

Kinematic study of planetary nebulae in NGC 6822

2.1. Resumen.

La cinemática de las NPs en las galaxias es clave para entender el comportamiento de estrellas de masa baja a intermedia (LIMS) y su relación con otras componentes de las galaxias. Al medir velocidades radiales precisas de NPs (población de edad intermedia), regiones H II y estrellas A supergigantes (población joven) en NGC 6822. El objetivo principal es determinar si ambos tipos de poblaciones siguen el comportamiento cinemático del disco de H I que posee esta galaxia.

De las 26 NPs conocidas de NGC 6822 se obtuvieron datos espectrales de alta resolución para cuatro NPs con MIKE con el telescopio Magallanes Clay, Chile. Este espectrógrafo cuenta con dos brazos que permiten obtener el espectro azul y rojo simultámeamente. El rango espectral que cubre va de 3350Å a 5050Å en el azul y de 4950 Å a 9400 Å en el rojo. Se utilizó un "binning"de 2×2, obteniendo una escala espacial de 0.2608"/pix, mientras que la resolución espectral varia de 0.14 Å a 0.17 Å (aproximadamente 10.8 km s^{-1}) en el azul y de 0.23 Å a 0.27 Å (aproximadamente 12.8 kms^{-1}) en el rojo.

Con el Manchester Echelle Spectrometer (MES) en el telescopio de 2.1 m en San Pedro Mártirel se adquirieron datos de una nebulosa planetaria (NP) y una región H II. El MES es un espectrógrafo echelle de rendija larga que utiliza filtros. También se agregaron a la muestra tres NPs y una región H II las cuales fueron tomadas del SPM Kinematic Catalogue: Extragalactic Planetary Nebulae (SPM KINCAT) de Richer et al. (2010).

En total se tienen datos de alta calidad para 10 de las 26 NPs de NGC 6822. Las velocidades heliocéntricas medidas a partir de los espectros calibrados tienen una precisión mejor que 5-6 km s^{-1}. Adicionalmente se agregaron datos de la literatura de dos regiones H II y de dos estrellas supergigantes tipo A al análisis, para comparar las velocidades radiales heliocéntricas de diferentes poblaciones estelares con las velocidades del disco de H I en la misma posición proyectada.

A partir del análisis de las velocidades radiales de los objetos de NGC 6822, se encontró que las regiones H II y las estrellas supergigantes tipo A tienen un comportamiento cinemático como el del disco de H I en la misma posición, tal y como se esperaría para estos objetos jóvenes. En contraste, la mayoría de las NPs presentan una diferencia de

velocidades significativa (mayor que 12 km s^{-1}) a las del disco de H I en la misma posición. El resultado principal es que la cinemática de las NPs es diferente de la cinemática de la población joven y su comportamiento es mucho más similar al que presenta las estrellas de carbono, estas estrellas son de edad intermedia-vieja y pertenecen a un esferoide estelar que existe en esta galaxia. Con estos resultados se confirmó que existen al menos dos sistemas cinemáticos diferentes en NGC 6822.

A&A 568, A82 (2014)
DOI: 10.1051/0004-6361/201322002

Astronomy & Astrophysics

Kinematic study of planetary nebulae in NGC 6822[⋆,⋆⋆]

S. N. Flores-Durán[1], M. Peña[1], L. Hernández-Martínez[1], J. García-Rojas[2,3],, and M. T. Ruiz[4]

[1] Instituto de Astronomía, Universidad Nacional Autónoma de México, Apdo. Postal 70264, México D.F., 04510, Mexico
e-mail: [sflores;miriam]@astro.unam.mx
[2] Instituto de Astrofísica de Canarias, 38200 La Laguna, Tenerife, Spain
[3] Departamento de Astrofísica, Universidad de La Laguna, 38205 La Laguna, Spain
e-mail: jogarcia@iac.es
[4] Depto. de Astronomía, Universidad de Chile, Casilla 36D Las Condes, Santiago, Chile
e-mail: mtruiz@das.uchile.cl

Received 31 May 2013 / Accepted 13 May 2014

ABSTRACT

Context. The kinematics of planetary nebulae in external galaxies and in our own is a clue for understanding the behavior of the low- and intermediate-mass stars and their relation with other components of the galaxies.
Aims. By measuring precise radial velocities of planetary nebulae (which belong to the intermediate-age population), H regions and A-type supergiant stars (which are members of the young population) in NGC 6822, we aim to determine whether both types of population share the kinematics of the disk of H found in this galaxy.
Methods. Spectroscopic data for six planetary nebulae were obtained with the high spectral-resolution spectrograph *Magellan* Inamori Kyocera Echelle (MIKE) on the *Magellan* telescope at Las Campanas Observatory. Data for another three PNe and one H region were obtained from the SPM Catalog of Extragalactic Planetary Nebulae, which employed the Manchester Echelle Spectrometer attached to the 2.1m telescope at the Observatorio Astronómico Nacional, México. An additional PN and one H region were observed with this same telescope-spectrograph in 2013. Thus, in total we have high-quality data for 10 of the 26 PNe detected in this galaxy. In the wavelength calibrated spectra, the heliocentric radial velocities were measured with a precision better than 5–6 km s^{-1}. Data for two additional H regions and two A-type supergiant stars were collected from the literature. The heliocentric radial velocities of the different objects were compared to the velocities of the H disk at the same position.
Results. From the analysis of radial velocities we found that H regions and A-type supergiants do share the kinematics of the H disk at the same position, as expected for these young objects. In contrast, most planetary nebula velocities differ significantly (more than 12 km s^{-1}) from that of the H at the same position. The kinematics of planetary nebulae is different from the young population kinematics and is more similar to the behavior shown by carbon stars, which are intermediate-age members of the stellar spheroid existing in this galaxy. Our results confirm that there are at least two very different kinematical systems in NGC 6822.

Key words. Local Group – planetary nebulae: general – Galaxy: kinematics and dynamics – galaxies: individual: NGC 6822

1. Introduction

Planetary nebulae (PNe) are produced in the advanced evolutionary stages of stars with initial masses from- about 1 $M_{\odot}$ to 8 $M_{\odot}$ that have a wide age spread (from 0.1 to 9 Gyr, Allen et al. 1998). Therefore PNe are valuable tracers of low- and intermediate-mass stars (LIMS). Because of their selective emission in a small number of strong and narrow emission lines, PNe can be discovered at significant distances within the nearby Universe (at least 30 Mpc). Studying them provides accurate information on the luminosity, age, metallicity, and- dynamics of the parent stellar population. This makes them very useful for testing several theories about the evolution of LIMS and galaxies. In this work we study the kinematics of the PN population of the dwarf irregular galaxy NGC 6822 to explore the connection of its intermediate and old stellar population with its H envelope. A similar study on the relation of the PN population and the H gas envelope in other Local Group member, IC 10, was carried out by Gonçalves et al. (2012), who reported that there is a kinematical connection between both populations in IC 10. Several authors have also used the PN population to analyze the kinematics of elliptical galaxies, for example, Mc Neil-Moylan et al. (2012), Teodorescu et al. (2011), and Coccato et al. (2009) have analyzed PNe kinematics in ellipticals at about 20 Mpc, and Ventimiglia et al. (2011) and Gerhard et al. (2007) have studied ellipticals at 50–100 Mpc.

The galaxy NGC 6822 is a member of the Local Group, located at a distance of 459 ± 10 kpc (Mateo 1998; Gieren et al. 2006). Its optical structure was discussed by Hodge (1977). It is dominated by a bar of about 8′ long (equivalent to 1.07 kpc) and with a position angle (PA) of 10°. There is clear evidence of recent star formation in this galaxy, which includes more than a hundred detected H regions (Killen & Dufour 1982; Hodge et al. 1988). A huge H disk of about 6 × 13 kpc, at PA of 110°, centered on the galactic center and including the optical bar, was discovered recently (de Blok & Walter 2000; Weldrake et al. 2003). In addition, by studying carbon stars, Letarte et al. (2002) revealed that NGC 6822 is surrounded by a huge stellar structure, composed mainly of intermediate and old age stars. By analyzing the stellar component, de Blok & Walter (2006),

⋆ Based on data obtained at Las Campanas Observatory, Carnegie Institution, Chile.
⋆⋆ Based on data collected at the Observatorio Astronómico Nacional, SPM. B.C., México.

Table 1. Physical properties of NGC 6822.

Property	Value	Ref.
Hubble type	IB(s)m	(1)
Other ID	DDO 209, IC 4895	
RA (J2000)[a]	19h44m56.6s	(2)
Dec (J2000)[a]	–14° 48′ 04.5″	(2)
Distance (kpc)	459 ± 17	(3)
Systemic Vel. (km s^{-1})	–57 ± 2, 55 ± 2	(4, 5)
Inclination (deg)	50.1	(2)
$E(B-V)$	0.231	(3)
M_V	–15.2 ± 0.2	(6)
$M_\star$ (10^6 $M_\odot$)	100	(4)
$M_{\rm HI}$ (10^6 $M_\odot$)	130	(7)
12 + log (O/H), A	8.36 ± 0.19	(8)
12 + log (O/H), H	8.11 ± 0.10	(9)

Notes. [(a)] H dynamical center coordinates.

References. (1) NASA/IPAC Extragalactic Database; (2) Brandenburg & Skillman (1998); (3) Gieren et al. (2006); (4) Koribalski et al. (2004); (5) Mateo (1998); (6) Dale et al. (2007); (7) Weldrake et al. (2003); (8) Venn et al. (2001); (9) Hernández-Martínez et al. (2009).

also found that the old-intermediate age stars are significantly more extended than the H disk. The stellar spheroid has been mapped by Battinelli et al. (2006), who reported a semi-major axis of 36′ (equivalent to 4.82 kpc) with a PA of 64.5°; therefore the old stellar distribution is substantially different from the H disk. With these characteristic, NGC 6822 has been cataloged as a polar-ring galaxy (Demers et al. 2006) and it contains at least two dynamical systems: the huge H disk whose kinematics has been studied in depth by de Blok & Walter (2000, 2006) and which shows a disk rotation, and the intermediate-age population, represented by carbon stars of the spheroid, whose kinematics was analyzed by Demers et al. (2006). This kinematics contrasts strongly with that of the H disk, because the spheroid rotates around its minor axis, whose PA differs by about 46° of the rotation axis of the H disk.

The main physical properties of NGC 6822 are listed in Table 1.

It has been proposed that dwarf irregular galaxies are dominated, at all radii, by dark matter that largely controls their kinematics. This seems to be the case of NGC 6822 (Weldrake et al. 2003; Hwang et al. 2014). In addition, numerical simulations based on the ΛCDM cosmology allow determining the dark-matter distribution and predict galactic dark-matter halos with cuspy density profiles in dwarf irregular galaxies (Navarro et al. 1996). However, some galaxies seem to favor the existence of halos with soft cores (see the discussion in Valenzuela et al. 2007, and references therein). Therefore these galaxies are very well-suited laboratories for testing ΛCDM models. These phenomena can be traced through the analysis of the velocity field of different objects in the galaxy, which provides some constraints that help to test the models. Valenzuela et al. (2007) suggested that the kinematics of PNe, because they are intermediate-age objects, provides valuables clues for determining the shape of the dark matter halo. The main aim in this work is to study the kinematical behavior of the different types of populations existing in the dwarf irregular NGC 6822 via the analysis of some PNe, H regions, and members of the stellar components. In the long term, we will discuss these kinematics in relation to ΛCDM models.

In Sect. 2 we present the observations, data reduction, and data compiled from the literature, as well as the radial velocities derived for the different objects. In Sect. 3 the velocities of PNe, H regions, and two A-type supergiant stars are compared to the velocities of the H disk. The results of the kinematical analysis are presented in Sect. 4. In Sect. 5 we present the line profiles and the nebular diagnostic of some of our PNe as derived from our high resolution spectra. General results are presented in Sect. 6.

Table 2. PNe, H regions, and stars analyzed in NGC 6822.

Object ID[a]	RA (J2000)	Dec (2000)	Other ID
PN2[b]	19:45:56.6	–14:40:53.4	PN5[d]
PN4[b c]	19:45:01.4	–14:41:33.0	S30[e] PN4[d]
PN6[b c]	19:44:00.7	–14:42:43.6	PN1[d]
PN7[c]	19:44:49.1	–14:43:00.6	PN2[d]
PN8[b]	19:42:02.2	–14:43:42.2	PN6[d]
PN10[c]	19:45:22.0	–14:43:28.0	PN19[d]
PN12[c]	19:44:58.8	–14:44:45.0	S14[e] , PN14[d]
PN14[b c]	19:45:07.5	–14:47:35.8	S33[e] ,PN7[d]
PN16[c]	19:44:58.6	–14:46:10.0	S16[e] , PN13[d]
PN20[b]	19:45:11.5	–14:48:53.6	PN20[f]
H V[g]	19:44:52.4	–14:43:13.4	–
H X[g]	19:45:5.23	–14:43:16.7	–
H 18[c]	19:44:42.6	–14:50:30.2	H 18[d] , S10[e]
H 15[c]	19:44:57.2	–14:47:50.6	H 08[d] , S28[e]
A 13[h]	19:44:53.4	–14:46:42	A supergiant
A 101[h]	19:44:56.5	–14:46:14	A supergiant

Notes. [(a)] Names as in Hernández-Martínez & Peña (2009), except for H V and H X. [(b)] Observed at LCO with MIKE. [(c)] Observed at SPM with MES. [(d)] Leisy et al. (2005). [(e)] Killen & Dufour (1982). [(f)] Richer & McCall (2007). [(g)] Hubble (1925). [(h)] Venn et al. (2001).

2. Data acquisition and measurements of radial velocities

High spectral resolution data for four PNe (PN2, PN4, PN6, and PN14 of Table 2) were obtained with the double echelle *Magellan* Inamori Kyocera Echelle spectrograph (MIKE) attached to the *Clay Magellan* Telescope at Las Campanas Observatory (LCO, Carnegie Institution, Chile), during the nights 2010 June 5 and 6. Two more objects (PN8 and PN20) were observed in 2014 March 6 and 8. The MIKE spectrograph operates with two arms that allow obtaining a blue and a red spectrum simultaneously (Berstein et al. 2003). The standard grating setting was used, which provides a full wavelength coverage from 3350 Å to 5050 Å in the blue, and from 4950 Å to 9400 Å in the red. The slit size was 1″ along the dispersion axis and 5″ in the spatial direction. A binning of 2 × 2 was used, thus obtaining a spacial scale of 0.2608 ″/pix, while the spectral resolution varied from 0.14 Å to 0.17 Å (about 10.8 km s^{-1}) in the blue and from 0.23 Å to 0.27 Å (about 12.8 km s^{-1}) in the red, as measured from the HWHM of the lines of the Th-Ar comparison lamp. Each object was observed on one occasion with an exposure time of 15 minutes. During the observing runs the seeing was better than 1″, most of the time.

For the other three PNe, high spectral resolution data were retrieved from the database of the San Pedro Mártir (SPM) Catalog of Extragalactic Planetary Nebulae[1] where data for some objects in common with LCO observations were found as well. The data available in this catalog consist of velocity-position diagrams for the [O]λ5007 and Hα emission lines, obtained with the Manchester Echelle Spectrometer

[1] http://kincatpn.astrosen.unam.mx/, for details see Richer et al. (2010).

(MES-SPM). In this case the spectral resolution is 0.077 Å/pix at [O]λ5007 and 0.100 Å/pix at Hα, equivalent to about 11 km s^{-1} for 2.6 pix FWHM. We downloaded the fits files for these PNe and calculated their heliocentric radial velocities from both lines, when available. An additional planetary nebula (PN7) and the H region #15 were observed with the same instrument, MES, at SPM Observatory on July 4, 2013. For the PN four spectra of 1800 s exposure time each were acquired; for the H region two spectra of 1200 s and 900 s were obtained. The Hα filter was used in both cases. The spectra were combined and reduced according to the standard process for MES data (see Richer et al. 2010).

Gathering all these data, we have information of the kinematical behavior of ten PNe, which represents almost 40% of the known PN candidates in this galaxy (26 objects reported by Hernández-Martínez & Peña 2009). It is important to note that we have data for several PNe near the galactic center, but also for the PNe that are the farthest away from the center (see Fig. 1).

In addition to PN data, spectroscopic data for some H regions (which represent the youngest population in the galaxy) were also obtained as another test to check the kinematical behavior of objetcs in NGC 6822. High-resolution calibrated spectra for the bright H regions H V and H X, obtained at the ESO Very Large Telescope with the UVES spectrograph at 2 Å resolution, were kindly provided by A. Peimbert (Peimbert et al. 2005). Data for H 18 was extracted from the SPM catalog mentioned above, and a new spectrum for H 15 was obtained as described in the previous paragraph.

On the other hand, high-resolution spectra of two A-type supergiant stars (located near the center of the galaxy) were analyzed in depth by Venn et al. (2001). By performing spectral synthesis of several stellar lines, these authors computed several stellar parameters, among them accurate radial velocities that we used here (see their Table 1). These stars are considered as representative of the young stellar population.

In next Sect. 3 we compare the heliocentric velocities of PNe, H regions and A-type supergiants with the H gas velocities given by de Block & Walter (2006) and with the kinematics of the carbon stars (Demers et al. 2006).

In Table 2 the identification of the observed objects is presented. Names for PNe and H regions (except those of H V and H X) were adopted from Hernández-Martínez & Peña (2009).

2.1. Data reduction

Data reduction of LCO Clay-MIKE spectra was carried out by using IRAF[2] echelle reduction packages. Raw 2D echellograms were bias-subtracted and flat-fielded. The spectra were extracted with an extraction window of 3.72″ wide. Wavelength calibration was performed with a Th-Ar lamp, which was observed immediately after each science exposure. Data from 2010 run were flux calibrated using the spectro-photometric standard stars Feige 110, LDS 749B, and NGC 7293 (Oke 1990). No flux calibration was performed for the data obtained in March 2014. The full description of the reduction procedure can be found in García-Rojas et al. (2012). Heliocentric radial velocity correction was applied to all the spectra.

For the MES-SPM data reduction procedure see Richer et al. (2010). The fits files retrieved from the SPM catalog provide wavelength-calibrated spectra. These data are not flux calibrated. For these spectra the heliocentric velocity correction was also applied.

[2] IRAF is distributed by the National Optical Astronomy Observatories, which is operated by the Association of Universities for Research in Astronomy, Inc., under contract to the National Science Foundation.

Table 3. LCO PNe dereddened[a] fluxes and heliocentric velocities for each line[b] .

Object	λ_{obs} (Å)	Ion	λ_{rest} (Å)	Flux/ F(Hβ)	V_{helio} (km s^{-1})
PN2	4339.23	Hγ	4340.47	0.445	–85.9
PN2	4362.1:	[O]	4363.21	0.178	–75.8:
PN2	4859.96	Hβ	4861.33	1.000	–84.7
PN2	4957.55	[O]	4958.91	1.395	–82.4
PN2	5005.47	[O]	5006.84	4.142	–82.3
PN2	6560.93	Hα	6562.82	2.812	–86.4
PN2	6581.59	[N]	6583.41	0.072	–83.0
PN2	6716.1:	[S]	6716.47	0.032	19.1:
PN2	6730.8:	[S]	6730.85	0.021	–1.9:
PN4	4339.47	Hγ	4340.47	0.500	–68.9
PN4	4362.19	[O]	4363.21	0.224	–70.1
PN4	4684.70	He	4685.68	0.229	–63.4
PN4	4860.25	Hβ	4861.33	1.000	–66.8
PN4	4957.82	[O]	4958.91	2.290	–65.8
PN4	5005.74	[O]	5006.84	6.651	–66.0
PN4	6561.31	Hα	6562.82	2.809	–69.0
PN4	6581.94	[N]	6583.41	0.394	–66.9
PN4	6715.23	[S]	6716.47	0.029	–55.3
PN4	6729.41	[S]	6730.85	0.059	–64.0
PN4	7134.06	[Ar]	7135.78	0.091	–72.4
PN6	4339.37	Hγ	4340.47	0.468	–76.3
PN6	4362.08	[O]	4363.21	0.091	–77.8
PN6	4860.09	Hβ	4861.33	1.000	–76.4
PN6	4957.67	[O]	4958.91	2.766	–75.1
PN6	5005.61	[O]	5006.84	7.257	–73.6
PN6	6561.15	Hα	6562.82	2.804	–76.6
PN6	6581.78	[N]	6583.41	0.412	–74.3
PN6	6714.66	[S]	6716.47	0.017	–80.9
PN6	6729.05	[S]	6730.85	0.235	–80.3
PN6	7133.94	[Ar]	7135.78	0.525	–77.0
PN8	4685.29	He	4685.68	–	–1.8
PN8	4860.84	Hβ	4861.33	–	–7.1
PN8	4958.3:	[O]	4958.91	–	–0.2:
PN8	5006.35	[O]	5006.84	–	–6.2
PN8	6562.22	Hα	6562.82	–	–4.3
PN14	4340.11	Hγ	4340.47	0.062	–25.2
PN14	4362.83	[O]	4363.21	0.115	–25.9
PN14	4685.33	He	4685.68	0.463	–22.4
PN14	4860.88	Hβ	4861.33	1.000	–27.9
PN14	4958.48	[O]	4958.91	3.556	–26.0
PN14	5006.40	[O]	5006.84	10.780	–26.1
PN14	6547.49	[N]	6548.03	1.347	–24.7
PN14	6562.21	Hα	6562.82	2.797	–27.8
PN14	6582.86	[N]	6583.41	3.966	–25.3
PN14	6715.82	[S]	6716.47	0.036	–28.9
PN14	6730.25	[S]	6730.85	0.039	–26.7
PN14	7135.13	[Ar]	7135.78	0.064	–27.5
PN20	4860.40	Hβ	4861.33	–	–33.8
PN20	4958.03	[O]	4958.91	–	–29.7
PN20	5005.91	[O]	5006.84	–	–32.2

Notes. [a] Fluxes dereddened by using Seaton (1979) reddening law. [b] A colon in the wavelength indicates a large uncertainty.

2.2. Measuring the radial velocities

For all the objects observed at LCO, we systematically chose the most intense lines in the blue and red spectra to measure the velocities. They were measured by fitting a Gaussian profile

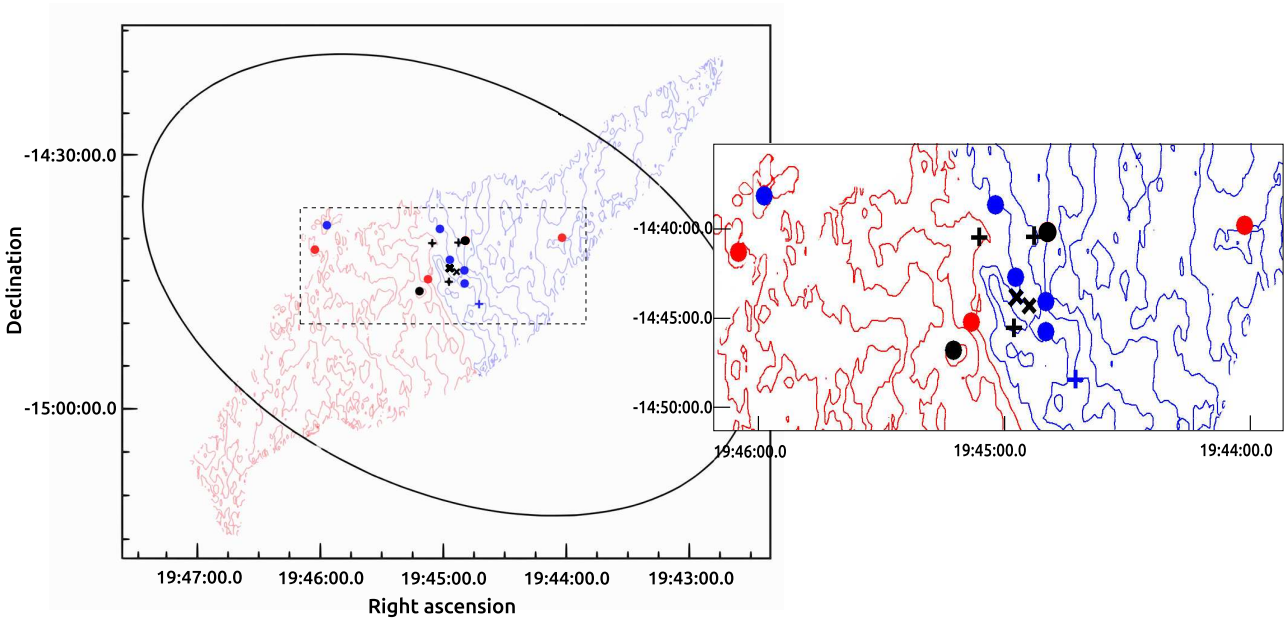

Fig. 1. Radial velocity map of H from de Block & Walter (2006). The blue contours run from −55 km s^{-1} in the inner part to −110 km s^{-1} in the outer NW zone, in steps of 5 km s^{-1}. The red contours run from −50 km s^{-1} in the central zone to +10 km s^{-1} in the outer SE zone. The ellipsoid represents the stellar spheroid analyzed by Battinelli et al. (2006) and Demers et al. (2006). Position of the PNe (filled dots), H regions (crosses) and A-type supergiants (x marks) are those presented in Table 2. Blue symbols indicate a negative difference between observed objects and H velocities. Red symbols indicate a positive difference. In black we plot objects with a velocity difference smaller than 12 km s^{-1}, relative to H disk. A zoom of the central zone is shown.

Table 4. Heliocentric velocities for SPM objects and comparison with LCO values.

	SPM (km s^{-1})		LCO (km s^{-1})	
Object ID	[O] λ5007	Hα λ6563	[O] λ5007	Hα λ6563
PN4	−59.9	−64.3	−66.0	−69.0
PN6	−72.6	–	−73.6	−76.6
PN7	–	−55.4	–	–
PN10	−69.6	−70.9	–	–
PN12	−86.8	−87.0	–	–
PN14	−29.3	−29.0	−26.1	−27.8
PN16	−77.1	−76.1	–	–
H 18	−88.1	–	–	–
H 15	–	−73.3	–	–

to the observed profile using the *splot* IRAF routine. In Table 3 we present the lines measured for each object: in Col. 1 object names are listed, the observed wavelength, λ_{obs} is presented in Col. 2; the ion identification is found in Col. 3, and in Col. 4 the laboratory wavelength is given; the observed flux relative to Hβ and the heliocentric radial velocity calculated are listed in Cols. 5 and 6. We adopted the average velocity given by all the measured lines as the heliocentric velocity of the object.

For the objects from the SPM catalog, the available lines (Hα, [O] 5007) were measured and the heliocentric radial velocity calculated. In Table 4 we present these velocities and compare them with the values from LCO observations for the objects in common. The two sets of values are very similar. The largest differences are found for PN4, where ΔV between LCO and SPM data for [O] λ5007 and Hα lines are 6.1 km s^{-1} and 4.7 km s^{-1} respectively; these differences lie within the uncertainties. In all the other cases the differences are smaller. This shows that our velocities obtained from the high-resolution spectra from LCO and SPM are very reliable because they have uncertainties smaller than about 5–6 km s^{-1}.

For the H regions H V and H X, the central wavelengths of Hβ, and [O]$\lambda\lambda$4959 and 5007 were measured by adjusting a Gaussian profile to the lines to determine their heliocentric radial velocities. The dispersion given by the lines is smaller than 3 km s^{-1}.

3. Radial velocities of different objects

In this section the behavior of the radial velocities of the objects is analyzed in relation to the velocities of the H disk and the stellar spheroid at the same projected position.

3.1. H I disk

Using the velocity field obtained by de Block & Walter (2006) for the H disk, we compared the heliocentric velocities of PNe, H regions, and A-type supergiants with those of the H gas. The results can be found in Table 5 where we present for all our objects, the adopted heliocentric velocity and its uncertainty (at 1σ), and the velocity of the H at the same projected position. The fifth column shows the difference $\Delta = V_{helio} - V_{HI}$, and in the sixth column we present the difference between the systemic velocity (–55 km s^{-1} from Mateo 1998) and our objects.

The position of our objects in the galaxy and their difference in velocity relative to the H disk are illustrated in Fig. 1, where we have included the location of the spheroid of intermediate-age stars (Battinelli et al. 2006; Demers et al. 2006), which has a semi-major axis of 36′ long, oriented at PA of 64.5°.

Column 5 of Table 5 shows that the differences in velocity between the PNe (all except two) and the H at the same position, are larger than ±12 km s^{-1}, which is significantly higher

Table 5. Heliocentric velocities of PNe, H regions, A supergiants, and H gas.

Object	V_{helio} (km s^{-1})	± (km s^{-1})	V_{HI} (km s^{-1})	Δ (km s^{-1})	Δ_{sys} (km s^{-1})
PN2[a]	–84.1	1.7	–24.0	–60.1	–29.1
PN4	–66.5	3.8	–54.4	–12.2	–11.5
PN6	–76.8	2.1	–89.2	+12.4	–21.8
PN7	–55.4	4.6	–64.9	+9.5	–0.4
PN8	–4.7	3.0	–20.8	–16.1	+50.2
PN10	–69.6	3.2	–54.1	–15.5	–14.6
PN12	–86.7	4.9	–65.8	–20.9	–31.7
PN14	–26.5	1.3	–47.5	+21.0	+28.5
PN16	–77.1	4.7	–60.6	–16.5	–22.1
PN20	–31.8	6.0	–36.9	+5.1	+23.1
H V	–62.7	2.1	–58.2	–4.5	–7.7
H X	–57.3	2.5	–48.7	–8.6	–2.3
H 18	–87.4	1.8	–63.2	–24.2	–32.4
H 15	–73.0	6.0	–61.3	–11.7	–18.0
A 13[b]	–55	2.0	–57.3	2.3	0.0
A 101[b]	–65	2.0	–53.8	–11.2	–10.0

Notes. [a] The weak [S] and [O]4363 lines were not considered. [b] A supergiants analyzed by Venn et al. (2001).

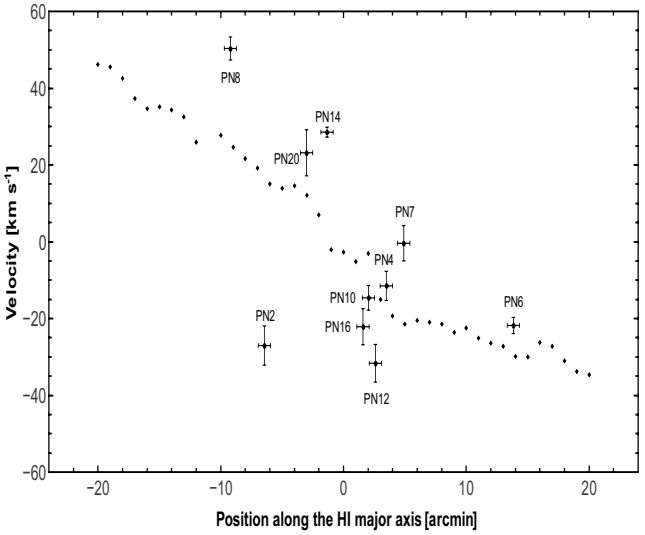

Fig. 2. PNe velocities, relative to the system, and their positions projected on the H disk major axis. The dotted line shows the rotation of the disk.

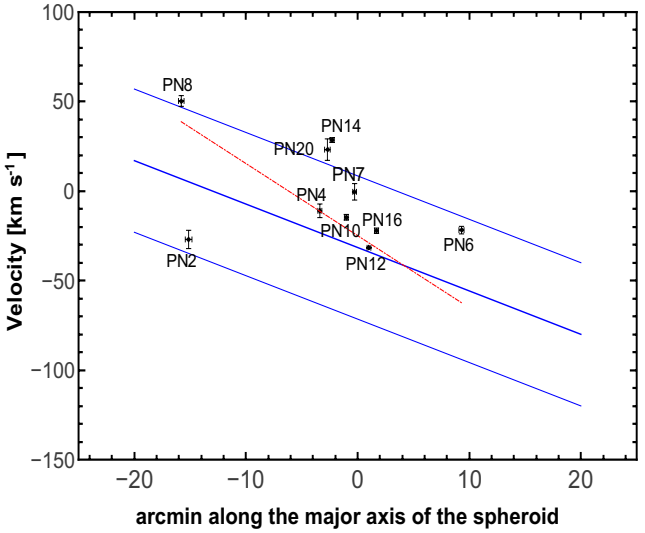

Fig. 3. Systemic velocity of PNe vs. their position projected along the major axis of the spheroid. The central line is the best fit to the velocities of the carbon stars (relative to the systemic velocity), as given by Demers et al. (2006). Top and bottom lines indicate their dispersion. A linear fit to the PNe velocities is also shown (dashed-dotted red line). The velocity uncertainties of PNe are marked.

than the uncertainties. According to the velocity map for H by de Blok & Walter (2006, see Fig. 1), the H disk rotates around the optical center with its NE zone moving toward us (heliocentric velocities from −110 to −55 km s^{-1}), while the SW zone recedes from us at velocities from −50 to +10 km s^{-1}. Half of our PNe are approaching faster than the H gas, with differences from −60 km s^{-1} to −12 km s^{-1}, while the other half are receding from the disk with velocity differences from +5 km s^{-1} to +21 km s^{-1}, that is, the H disk is leaving these objects behind.

To better illustrate the differences in velocity between our PNe and the H disk, Fig. 2 shows the PN velocities (relative to the system) vs. their position projected along the major axis of the H disk. The rotation of the H disk is shown as a dotted line, and it shows some irregularities that so far have not been explained. However, this figure shows that PNe do not rotate with the disk, but have a much more disperse velocity field.

In contrast, the heliocentric velocities of the H regions H V, H X, and H 15 and the A-type supergiants are very similar to those of the H disk, with differences smaller than 12 km s^{-1}, as expected because they are young objects. They share the movement of the H disk. In the case of H 18, which is cataloged as a H region by Leisy et al. (2005), it presents a large velocity difference of −24.2 km s^{-1} relative to the H gas. In the appendix we discuss the possibility that this nebula is in fact a planetary nebula superposed on a H region, which would explain its strange kinematics.

3.2. Stellar spheroid and its velocity field

Demers et al. (2006) measured radial velocities of 110 carbon stars located within 15′ of the H major axis with a precision of ±15 km s^{-1}. These stars belong to the stellar spheroid and seem to be rotating with a rotation axis that almost coincides with the minor axis of the stellar spheroid. Thus, the rotation axis of the C-star system and that of the H disk differ by about 46°, which indicates that there are two different kinematical systems.

In the following we compare the PN heliocentric velocities with those of the carbon stars. We projected the positions of the PNe with respect to the major axis of the ellipsoid (PA 65°) and, subtracting the system velocity, we located them in Fig. 3, where we show a band representing the average behavior of carbon star velocities (and its dispersion). The uncertainties of our data in this figure are not larger than 6 km s^{-1}. We included a linear fit to the velocities of our PN sample.

Interestingly, we found that the heliocentric velocities of PNe are similar to those reported for the carbon stars near the same position. Our PN sample also shows a velocity dispersion as large as the C stars. PN2 and PN8, located in the East part of the bar, show the strongest differences with the average of carbon star velocities, although it is always inside the C-star velocity dispersion. The fit for the PNe shown in Fig. 3 seems steeper

than that for the C-stars, but as this is a fit for only ten objects, it is not very reliable. Thus, we consider that both behaviors are similar in the sense that the PN system seems to rotate in a way similar to the C-star spheroid. Nevertheless, one important difference is that the PN average velocity is –57.8 km s^{-1}, which agrees very well with the systemic velocity, while the C-star mean velocity is –32.9 km s^{-1}, that is, the spheroid would be receding relative to the galaxy, with a velocity of about 22 km s^{-1}. This latter possibility was indicated by Hwang et al. (2014), who in addition, by studying the kinematics of four extended stellar clusters, found that these objects (located from one side to the other of the extended stellar spheroid) do not rotate as the C-stars, and they present an average velocity of –88.3 km s^{-1}, which is also very different from the system velocity (the stellar clusters would be moving towards us 30 km s^{-1} faster than the galaxy). In both cases (C-stars and stellar clusters) this is a peculiar kinematical behavior that deserves future studies.

4. Conclusions for the kinematics

By using high spectral resolution data obtained at LCO and SPM, we studied the kinematics of ten PNe and four H II regions and compared them with the kinematics of the extended H I disk and the C stars of the stellar spheroid of NGC 6822. The behavior of two A-type supergiant stars was analyzed as well.

It is clear that the studied PNe are not moving along with the H I gas and their kinematics is more similar to that of the C-stars of the stellar spheroid. This is not the case of the A-type supergiants and the H II regions H V, H X, and H II 15, which seems to be part of the dynamical system of the H I disk, which is expected because they are young objects.

One of the regions that was previously declared a H II region, the compact H II 18, shows kinematics closer to the PNe and C stars, with a difference in velocity of –24.2 km s^{-1} relative to the H I gas at the same position. In the appendix we propose that this nebula might be a true PN located near a faint and extended H II region, which might explain the fuzzy appearance of H II 18, and its peculiar kinematics.

Because of their systemic velocities, PNe seem to be part of the intermediate-age stellar spheroid in NGC 6822. However, the average velocity of our sample of ten PNe is –57.8 km s^{-1}, therefore the PN sample shares the system velocity of –55 km s^{-1}. On the other hand, the C-stars measured by Demers et al. (2006) show an average velocity of –32.9 km s^{-1} and the four stellar clusters reported by Hwang et al. (2014) have an average velocity of –88.3 km s^{-1}. Therefore, it seems that NGC 6822 has different kinematical systems (the H I gas and the young objects, the stellar spheroid with its C-stars, the stellar clusters in the stellar halo, etc.) that deserve to be investigated in more detail.

5. Line profiles and other characteristics of analyzed PNe

With the high spectral resolution used, the line profiles of the objects observed at LCO are resolved. In Fig. 3 we present the profiles of [O III] λ5007, Hα, and [N II] λ6583 lines for PN6, PN4, PN2 and PN14. The profiles are different in each case: PN6 presents more compact lines, very Gaussian in shape. The FWHM of lines (after subtracting the instrumental and thermal widths by assuming that they add in quadrature) is 17 ± 2 km s^{-1}, indicating an expansion velocity of around 8 km s^{-1}. The situation is different in PN4 where the lines are much wider and show a structure that seems to contain three components; this is particularly clear in the [N II] line, where a central component surrounded by some kind of shell is apparent. The shell would have an expansion velocity of about 25 km s^{-1}. In PN2 the lines are Gaussian but wider than for PN6, with a FWHM of about 25 km s^{-1}. Then, the expansion velocity in PN2 would be of about 12 km s^{-1}.

PN 14 shows the most interesting profiles. The [O III] lines present two very close components differing in velocity by about 15 km s^{-1}, and in the [N II] λ6583 profile a faint very wide component is apparent. This latter component represents some kind of bipolar ejection at high velocities (about 140 km s^{-1}) similar as the galactic M1-25 and M1-32 among others (Medina et al. 2006; Akras & López 2012).

5.1. Nebular diagnostic

In our high-resolution spectra the auroral line [O III] λ4363 and the [S II] $\lambda\lambda$6717,6731, useful for plasma diagnostic, are measurable for several PNe, allowing us to roughly estimate the nebular electron temperature and density. First, the line fluxes (shown in Table 2) were derreddened. The logarithmic reddening correction at Hβ, c(Hβ), was obtained from the Balmer decrement. We adopted the interstellar reddening extinction law by Seaton (1979).

We were able to determine [O III] electron temperatures and [S II] densities in PN2, PN4, PN6, and PN14 although, [O III] λ4363 and [S II] λ6717, 6730 emission lines present large uncertainties. For PN14, the [N II] temperature was also measured through the λ5755/λ6583 line ratio. For these calculations we used the *temden* routine implemented in the IRAF NEBULAR package (Shaw & Dufour 1995). The results are presented in Table 6. Despite the large errors, the calculated values are similar, whithin uncertainties, to those presented by Hernández-Martínez et al. (2009). Therefore, as PN2 is the only one without previous calculations, we consider its values to be valid. This nebula shows a high electron temperature (about 22 000 K), indicating a low metallicity object, therefore it probably belongs to the old objects in the classification of PNe made by Hernández-Martínez et al. (2009).

6. Results

Most of the results regarding the kinematics are discussed in Sect. 4, therefore we present a synthesis here. From high-resolution spectra obtained at LCO and OAN-SPM and data from the literature, the heliocentric radial velocities of ten PNe, four H II regions, and two A-type supergiant stars were analyzed and compared to the velocities of the H I disk at the same position. We found that H II regions and A-type supergiants share the kinematics of the rotating H I disk, while PNe seem to belong to a different kinematical system similar to the one shown by the C stars. Our result is different from what was found in the irregular galaxy IC 10, and implies that there are at least two kinematical systems in NGC 6822, one defined by the young population (H I disk, H II regions and young stars), the other defined by the intermediate-age population (PNe and C stars), which differ significantly. In addition, four stellar cluster in NGC 6822 seem to represent an even more different system. These clusters, of low metallicity and at high velocity relative to the system, would have accreted into the halo (Hwang et al. 2014).

Only one object of our sample, named H II 18, has a velocity apparently in contradiction with our results, showing a large velocity difference relative to the H I gas at the same position. In

Table 6. Temperature and density in PNe.

	PN6	PN4	PN2	PN14
T(O) (K)	12 400 ± 1900	18 800 ± 1630	22 200 ± 3900	13 400 ± 700
T(N) (K)	–	–	–	19 500 ± 630
N(S II)(cm^{-3})	2000 ± 1400	8600 ± 360	480 ± 290	900 ± 730
c(Hβ)	0.58	0.46	0.39	0.24

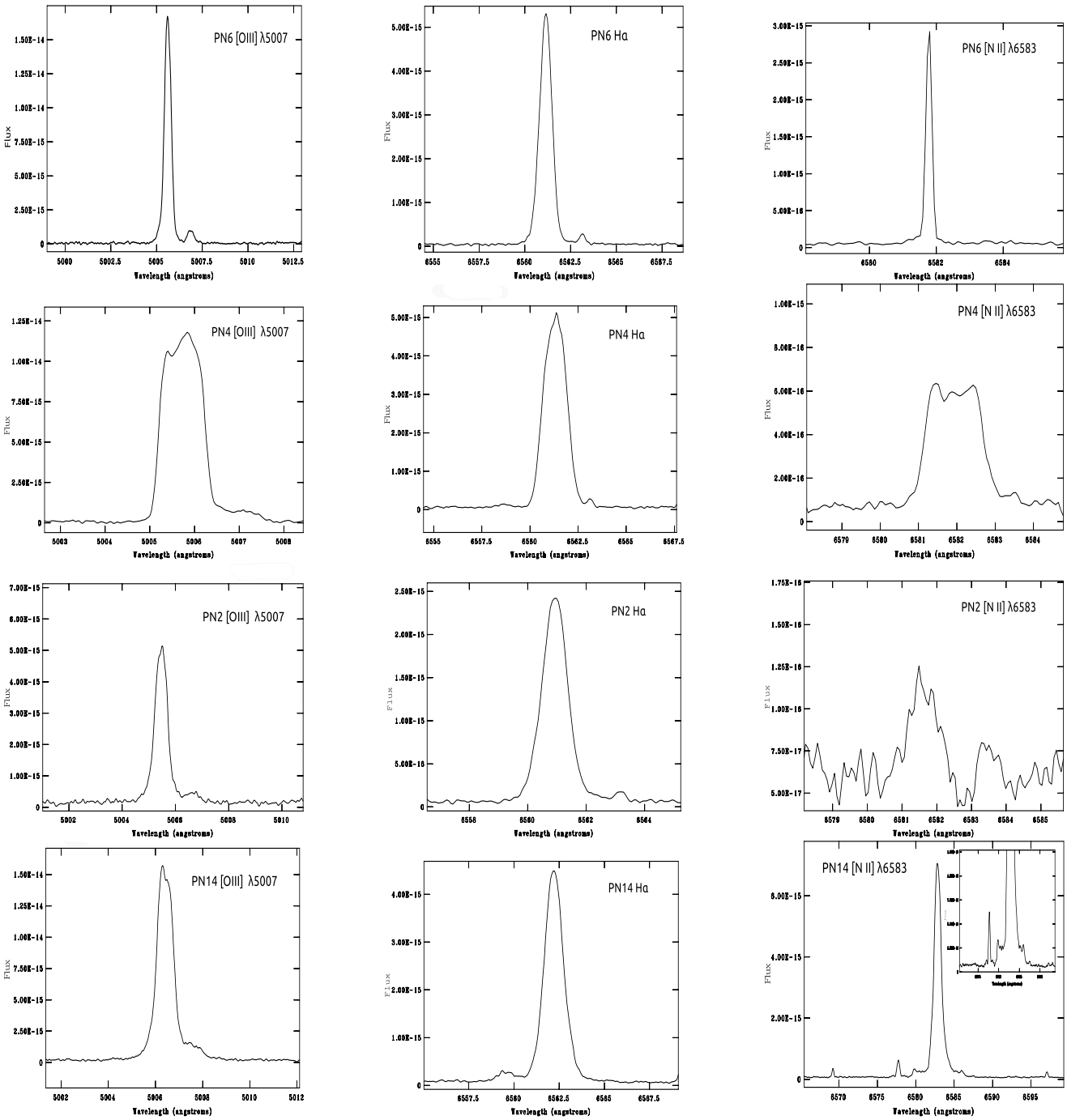

Fig. 4. Line profiles for planetary nebulae. First, second, and third columns show [O] λ5007, Hα, and [N] λ6583, respectively.

the appendix we discuss the possibility that H 18 is a PN and not an H region, which would explain its kinematics.

Physical conditions of the plasma (electron temperature and density) were determined for some PNe. Our values coincide

with previous results from the literature. For the first time, these parameters were derived for PN2, a planetary nebula at the NE of the galaxy, away from the optical bar. The high electron temperature and radial velocity of PN2 indicate that this is an old low-metallicity PN.

The line profiles of the PNe observed at LCO were measured. Expansion velocities and some velocity structures were determined for PN2, PN4, PN6, and PN14. The expansion velocities shown by our PNe reach from about 8 to 25 km s^{-1}, which is a range similar to the one found in PNe of other galaxies by Richer et al. (2010). PN14 is a very interesting object. It is a Type I PN (so it is a young object) located near the galactic center, but it is receding from the galaxy at almost 30 km s^{-1} and shows a fast bipolar ejection (jet) with a velocity of about ±140 km s^{-1}.

Many objects need to be analyzed in the future to verify the velocity field of the different populations, in particular in the central zone, to constrain the models for computing the distribution of the dark matter halo in NGC 6822.

Acknowledgements. We are indebted to W. J. G. de Blok and Antonio Peimbert, who kindly provided the H velocity map and the spectra of H V and H X used in this work. Enlightening discussion with Michael Richer is deeply appreciated. S.F.-D. received scholarship from CONACyT-Mexico, and from DGAPA-PAPIIT (UNAM) grant IN105511. This work received financial support from DGAPA-PAPIIT (UNAM) grants IN105511 and IN109614.

Appendix A: True nature of the nebula H II 18

As said in Sect. 3.1, the high radial velocity of this object, compared with that in the H disk, resembles more the values found for PNe that those of H regions. This object was first reported by Killen & Dufour (1982), who named it S 10 and described it as a compact nebula. A classification as "PN?" was given to this object. Leisy et al. (2005) declared it an extended nebula and classified it as a compact H region. It is object number 18 in their list. Similarly, Richer & McCall (2007) reported the nebula as extended. These latter authors analyzed spectrophotometric data for this object and, interestingly, they calculated an electron temperature T(O) of almost 15 000 K, which is too high, compared with the values for H regions, which never exceed 13 000 K. The oxygen abundance derived by Richer & McCall is log O/H + 12 = 7.71, which is very low when compared with the abundances of H regions, which on average are 8.06 ± 0.04 with a very small dispersion (Hernández-Martínez et al. 2009). With this high temperature and low metallicity, H 18 is more similar to the PNe of low chemical abundances in this galaxy.

Another characteristic of H 18 that might be indicating a PN nature rather than a H region is its Hα luminosity. By considering the distance given by Gieren et al. (2006) and the Hα flux estimated by Hernández-Martínez & Peña (2009), we obtain $L(\mathrm{H}\alpha)/L_{\odot}$ = 85.5, which is very similar to the Hα luminosity of PN14 (76.9 $L_{\odot}$) and is lower than expected for a compact H region ionized by an OB star.

Considering all the above, we revised the images in [O]λ 5007 and Hα obtained with the VLT FORS2 spectrograph on 2006, which served as pre-imaging for the spectroscopy work (program ID 077.B-0430) reported by Hernández-Martínez et al. (2009). The Hα image and the subtracted Hα-continuum image are shown in Fig. A.1 H 18 appears as a very intense compact

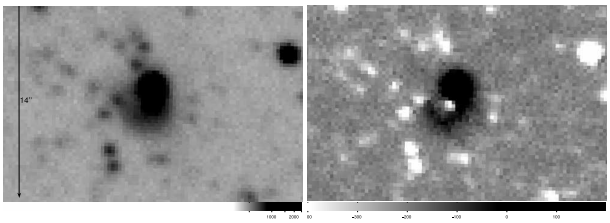

Fig. A.1. Hα (*left*) and the Hα-continuum subtracted (*right*) images of H 18 are shown. North is up and east is to the left. The scale is 14 arcsec. A small faint H region is in the SE that seems projected on top of the compact intense Hα knot.

nebula located at the edge of a faint shell-like H region , whose central star seems clearly visible.

Based on this evidence, we suggest that H 18 is a planetary nebula, overlapping a H region, which gives it an extended appearance. However, our discussion is not conclusive. Deep spectroscopic data and highly resolved imaging are required to definitely establish the true nature of the H 18 – S10 nebula.

References

Akras, S., & López, J. A. 2012, MNRAS, 425, 2197
Allen, C., Carigi, L., & Peimbert, M. 1998, ApJ, 494, 247
Battinelli, P., Demers, S., & Kunkel, W. E. 2006, A&A, 451, 905
Berstein, R. A., Shectman, S. A., Gunnels, S., Mochnacki, S., & Athey, A. 2002, Proc. SPIE, 4841
Coccato, L., Gerhard, O., Arnaboldi, M., et al. 2009, MNRAS, 394, 1249
de Blok, W. J. G., & Walter, F. 2000, ApJ, 537, L95
de Blok, W. J. G., & Walter, F. 2006, AJ, 131, 343
Demers, S., Battinelli, P., & Kunkel, W. E. 2006, ApJ, 636, L85
García-Rojas, J., Peña, M., Morisset, C., Mesa-Delgado, A., & Ruiz, M. T. 2012, A&A, 538, A54
Gerhard, O., Arnaboldi, M., Freeman, K. C., et al. 2007, A&A, 468, 815
Gieren, W., Pietrzyński, G., Nalewajko, K., et al. 2006, ApJ, 647, 1056
Gonçalves, D. R., Teodorescu, A. M., Alves-Brito, A., Méndez, R. H., & Magrini, L. 2012, MNRAS, 425, 2557
Hernández-Martínez, L., & Peña, M. 2009, A&A, 495, 447
Hernández-Martínez, L., Peña, M., Carigi, L., & García-Rojas, J. 2009, A&A, 505, 1027
Hodge, P. W. 1977, ApJS, 33, 69
Hodge, P. W., Lee, M. G., & Kennicutt, R. C. Jr. 1988, PASP, 100, 917
Hubble, E. 1925, ApJ, 62, 409
Hwang, N., Park, H. S., Lee, M. G., et al., 2014, ApJ, 783, 49
Killen, R. M., & Dufour, R. J. 1982, PASP, 94, 444
Leisy, P., Corradi, R. L. M., Magrini, L., et al. 2005, A&A, 436, 437
Letarte, B., Demers, S., Battinelli, P., & Kunkel, W. E. 2002, AJ, 123, 832
Mateo, M. 1998, ARA&A, 36, 435
McNeil-Moylan, E. K., Freeman, K. C., Arnaboldi, M., & Gerhard, O. E. 2012, A&A, 539, A11
Medina, S., Peña, M., Morisset, C. & Stasińska, G. 2006, Rev. Mex. Astron. Astrofis., 42, 53
Navarro, J. F., Frenk, C. S., & White, S. D. M. 1996, ApJ, 462, 563
Oke, J. B. 1990, AJ, 99, 1621
Richer, M. G., & McCall, M. L. 2007, ApJ, 658, 328
Richer, M. G., López, J. A., Díaz-Méndez, E., et al. 2010, Rev. Mex. Astron. Astrofis., 46, 191
Peimbert, A., Peimbert, M., & Ruíz, Ma. T. 2005, ApJ, 634, 1056
Seaton, M. 1979, MNRAS, 185, 5
Shaw, R. A., & Dufour, R. J. 1995, PASP, 107, 896
Teodorescu, A. M., Méndez, R. H., Bernardi, F., et al. 2011, ApJ, 736, 65
Valenzuela, O., Rhee, G., & Kyplin, A. 2007, ApJ, 657, 773
Venn, K. A., Lennon, D. J., Kaufner, A., et al. 2001, ApJ, 547, 765
Ventimiglia, G., Arnaboldi, M., & Gerhard, O. 2011, A&A, 528, A24
Weldrake, D. T. F., de Blok, W. J. G., & Walter, F. 2003, MNRAS, 340, 12

3

The planetary nebulae and HII region in NGC 6822 revisited.

Se obtuvieron datos espectrofotométricos de 11 NPs y dos regiones H II con el espectrógrafo OSIRIS con el GTC. De la literatura se obtuvieron datos para otras 13 NPs y tres regiones H II. Se derivaron las condiciones físicas y abundancias químicas para el O, N, Ne, Ar y S de forma consistente para 19 NPs y 4 regiones H II. Las abundancias en la muestra de NPs de NGC 6822 están ampliamente distribuidas mostrando valores para 12 + log (O/H) desde 7.4 hasta 8.2 y 12 + log (Ar/H) desde 4.97 hasta 5.80. Se pueden diferenciar dos grupos de NPs: uno donde las progenitoras son viejas con baja metalicidad (12 + log (O/H) $<$ 8.0 y 12 + log (Ar/H) $<$ 5.7) y otro con progenitoras jóvenes con metalicidades similares a las de las regiones H II. Los objetos viejos están distribuidos en un volumen más grande que los jóvenes. En esta galaxia, se encontró que una fracción importante de NPs (más de 30 %) están muy enriquecidas en N (NP tipo I Peimbert). Además, cerca del 60 % de la muestra presenta alta ionización (He^{++}/He $\geq$ 0.1), con una estrella central con temperatura efectiva mayor que 100 000 K. Al comparar con los modelos de evolución estelar de Karakas (2010) y Fishlock et al. (2014), para los cocientes de abundancia de N/O, se obtiene que las NPs debieron tener masas iniciales menores que 2 $M_{\odot}$. Estos modelos para estrellas con 2-3 $M_{\odot}$ parecen producir demasiado ^{22}Ne en la superficie estelar al final de la AGB. Por otro lado, al comparar con los modelos de evolución estelar de Ventura et al. (2013, 2014,?) se encuentra una mejor concordancia entre las observaciones y los cocientes N/O y Ne/H predichos para estrellas con masas iniciales cercanas a 4 $M_{\odot}$.

A&A 586, A59 (2016)
DOI: 10.1051/0004-6361/201527265

Astronomy & Astrophysics

The planetary nebulae and H II regions in NGC 6822 revisited. Clues to AGB nucleosynthesis

Jorge García-Rojas[1,2], Miriam Peña[3], Sheila Flores-Durán[3], and Liliana Hernández-Martínez[3,4]

[1] Instituto de Astrofísica de Canarias, 38205 La Laguna, Tenerife, Spain
e-mail: jogarcia@iac.es
[2] Universidad de La Laguna, Dept. Astrofísica, 38206 La Laguna, Tenerife, Spain
[3] Instituto de Astronomía, Universidad Nacional Autónoma de México, Apdo. Postal 70-264, Méx. D. F., 04510 México, Mexico
[4] Instituto de Ciencias Nucleares, Universidad Nacional Autónoma de México, Apdo. Postal 70-543, Méx. D. F., 04510 México, Mexico

Received 28 August 2015 / Accepted 18 October 2015

ABSTRACT

Aims. The chemical behaviour of an ample sample of planetary nebulae (PNe) in NGC 6822 is analysed.
Methods. Spectrophotometric data of 11 PNe and two H regions were obtained with the OSIRIS spectrograph attached to the Gran Telescopio Canarias. Data for other 13 PNe and three H regions were retrieved from the literature. Physical conditions and chemical abundances of O, N, Ne, Ar, and S were derived in a consistent way for 19 PNe and 4 H regions.
Results. Abundances in the PNe sample are widely distributed showing 12 + log (O/H) from 7.4 to 8.2 and 12 + log (Ar/H) from 4.97 to 5.80. Two groups of PNe can be differentiated: one old with low metallicity (12 + log (O/H) < 8.0 and 12 + log (Ar/H) < 5.7) and another younger one with metallicities similar to the values for H regions. The old objects are distributed in a larger volume than the young ones. An important fraction of PNe (over 30%) was found to be highly N-rich (Peimbert Type I PNe). Such PNe occur at any metallicity. In addition, about 60% of the sample presents high ionization ($He^{++}/He \geq 0.1$), possessing a central star with effective temperature higher than 100 000 K. Possible biases in the sample are discussed. From comparison with stellar evolution models by Karakas (2010) and Fishlock et al. (2014) of the observed N/O abundance ratios, our PNe should have had initial masses that are lower than 4 $M_{\odot}$, although if the comparison is made with Ne vs. O abundances, the initial masses should have been lower than 2 $M_{\odot}$. It appears that these models of stars of 2–3 $M_{\odot}$ are producing too much ^{22}Ne in the stellar surface at the end of the AGB. On the other hand, the comparison with another set of stellar evolution models with a different treatment of convection and on the assumptions about the overshoot of the convective core during the core H-burning phase, provided there is reasonable agreement between the observed and predicted N/O and Ne/H ratios if initial masses of more massive stars are about 4 $M_{\odot}$.

Key words. ISM: abundances – HII regions – planetary nebulae: general – galaxies: abundances – galaxies: dwarf – stars: AGB and post-AGB

1. Introduction

The barred irregular galaxy NGC 6822 (IBs(m), also known as DDO209), is one of the most interesting galaxies in the Local Group. Half way between the Milky Way and Andromeda, (Gieren et al. 2006, reported a distance modulus of 23.31 ± 0.02), it presents several very interesting characteristics that have made it the subject of intense studies.

NGC 6822 contains different populations with different spatial distributions and kinematics. Its optical structure is dominated by a bar that is 8′ long (about 1.1 kpc), oriented almost N-S, and it contains a huge disk of H of about 6 × 13 kpc at a position angle (PA) of 130° centred on the optical centre (de Blok & Walter 2000; Weldrake et al. 2003). In addition, a huge spheroidal stellar distribution with its long axis at PA of 64.5° (almost perpendicular to the H disk), composed mainly of intermediate-age stars, has been found (Letarte et al. 2002; Battinelli et al. 2006). Interestingly, the H disk and the stellar spheroid do not share the same kinematics. The stellar spheroid has a systemic radial velocity $v_{sys} = -32.9$ km s^{-1}, and it rotates around its minor axis with radial velocities extending from 20 to −70 km s^{-1} (Demers et al. 2006), while the H disk shows a systemic velocity $v_{sys} = -57$ km s^{-1} and rotates around an axis almost orthogonal to the main axis of the spheroid, with velocities extending from −51 km s^{-1} to 100 km s^{-1} (de Blok & Walter 2006). A recent study of several stellar clusters in NGC 6822 (Hwang et al. 2014) reveals that the clusters seem to show completely different kinematics with a mean radial velocity of −88 ± 22.7 km s^{-1}.

In recent years we have been analysing the PN population in this galaxy and other galaxies and its relation with other objects (e.g., Peña et al. 2007 for NGC 3109; Hernández-Martínez et al. 2009, 2011, for NGC 6822; Stasińska et al. 2013 for NGC 300).

Chemically, NGC 6822 is a metal-poor galaxy similar to the SMC, with an interstellar medium (ISM) abundance of about 0.2 $Z_{\odot}$ (Richer & McCall 2007). Hernández-Martínez & Peña (2009) discovered 26 PN candidates in NGC 6822, and Hernández-Martínez et al. (2009) analysed the chemical abundances of a limited sample of them (11 objects), showing that the studied planetary nebulae (PNe) belong to two groups of different ages (1–3 Gyr and 3–9 Gyr) and different abundances, the first one with a composition similar to the present ISM and

the older one with abundances a factor of 2 lower. By studying abundances in H regions, they also found that the ISM located in the 2 kpc around the centre is chemically homogeneous, showing 12+log (O/H) = 8.06 ± 0.04.

Carigi et al. (2006) constructed chemical evolution models that fit the photometric properties of NGC 6822 computed by Wyder (2001, 2003) and derived a robust star formation history (SFH) for this galaxy. Detailed galactic chemical evolution models were computed by Hernández-Martínez et al. (2009, 2011) using PNe and H region abundances as constraints with no conclusive results. One of the two best models reproduces the abundances of O, Ne, S, Ar, and C derived from collisionally excitation lines (CELs) if the most massive star in the initial mass function has a mass $M_{up} = 40\ M_{\odot}$. The other model reproduces the abundances obtained from recombination lines (RLs, which are about a factor of 2 higher), if a $M_{up} = 80\ M_{\odot}$ is assumed. This is a direct effect of the abundance discrepancy problem, a still unresolved problem for photoionized nebulae, which consists in the well known fact that abundances obtained from RLs are systematically larger than those obtained from CELs of the same ion (e.g., García–Rojas & Esteban 2007; Liu 2012; Esteban et al. 2009). This effect is generally parametrized by the abundance discrepancy factor (ADF), which is defined as the ratio between abundances obtained from RLs and CELs. The ADF is usually between 1.5 and 3, but in PNe it has a significant tail that extends to much higher values, up to 120 (Corradi et al. 2015a). By analysing high-resolution spectra, Flores-Durán et al. (2014) demonstrate that the kinematics of PNe is closer to the one shown by the stellar spheroid than to the H disk, thus PNe would belong to the intermediate age population.

In this work we revisit the PN population in order to analyse the chemical behaviour of a larger sample of objects. New data were obtained from observations with the Gran Telescopio Canarias (GTC). In Sect. 2 we present the observations and data reduction. Section 3 is devoted to discussing the true nature of the sample. In Sect. 4 the physical conditions (electron temperatures and densities) and ionic abundances of a wide sample of objects are calculated. In Sect. 5 the total abundances are derived and discussed in comparison with stellar evolution models from the literature. Our results are presented in Sect. 6, and the final summary is found in Sect. 7.

2. Observations and data reduction

Long-slit spectroscopy was performed with the OSIRIS spectrograph attached to the GTC, which was in service mode during 2014[1]. Three exposures of 900 s each were obtained for each slit position. A binning of 2×2 was used. Grism R1000B (IR_G3.2) was employed to cover from 3630 to 7500 Å with an effective resolution of ∼1000 at 7510 Å. This wavelength range and resolution are well suited to detecting the main plasma diagnostic line ratios, which are useful for electron temperature and electron density determinations in the nebula, which are crucial for an accurate ionic abundance determination.

The slit size was 6.8 arcmin long by 1.5 arcsec wide. Slits were oriented in a mode where two or more objects were observed simultaneously in each observing block (OB) to save exposure time. The log of observations is presented in Table 1, where the slit position angle and observed objects in each OB are included. Because PNe are faint objects, most of the time a blind offset from a nearby field star was needed to place the objects in the slit. In total we observed 11 PN candidates and two faint H regions. The effect of atmospheric differential refraction was minimized by observing NGC 6822 close to culmination, which translates into slit orientations that are very close to the parallactic angle (differences less than 20–30°). This was not the case for OB2 where slit position was more than 60° away from parallactic angle; however, spectra of PN 25 and PN 26 were not useful for our purposes, probably owing to large slit losses.

[1] GTC programme number is GTC5-14AIACMEX, and 6 h of observing time were awarded. The observing time was divided in 6 observing blocks (OB), one hour each, of which 45 min were used for scientific observations.

Table 1. Log of observations with GTC.

Block	Date	Slit PA[a]	A.M.	Objects[b], night condition
OB1	2014-06-02	−26.4°	1.387	PN 2, PN 8, dark clear
OB2	2014-06-03	+54.4°	1.397	PN 25, PN 26, dark spectr.
OB3	2014-06-23	−10.3°	1.502	PN 23, PN 24, dark clear
OB4	2014-06-24	+1.3°	1.380	PN 11, PN 15, dark clear
OB5	2014-06-27	−0.35°	1.405	PN 9, PN 22, dark phot.
OB6	2014-06-27	+3.8°	1.389	PN 13, H II, H III, dark phot.

Notes. Exposure time was always 3 × 900 s, for each OB. [(a)] Slit size was always 6.8 arcmin ×1.5 arcsec. [(b)] PN names as in Hernández-Martínez & Peña (2009).

Observed 2D spectra were bias-subtracted and flat-fielded. Afterwards the spectra were extracted, and a careful sky subtraction was made, especially in the red zone where many sky lines appear. The extraction window was chosen in such a way that all the PN nebular emission was included. For H regions, which are more extended, the extraction window was 3″ and generally it does not include the whole object. The standard star Ross 640 was used for flux calibration. Ne and Hg-Ar lamps were observed in daytime for spectral calibration. Calibrated spectra of PNe and two H regions are shown in Fig. A.1.

Dereddened nebular line fluxes are presented in Table A.1, which for each object, includes the logarithmic reddening correction, c(Hβ), and the Hβ observed flux. c(Hβ) was derived from the Balmer ratio Hα/Hβ, by assuming Case B (Storey & Hummer 1995). No underlying absorption was considered to correct Hα and Hβ emission of H regions since these lines have a very large equivalent width. In the case of PNe, the central stars are very faint, and no underlying absorption is expected to affect the nebular lines. An additional object observed, but not included in Table A.1, is PN 26 for which only Hα was detected with a flux of 7.93E-17 erg cm^{-2} s^{-1}.

Additional spectroscopic data were obtained from the literature. The line fluxes reported by Hernández-Martínez et al. (2009) from VLT-FORS2 observations for PN 4, PN 5, PN 6, PN 7, PN 10, PN 12, PN 14, PN 16, PN 18, PN 19, PN 21, and H 15; those by Richer & McCall (2007), from observations with the Canada-France-Hawaii (CFH) telescope and the Multi-Object Spectrograph MOS, for PN 17 and PN 20, and data published by Peimbert et al. (2005) for the H regions H V and H X: all were retrieved and physical conditions and chemical abundances recalculated, following the same procedure as for our GTC data to have a consistent data set of abundances.

3. The true nature of objects observed with GTC

At the distance of NGC 6822, PN candidates can be easily mixed up with very compact H regions, therefore spectroscopic data are needed to segregate both types of objects. In our sample of 11 PN candidates observed with GTC, we found that the He λ4686 emission line is present (and measurable) in the

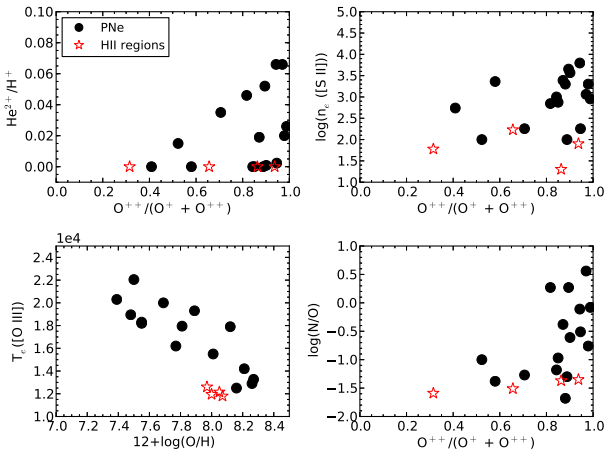

Fig. 2. Diagrams illustrating observed properties that allow differentiatin between PNe and H regions in NGC 6822.

objects named PN 8, PN 23, and PN 24, therefore their PN nature is confirmed since it is not expected that H regions emit such a high ionization line. In addition, the [O] λ5007/Hβ line ratio is larger than 3 in the objects PN 2, PN 11, and PN 13, also confirming their PN nature. The objects PN 9, PN 15, PN 22, PN 25, and PN 26 are very faint with observed F(Hβ) lower than about 2×10^{-16} erg cm^{-2} s^{-1}, and no (or very faint) [O] λ5007 or He λ4686 emission were detected, thus their PN nature is still unconfirmed, although the faintness of Hβ, the stellar appearance, and the lack of a detectable central star support their PN nature. In particular, we want to point out the case of PN 25, for which the [N] $\lambda\lambda$6548, 6583 lines are stronger than Hα (see Fig. A.1), which makes it a good candidate for a Peimbert Type I PN. As mentioned above, only Hα was detected for PN 26.

By considering the 11 objects confirmed as PNe by Hernández-Martínez et al. (2009), the two observed by Richer & McCall (2007), and the six objects observed with GTC and confirmed as PNe in this work, we find that 19 of the 26 PN candidates reported by Hernández-Martínez & Peña (2009) are true PNe, and the others are highly probable PNe, thus indicating that the criteria for selecting PN candidates in external galaxies proposed by these authors are very good. However, as we see in the discussion, these criteria, which were designed to mainly select high-luminosity ([O] λ5007) PNe (useful for building the planetary nebula luminosity function, PNLF), lead to ignore a number of PNe, in particular those with low excitation and low [O] λ5007 flux. Our sample therefore shows some bias that will be discussed later. In Sect. 5 we present Fig. 2, which shows some diagrams that are useful for distinguishing between PNe and compact H regions.

4. Physical conditions and ionic chemical abundances

All the available diagnostic line ratios were used to derive the physical conditions. Electron temperatures were calculated from [O] $\lambda\lambda$4363/5007 and [N] $\lambda\lambda$5755/6583 intensity ratios, while densities were derived from [S] $\lambda\lambda$6717/6731 and [Ar] $\lambda\lambda$4711/4740 intensity ratios. For H V and H X, we can also compute electron temperatures from the [O] $\lambda\lambda$3727/7325 intensity ratio and electron densities from the [O] $\lambda\lambda$3726/3729 and the [Cl] $\lambda\lambda$5517/5537 line ratios; the last ratio was also measured for H 15 (see Table 2 of Hernández-Martínez et al. 2009). Physical conditions and ionic abundances were computed using P N , a new python-based code for the analysis of nebular data (Luridiana et al. 2015). The atomic data set used is listed in Table 2.

In general, a two-temperature model was adopted to derive ionic abundances, where T_e([O]) was used for high ionization species (O^{++}, Ne^{++}, Ar^{++}, Ar^{+3}, He^+, and He^{++}), while T_e[N] was used for the low-ionization ones (N^+, O^+, S^+, and S^{++}). For H V, the weighted average of T_e([N]) and T_e([O]) was used to compute abundances of low ionization species. When only one temperature was available, it was used for all the ions. The density derived from the [S] density sensitive line ratio was used in all the cases when available. In the objects where other diagnostics were available, the densities obtained were consistent within the uncertainties with the density derived from [S] lines. When no density diagnostic was observed, a density of 1000 or 2000 cm^{-3} was adopted, depending on the case (see Tables A.2 and 4).

Uncertainties in the ionic abundances were calculated by applying Monte Carlo simulations. We generated 500 random values for each line intensity with a sigma equal to the uncertainty quoted for the line intensities. In Table 3 we show the list of lines used to derive ionic abundances.

Physical conditions and ionic abundances, with their respective errors, are presented in Table A.2 for data from the VLT and the CFH telescope and for H V and H X, and in Table 4 for data obtained with the GTC. Although we have estimated

Table 2. Atomic data set used for collisionally excited lines.

Ion	Transition probabilities	Collisional strengths
N^+	Froese Fischer & Tachiev (2004)	Tayal (2011)
O^+	Froese Fischer & Tachiev (2004)	Kisielius et al. (2009)
O^{2+}	Froese Fischer & Tachiev (2004)	Storey et al. (2014)
	Storey & Zeippen (2000)	
Ne^{2+}	Galavís et al. (1997)	McLaughlin & Bell (2000)
Ne^{4+}	Galavís et al. (1997)	Dance et al. (2013)
	Bhatia & Doschek (1993)	
S^+	Podobedova et al. (2009)	Tayal & Zatsarinny (2010)
S^{2+}	Podobedova et al. (2009)	Tayal & Gupta (1999)
Cl^{2+}	Mendoza (1983)	Butler & Zeippen (1989)
Ar^{2+}	Mendoza (1983)	Galavís et al. (1995)
	Kaufman & Sugar (1986)	
Ar^{3+}	Mendoza & Zeippen (1982)	Ramsbottom & bell (1997)
Ar^{4+}	Mendoza & Zeippen (1982)	Galavís et al. (1995)
	Kaufman & Sugar (1986)	
	LaJohn & Luke (1993)	

Table 3. Lines used for ionic abundance determinations.

Ion	Line
N^+	[N] $\lambda\lambda$6548, 6584
O^+	[O] $\lambda\lambda$3726+29, 7320+30
O^{++}	[O] $\lambda\lambda$4959, 5007
Ne^{++}	[Ne] $\lambda\lambda$3868
Ne^{+4}	[Ne] λ3425
S^+	[S] $\lambda\lambda$6717+31, 4068+76
S^{++}	[S] λ6311
Cl^{++a}	[Cl] λ5517+37
Ar^{++}	[Ar] $\lambda\lambda$7136, 7751
Ar^{+3}	[Ar] $\lambda\lambda$4711+40
Ar^{+4}	[Ar] λ7005

Notes. [(a)] Only for VLT H region data.

Table 4. Ionic abundances in NGC 6822 objects from GTC data.

Object	PN 2	PN 8	PN 11	PN 13	PN 23	PN 24	H II	H III
T_e([O]) (K)	18 300 ± 3800	20 300 ± 3900	–	20 000 ± 3000	<14 700	16 300 ± 3300	<16 700	12 600 ± 1000
T_e([N]) (K)	–	–	17 650 ± 5750	–	–	15 850 ± 8700	–	–
n_e([S]) (cm^{-3})	750^{+3000}_{-600}	6250:	550^{+1250}_{-400}	<100	100^{+300}_{-75}	200^{+550}_{-140}	<100	60^{+100}_{-40}
Ion	12 + log (X^{+i}/H^+)							
He^+	11.26 ± 0.13	$10.57^{+0.13}_{-0.11}$	–	11.08 ± 0.06	$10.89^{+0.13}_{-0.16}$	<11.15	11.02 ± 0.06	10.96 ± 0.02
He^{++}	<9.73	10.82 ± 0.04	–	<10.19	>10.40	$10.79^{+0.06}_{-0.08}$	–	–
N^+	$5.68^{+0.22}_{-0.14}$	$5.84^{+0.18}_{-0.15}$	$7.78^{+0.21}_{-0.18}$	5.41 ± 0.20	>6.62	6.60:	>6.18	$6.15^{+0.10}_{-0.08}$
O^+	6.72:	5.83:	<7.51	$6.71^{+0.32}_{-0.18}$	>7.43	–	>7.49	$7.74^{+0.14}_{-0.11}$
O^{++}	$7.47^{+0.21}_{-0.15}$	$7.05^{+0.26}_{-0.15}$	$7.35^{+0.31}_{-0.24}$	$7.61^{+0.19}_{-0.10}$	>8.07	$7.83^{+0.29}_{-0.17}$	>7.07	$7.59^{+0.12}_{-0.08}$
Ne^{++}	$6.74^{+0.33}_{-0.30}$	<6.08	–	–	–	–	–	$6.77^{+0.15}_{-0.11}$
S^+	$4.44^{+0.25}_{-0.17}$	$4.45^{+0.38}_{-0.35}$	5.90 ± 0.23	$4.78^{+0.14}_{-0.11}$	>5.51	$5.28^{+0.31}_{-0.23}$	>5.72	$5.85^{+0.09}_{-0.07}$
S^{++}	–	–	–	–	–	–	–	–
Ar^{++}	$4.83^{+0.18}_{-0.16}$	$4.79^{+0.22}_{-0.19}$	5.77 ± 0.28	<5.22	>5.56	$5.51^{+0.20}_{-0.14}$	>5.43	$5.65^{+0.10}_{-0.07}$
Ar^{+4}	–	$4.98^{+0.23}_{-0.26}$	–	–	–	–	–	–

Notes. Abundances in 12 + log (X^{+i}/H^+). Colons indicate errors larger than a factor of two.

Table 5. Total abundances in NGC 6822 from GTC data.

Elem/object	PN 2	PN 8	PN 11	PN 13	PN 23	PN 24	H II	H III
He	11.27 ± 0.12	11.01 ± 0.05	–	11.13 ± 0.06	$11.01^{+0.09}_{-0.13}$	<11.30	>11.02	–
N	$6.58^{+0.21}_{-0.17}$	7.28 ± 0.32	$8.27^{+0.27}_{-0.14}$	$6.39^{+0.16}_{-0.23}$	>7.38	–	6.30:	6.38 ± 0.08
O	$7.55^{+0.25}_{-0.18}$	$7.39^{+0.25}_{-0.14}$	7.74:	$7.69^{+0.20}_{-0.10}$	>8.23	>7.83	>7.63	$7.97^{+0.13}_{-0.10}$
Ne	6.76:	<6.42	–	–	–	–	–	$6.88^{+0.15}_{-0.12}$
S	$5.56^{+0.28}_{-0.22}$	5.99:	–	6.01 ± 0.10	>6.49	>5.28	–	–
Ar	$4.97^{+0.17}_{-0.13}$	$5.30^{+0.20}_{-0.15}$	6.50:	<5.40	>5.74	>5.51	5.48:	$5.69^{+0.10}_{-0.07}$
$L(H\beta)/L_\odot$	13.95	21.79	0.22	56.85	3.27	7.07	–	

Notes. Abundances in 12 + log (X/H). Colons indicate errors larger than a factor of two.

some ionic abundances for the H region H II, these values are extremely uncertain because no electron temperature could be computed for this object, therefore it will not be considered for the discussion of total abundances in H regions.

For elements heavier than He, we only considered abundances obtained from CELs. It is well known that abundances obtained from RLs are generally higher than those obtained from CELs (see Sect. 1), but although some oxygen RLs have been detected in H V and H X spectra (Peimbert et al. 2005), we do not detect oxygen RLs in the rest of our sample objects. Moreover, some authors claim that the ADF can be considered almost constant for H regions in Galactic and extragalactic domain (García–Rojas & Esteban 2007; Peña-Guerrero et al. 2012), but this is not necessarily true for PNe (McNabb et al. 2013), making any conclusion obtained from assuming a "canonical" ADF unreliable. However, if we consider that PNe in NGC 6822 follow the behaviour of Galactic and extragalactic H regions and the bulk of PNe in our Galaxy, the effect of considering the ADF would be much lower than the quoted uncertainties in heavy element abundance ratios and would affect elemental abundances by adding ∼0.2 dex to the CELs abundances.

5. Total abundances and AGB nucleosynthesis

To derive the total abundance of an element, we must add the determined ionic abundances and correct for the unseeing ions by employing ionization correction factors (ICF). Very recently, a new set of ICFs for PNe has been presented by Delgado-Inglada et al. (2014). These ICFs were computed from a large grid of photoionization models, covering a wide range of values in the parameter space, thus improving significantly the previous ICF sets for PNe in the literature. We checked the validity range of the ICFs, depending on the excitation of each PN. In the majority of the cases, the ICFs can be applied; however, four PNe (PN 12, PN 16, PN 18, and PN 21) showed $O^{2+}/(O^+ + O^{2+}) \geq 0.95$, which is out of the validity range of the ICF proposed by Delgado-Inglada et al. (2014) for N, S, and Ar. In such cases we compared the results obtained with the ICF provided by Delgado-Inglada et al. (2014) for N with the classical ICF scheme, i.e., $N/O \sim N^+/O^+$, and we found average differences of about ±0.10 dex, which are within the uncertainties of the total abundance determinations; moreover, we do not find any unexpected behaviour of the abundances of Ar and S on these objects (see Sect. 5.3), and therefore, to have a homogeneous analysis, we applied the Delgado-Inglada et al. (2014) scheme to these objects. For H regions we used the ICF expressions for mid-metallicity ($7.6 < (12 + \log(O/H) < 8.2$) proposed by Izotov et al. (2006). The intrinsic uncertainties of the Delgado-Inglada et al. (2014) ionization correction factors are not propagated in our analysis and only error propagation of the ionic abundances was considered in our Monte Carlo simulations.

Total abundances for 19 PNe are listed in Table A.3 for data from the VLT and CFH observations and in Table 5 for data from the GTC. In addition, the chemical abundances of four H regions – H 15 and H III observed by us and H V and H X from the work by Peimbert et al. (2005) for which we recalculated the abundances – have been included for comparison. The behaviour of elemental abundances are shown in Figs. 3–7, and they are discussed in the following. In these plots we have not included uncertain determinations of abundances (those with errors quoted as :) or the upper and lower limits to the abundances.

In Tables A.3 and 5 we also list the total luminosity $L(\mathrm{H}\beta)$ of PNe in solar units for all the objects for which F(Hβ) and c(Hβ) are published. A distance of 459.19 kpc was assumed for NGC 6822 (Gieren et al. 2006). After determining physical conditions and chemical abundances, in Fig. 2 we present some diagrams comparing the properties of PNe and H regions that clearly show the differences between these two type of photoionized nebulae. It is evident that spectroscopic analysis allows a reliable classification on a very solid basis.

5.1. O abundances

In the upper panel of Fig. 3, we present 12 + log (O/H) vs. log ($L(\mathrm{H}\beta)/L_{\odot}$). In Tables A.3 and 5, it is observed that PNe in NGC 6822 show $L(\mathrm{H}\beta)$ smaller than 60 $L_{\odot}$, while H regions (even the compact ones) are expected to be much brighter; for instance, the compact H 15 has $L(\mathrm{H}\beta)$ larger than 300 $L_{\odot}$. $L(\mathrm{H}\beta)$ for the most extended H regions are not presented because only a fraction of the nebula was observed. Regarding O abundances, 12 + log (O/H) values in PNe show a wide range from 7.39 to 8.27, with the two brightest PNe showing intermedium O abundances. We do not find a particular trend between $L(\mathrm{H}\beta)$ and the O/H abundance, although it is worth noticing that the faintest objetcs show very low O abundances. The same is observed in the lower panel of Fig. 3, where we plot L([O] λ5007) instead of $L(\mathrm{H}\beta)$ and where no particular trend is again found.

In their Fig. 4, Corradi et al. (2015b) found for M 31 PNe that there seems to be a tendency toward decreasing metallicity with decreasing [O] luminosity. They also seem to find a similar tendency when plotting M 33 data from Magrini et al. (2009). Similar results have already been indicated by Stasińska et al. (1998) for the LMC, SMC, and the Milky Way. From our data, this tendency is not evident, although as pointed out above, the faintest PNe of our sample show low metallicities, while the bright ones have a wide spread in O/H abundances.

5.2. He, N, and O

Figure 4 shows the behaviour of 12 + log (N/H) as a function of 12 + log (He/H) (upper panel) and log (N/O) ratio vs. 12 + log (O/H) (lower panel) for PNe (black dots) and H regions (red stars). No correlation between these quantities is evident. In comparison with the H regions, most of the PNe are both He-rich and N-rich, as occurs in all the samples analysed by many authors for different galaxies. This indicates that central stars of PNe are providing large amounts of He and N to the ISM as a consequence of the first and second dredge-up events experienced during the AGB phase. The second dredge-up occurs for the more massive stars with $M > 3\ M_{\odot}$. Such dredge-up processes enrich the stellar surface with N produced via the CNO cycle, but it is apparent from this figure that, since no correlation exists, the ON-cycle is not a significant contributor to

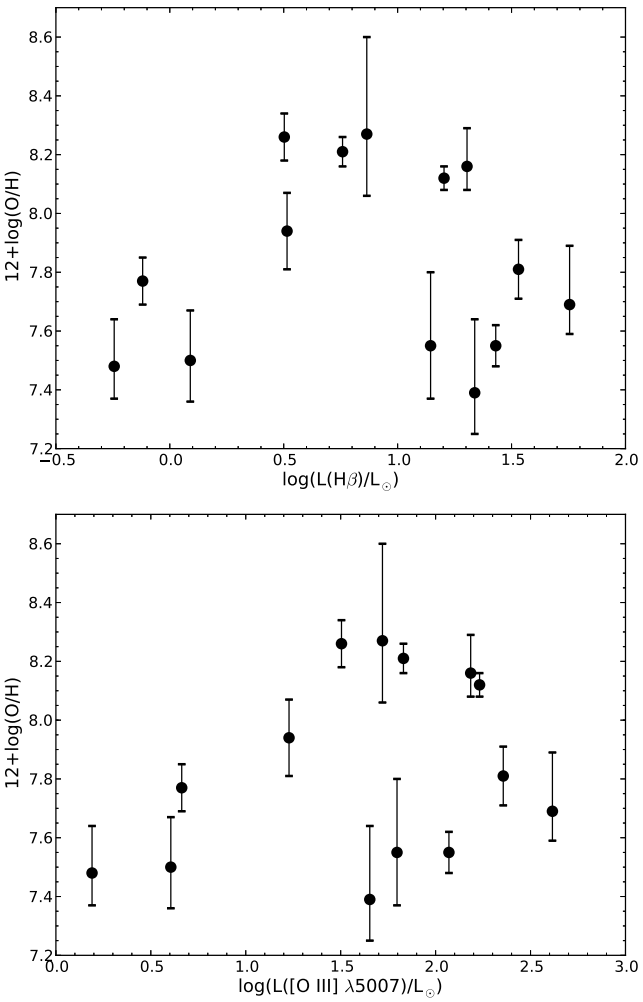

Fig. 3. *Above*: 12 + log (O/H) vs. $L(\mathrm{H}\beta)$; *below*: 12 + log (O/H) vs. L([O]5007) for PNe in NGC 6822.

the N nucleosynthesis yield, and most of the N should be contributed by the CN-cycle in these stars. However, a note of caution should be introduced here, because Karakas et al. (2009, and references therein) point out that PNe with rapid rotating progenitor stars can also reflect high He and N abundances in the gas owing to rotation changes the internal structure of the star, resulting in high He/H and N/O ratios in the surface, before the AGB phase. Extreme N enrichment is observed in some PNe (they would be Peimbert Type I PNe) whose central stars (in principle the most massive ones) produce extra N enrichment by experiencing envelope-burning conversion to N of dredged-up primary C (phenomenon known as "hot-bottom burning", hereinafter HBB). Additionally, the role of the binary evolution of low-mass stars cannot be ruled out as the origin of a fraction of highly N-rich PNe (see e.g. Moe & De Marco 2006, and references therein). If we consider Type I PNe as those with a N/O abundance ratio greater than 0.5 (see discussion in Hernández-Martínez et al. 2009, for adopting this value), we found that there are six Type I PNe in our sample, representing one third of the whole analysed sample, although two of them have very uncertain N and/or O abundances and are not represented in Fig. 4. Interestingly, in the lower panel of this figure, it is evident that these Type I PNe occur at any value of O/H (that

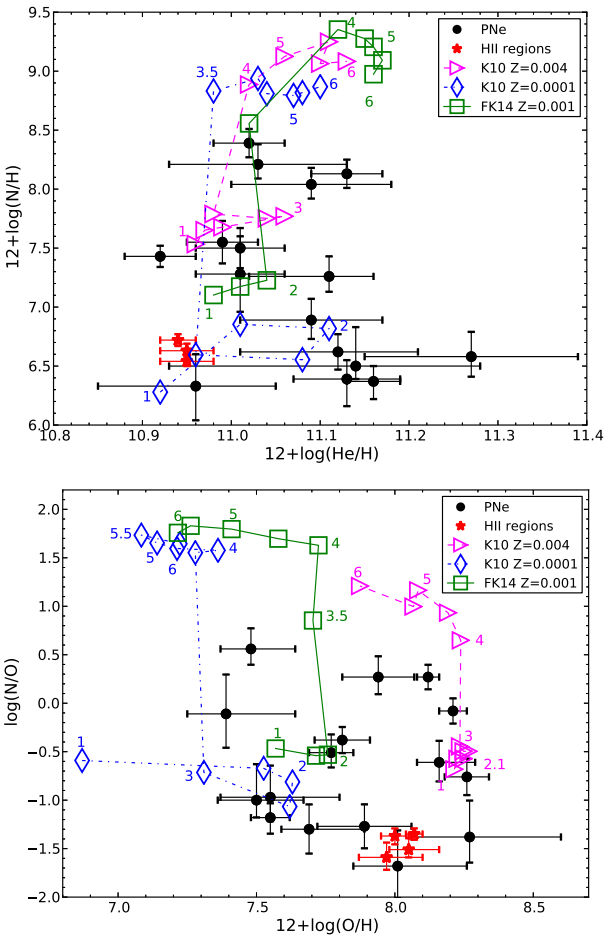

Fig. 4. 12 + log (N/H) vs. 12 + log (He/H) (*upper panel*) and log (N/O) vs. 12 + log (O/H) (*lower panel*) for PNe (in black) in NGC 6822. In red the H regions. Stellar evolution models for different metallicities by Karakas (2010, K10) (Z = 0.0001, blue diamonds; Z = 0.004, magenta triangles) and Fishlock et al. (2014, FK14) (Z = 0.001, green squares) have been included. Masses of the progenitors stars are shown for some models. See text for discussion.

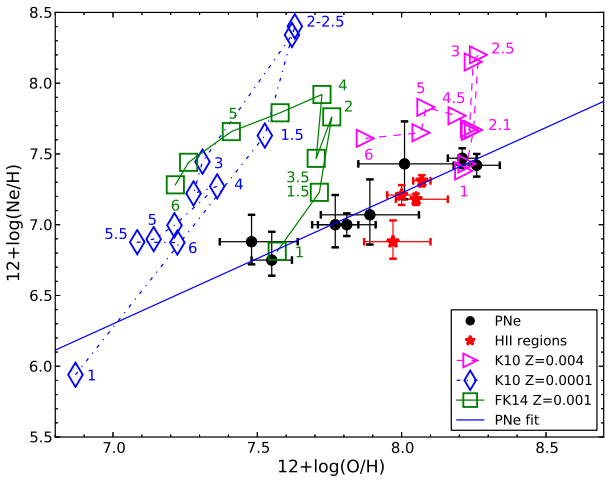

Fig. 5. 12 + log (Ne/H) vs. 12 + log (O/H), for PNe (in black) in NGC 6822. In red the H regions. The linear fit (including only PNe data) corresponds to 12 + log (Ne/H) = (0.925 ± 0.071) × (12 + log (O/H)) − (0.176 ± 0.566), with r = 0.88. Stellar evolution models for different metallicities, by Karakas (2010, K10) (Z = 0.0001, blue diamonds; Z = 0.004, magenta triangles) and Fishlock et al. (2014, F14) (Z = 0.0001, green squares) have been included. See text for discussion.

is, at any metallicity), and they are not restricted to the young (supposedly more massive) high-metallicity objects.

As said above, to check the influence of the selected ICF scheme on our results, we also computed total N abundances using the classical ICF scheme of N/O ∼ N^+/O^+, and we did not find any significant differences (on average, less than ±0.1 dex) between using the Delgado-Inglada et al. (2014) scheme and the classical one, with the exception of PN 11, whose N/O ratio decreases ∼0.26 dex using the classical ICF scheme, but this object is not included in Fig. 4 because it shows a very uncertain O/H ratio.

In Fig. 4 we have also included the behaviour predicted by the stellar evolution models by Karakas (2010) and Fishlock et al. (2014) for different metallicities. Model values correspond to the surface stellar abundances at the end of the AGB phase. The initial masses of stars have been tagged. In the upper panel of this figure, it is apparent that our objects have larger He/H abundances than what is predicted by the models. Only models with metallicity Z = 0.0001 would be in agreement with the He abundance shown by PNe with 12 + log(N/H) lower than 7.0.

In the lower panel of Fig. 4, it is found that our objects appear well demarcated by models with Z between 0.0001 and 0.004. As expected, models predict that more massive stars produce larger amounts of N, similar to the values shown by Type I PNe. According to these models, our objects would have had initial masses lower than 4 $M_\odot$; however, it should be noticed that no model predicts the low N/O ratio (log(N/O) > −1.0) shown by several of our PNe. Such stars should have had initial masses lower than 1 $M_\odot$, or the stellar evolution models could be predicting yields for N that are too large. The behaviour of these models is discussed further in Sect. 5.4.

5.3. The alpha elements: Ne, Ar, and S

The Ne/H vs. O/H abundance behaviour is shown in Fig. 5. Values derived for PNe and H regions are presented. A tight correlation is found between Ne and O abundances as occurs in any other sample of PNe and H regions (Henry 1989; García-Hernández & Górny 2014). This has been interpreted as Ne not being strongly altered by AGB evolution so that O and Ne grow in lock-step during the chemical evolution of galaxies. In the case of our PNe sample, the slope of the correlation is 0.93±0.07, which is similar to the slopes found for other PN samples; for instance, Leisy & Dennefeld (2006) report slopes of 1.13 for PNe in the LMC and 1.01 in the SMC.

Similar to what has been done with N, we checked the Ne/H ratio obtained using the ICF scheme by Kingsburgh & Barlow (1994). The differences between this ICF scheme and the one assumed in this work (Delgado-Inglada et al. 2014) are, on average, much smaller than the derived uncertainties (<0.05 dex) with the exception of two objects, PN 17 and PN 6, for which the Kingsburgh & Barlow scheme gives Ne/H ratios that are 0.48 and 0.26 dex larger, respectively. PN 6 is not shown in Fig. 5 owing to its uncertain Ne/H ratio.

In Fig. 5 we have also included the predictions of stellar evolution models by Karakas (2010) and Fishlock et al. (2014) for different metallicities. These models consider the yields of all the Ne isotopes: ^{20}Ne, ^{21}Ne, and ^{22}Ne. It is worth recalling that ^{20}Ne is the most abundant isotope, and it is not significantly

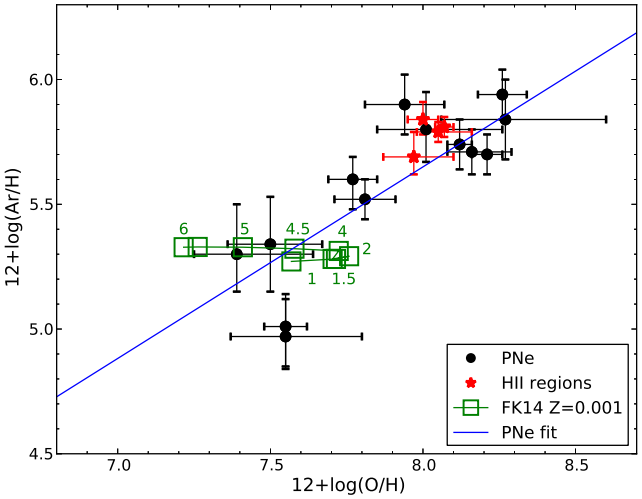

Fig. 6. Behaviour of 12 + log (Ar/H) vs. 12 + log (O/H). In red the H regions. The linear fits, including only PNe, corresponds to 12 + log (Ar/H) = (−0.494 ± 0.512) + (0.768 ± 0.064) × (12 + log (O/H)), with r = 0.79. The stellar evolution models for Z = 0.001 by Fishlock et al. (2014, F14) are included.

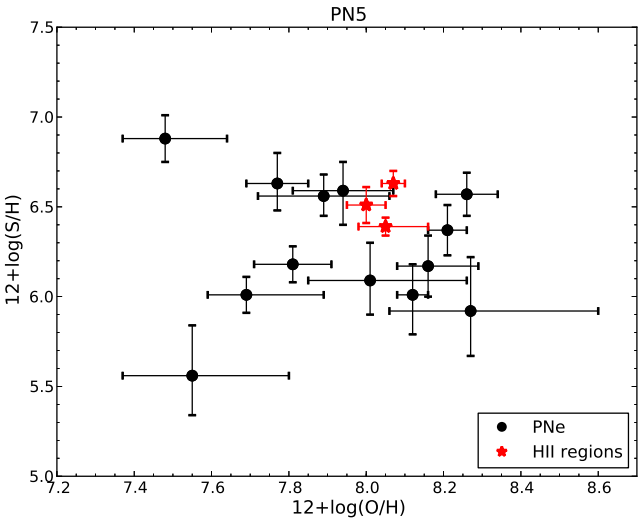

Fig. 7. Behaviour of 12 + log (S/H) vs. 12 + log (O/H), for PNe in NGC 6822. In red the H regions. No correlation exists. The H regions present larger S abundances than many PNe.

modified by nucleosynthesis during the AGB phase, but two α-captures may transform a ^{14}N into a ^{22}Ne that could be mixed to the surface in the third dredge-up episode, increasing the total Ne abundance. Interestingly, the models predict large Ne increases at very low metallicities. ^{22}Ne is efficiently produced and brought to the surface in stars with initial masses between ∼2 and 4 $M_{\odot}$, depending on the metallicity. Stars with higher masses are less efficient because ^{22}Ne diminishes as a consequence of an α capture that destroys it. Our objects are delimited by models with Z between 0.001 and 0.004. In this case we found that models predict excess of Ne, unless our objects have had initial masses lower than 1.5 or 2 $M_{\odot}$, which contradicts the results from the N/O vs. O/H diagram using the same set of models (see Fig. 4 in previous section). In Sect. 5.4 this subject is discussed more deeply.

The behaviour of Ar/H vs. O/H is presented Fig. 6. A correlation is also found for these elemental abundances. Although it is not as tight as in the case of Ne/H vs. O/H, it shows that O, Ne, and Ar are elements that evolve closely in lock-steps. Data for H regions have been included in this diagram (red dots). In this case the slope of the correlation (computed including PNe only) is 0.768 ± 0.064, significantly far from 1, which could indicate that O abundances are too large at the high-metallicity end, as would occur if O is enriched by stellar nucleosynthesis.

The predictions of evolution models by Fishlock et al. (2014) at Z = 0.001 are included in the graph. These models show clearly that Ar is not modified by stellar nucleosynthesis, independently of the initial stellar mass. In this case, the 12 + log (Ar/H) abundance has an almost constant value around 5.3.

S/H vs. O/H abundances are presented in Fig. 7. In this graph no correlation of S with O is found, although it should be expected, because S is also an α element produced in similar processes to O, Ne, and Ar. Probably this has to do with the difficulty of deriving the S total abundance for which no appropriate ICF exists (Henry et al. 2004). In this graph we see that S/H values in PNe spread in a wide range, and it is also seen that H regions show a S/H ratio similar to many PNe, but an important fraction of PNe present lower S/H than the values in H regions. Therefore the phenomenon known as "sulphur anomaly" (consisting in PNe showing sustantially lower S abundance than H regions at a given metallicity) is present in our PN sample. The reasons behind this phenomenon are still not clear, although as said above, it has been attributed mainly to deficient ICFs for calculating S abundance, particularly, to the uncertain contribution of S^{3+} to the total S. In our case, the use of the new ICFs proposed by Delgado-Inglada et al. (2014) has not improved the situation. On the other hand, some authors claim that the sulphur anomaly can be explained by the depletion of S into dust, especially in C-rich dust PNe (García-Hernández & Górny 2014). Computing abundances from S lines in IR spectra, where S^{3+} lines can be measured, would shed some light on this problem.

5.4. Testing other stellar evolution models

As said above, the comparison of the observed N/O abundances with predictions of stellar evolution models by Karakas (2010) and Fishlock et al. (2014) indicates that the initial masses of the observed PNe were lower than 4 $M_{\odot}$, contradicting the predictions of the same models for Ne/H vs. O/H (Fig. 5), from which the initial masses should have been lower than 2 $M_{\odot}$. Therefore we have decided to analyse the behaviour of models more deeply.

Karakas & Lattanzio (2003) have compared the Ne yield of their models with abundances of PNe of the Milky Way (Z = 0.02) and the Large Magellanic Cloud (Z = 0.008) to find that models agree with the observations except for the case of models with initial mass of 3 $M_{\odot}$ and Z = 0.008, which seem to predict too much Ne.

From the analysis of a sample of Galactic disk and bulge double chemistry (DC), O-rich dust (OC), and C-rich dust (CC) PNe, García-Hernández & Górny (2014) found that the average Ne/O at Z = 0.02 for their DC and OC PNe was slightly larger than those predicted by the models by Karakas (2010) without a partial mixed zone (PMZ); therefore, they conclude that including and varying the size of a PMZ can solve the observed behaviour. However, that is exactly the opposite of what we found in our sample. For our objects (which have Z < 0.004), we found that models with initial mass higher than 2 $M_{\odot}$ show too much Ne, in comparison with observations. We consider that

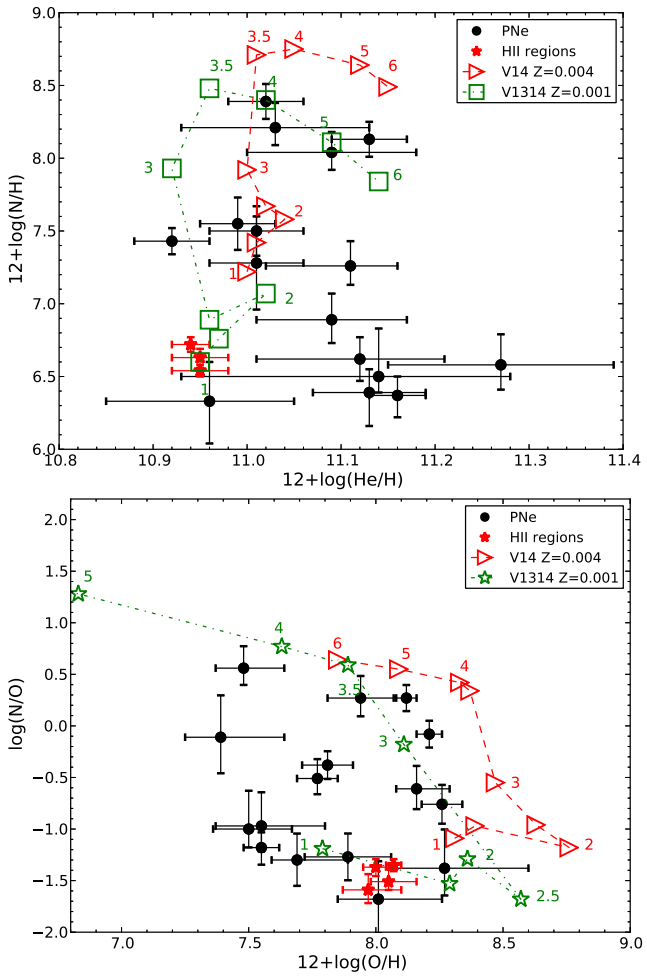

Fig. 8. Same as Fig. 4 but showing the predictions of stellar evolution models for $Z = 0.001$ (green squares) by Ventura et al. (2013, 2014b, V1314) and $Z = 0.004$ (red triangles) by Ventura et al. (2014a, V14). See text for discussion.

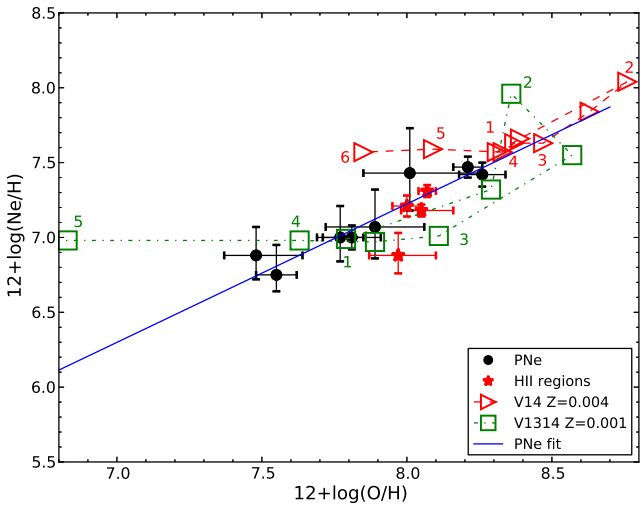

Fig. 9. Same as Fig. 5 but showing the predictions of stellar evolution models for $Z = 0.001$ (green squares) by Ventura et al. (2013, 2014b, V1314) and $Z = 0.004$ (red triangles) by Ventura et al. (2014a, V14). See text for discussion.

it is possible that such models are producing an excess of ^{22}Ne or that the efficiency of the third dredge-up should be diminished in those stars.

Very recently, Ventura et al. (2015) and Dell'Agli et al. (2015) have used a new generation of AGB stellar models that include dust formation in the stellar winds to constrain CNO abundances of PNe in the Magellanic Clouds, which have a metallicity slightly higher than but comparable to that of NGC 6822. These models were developed using the ATON evolutionary code, which stands apart from others in that it uses the Blöcker (1995) mass loss prescription and the full spectrum of turbulence (FST) convective model (Canuto & Mazzitelli 1991). These assumptions concern the overshoot of the convective core during the core H-burning phase and lead to a less efficient dredge-up and to a lower threshold mass for the activation of the HBB. A detailed description of these models are given in Ventura et al. (2014a) for $Z = 0.004$, in Ventura et al. (2013) for $Z = 0.001$ and $M > 3\ M_{\odot}$, and in Ventura et al. (2014b) for $Z = 0.001$ and $M \leq 3\ M_{\odot}$.

In Figs. 8 and 9 we explore the behaviour of 12 + log (N/H) vs. 12 + log (He/H) and log (N/O), and 12 + log (Ne/H) vs. 12 + log (O/H) with models by Ventura et al. (2013, 2014b) for $Z = 0.001$ and Ventura et al. (2014a) for $Z = 0.004$. It is found that they predict lower N/O ratios for intermediate-mass progenitors stars than the models by Karakas (2010) and Fishlock et al. (2014). Additionally, the lowest N/O ratios are reproduced by stars with initial masses lower than 2.5 $M_{\odot}$. It is important to stress than in the $Z = 0.001$ models, the HBB destroys O very efficiently in the more massive progenitors. In our sample there are several objects at 12 + log (O/H) < 7.8 that are not reproduced by the set of models shown here. Probably these objects could be reproduced by models at $Z = 0.0001$. In Fig. 8 (above), it is observed that Ventura et al. models do not reproduce the large He/H abundance found in the PNe with 12 + log(N/H) < 7.0).

Similar to what it was found for N, in Fig. 9 the observed Ne abundances are consistent with models of stellar progenitors with masses up to 4–5 $M_{\odot}$, which is in overall agreement with what we found in Fig. 8. This is because dredge-up events in Ventura et al. (2015) models are less efficient than the Karakas ones.

On the other hand, we checked the evolution of the surface abundances obtained from the Fishlock et al. (2014) models during the different thermal pulses (TP) and dredge-up events. In Fig. 10 we show the behaviour of the N/O and Ne/H surface abundances for models with initial masses of 3.5, 4, and 5 $M_{\odot}$ at different steps, from the first TP to the final surface abundances in steps of 10 TP, and we found that if the models are stopped significantly before (the amount of mass loss changes significantly) they can also reproduce the observed behaviour in N/O.

A deeper discussion of this subject is beyond the scope of this paper, but it would be important to analyse the predictions of models in comparison with the chemical abundances of different elements (C, N, O, Ne, Ar, etc.) observed in PNe at different metallicities, looking for a good agreement between observations and theory.

5.5. PNe populations

From a sample of 11 objects Hernández-Martínez et al. (2009) reported the presence of two PN populations, one older, of low metallicity with 12 + log (O/H) values lower than 7.9, and one younger, of high metallicity, including PNe showing 12 + log

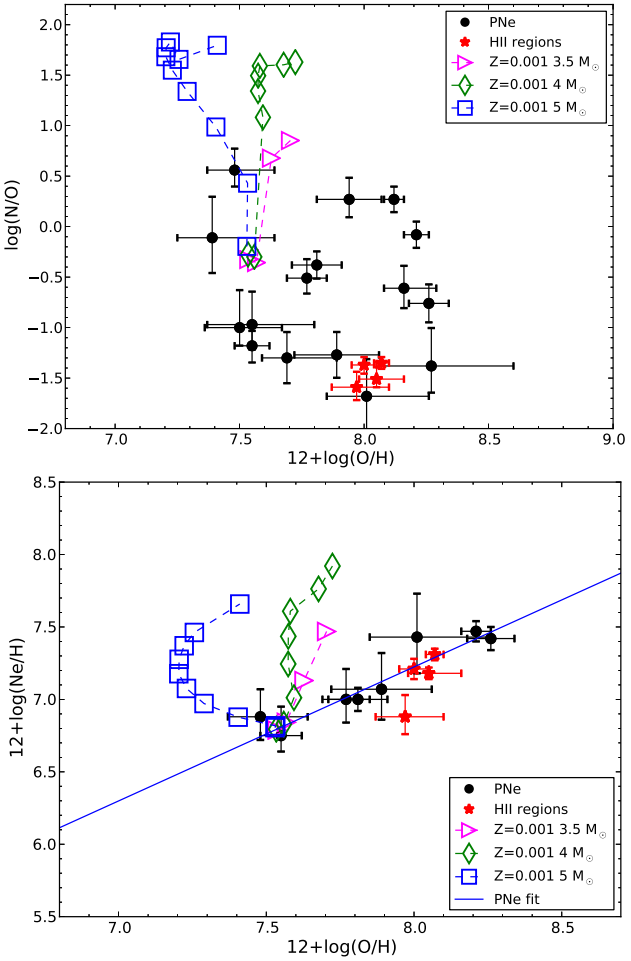

Fig. 10. Evolution of the surface abundances for models with $Z = 0.001$ and initial masses of 3.5, 4, and 5 $M_{\odot}$ of Fishlock et al. (2014). First point shows abundances after first TP and the last point represents the final surface abundances of the AGB model. The step between points is ~10 TP.

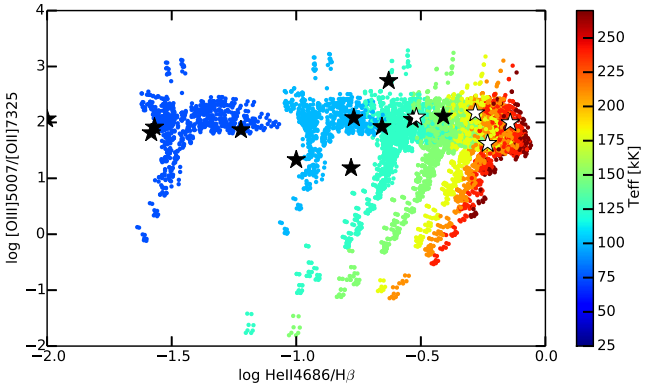

Fig. 11. λ5007/[O]λ7325 vs. He λ4686/Hβ as obtained from the Mexican Million Models data base by Morisset et al. (2015). Stellar temperatures can be obtained from this plot. Many of our PNe have stars with T higher than 10^5 K. The Type I PNe are indicated in white.

(O/H) abundances larger than 8.0 and similar to the H region abundances (the four H regions presented in Tables 7 and 8 show a very similar 12 + log (O/H) value with an average of 8.02 ± 0.05). In our extended PN sample, such a segregation does not seem so evident. However, there is only one PN with 12 + log (O/H) in the range from 7.9 to 8.0, therefore our sample still supports the idea of having two PN populations on the basis of O/H abundances.

By analysing the behaviour of Ar abundances in Fig. 6, two PN populations can also be differentiated, one showing 12 + log (Ar/H) lower than 5.7 and the other Ar/H similar to the values in H regions, which on average is 5.80 ± 0.10.

As said in the Introduction, Carigi et al. (2006) used Wyder (2003) data and proposed a star formation history representative of the whole galaxy. In their Fig. 4 presenting the star formation rate (SFR), a clear burst appears between 6 and 8 Gyr, followed by a fall in the SFR lasting up to about 10 Gyr, when a second star formation episode starts. These two episodes of star formation coincide with the ages assigned by Hernández-Martínez et. al (2011) to the PN two populations, between 3 and 9 Gyr for the older one and ages under 3 Gyr for the younger one. These PN ages were obtained from Allen et al. (1998, and references therein). Additionally, according to Rodríguez-González et al. (2015), the presence of a dip in the PNLF in NGC 6822 indicates that two important episodes of star formation should have occurred in order to obtain such a dip in the PNLF. Therefore, our finding of two PN populations in NGC 6822 and their ages corroborate the two star formation episodes found in the SFR by Carigi et al. (2006).

Regarding the Ar abundances, as expected within uncertainties, no PN shows Ar/H larger than H regions. However this is not the case of O, for which a few PNe have O/H slightly larger than H regions (see Fig. 6). Similar to the slope of the Ar/H vs. O/H correlation, this could indicate O-enrichment in the PN shell due to nucleosynthesis in the stellar interior. Such an enrichment has been predicted by some stellar evolution models for low-metallicity stars (see e.g. Marigo 2001) and from some nucleosynthesis models including extra mixing mechanism (Pignatari et al. 2013). Peña et al. (2007) find O-enrichment in the PNe of the low-metallicity irregular galaxy NGC 3109. Such an O-enrichment has also been found in some PNe of the Milky Way showing C-rich dust (Delgado-Inglada et al. 2015), and it is attributed to an efficient third dredge-up episode. In case of O-enrichment, O abundance does not trace the metallicities of objects and, therefore Ar or other elements, such as Cl, are better indicators of initial metallicities.

6. Results and discussion

From observations obtained with the GTC, VLT, and CFH telescopes, we have analysed the spectrophotometric data of 22 PNe in NGC 6822. This represents 84% of the total sample of 26 PN candidates known in this galaxy. We have confirmed the PN nature of 73% of the sample. Physical conditions and chemical abundances (in particular helium, nitrogen, oxygen, argon, and sulphur) were derived for 19 PNe. In addition, the chemical abundances of four H regions have been included for comparison: H 15 and H III observed by us and H V and H X from data by Peimbert et al. (2005). In the following we discuss the main results of our analysis.

A large number of Peimbert Type I PNe were found. (Following Hernández-Martínez et al. 2009, Peimbert Type I PNe were selected as those having N/O abundance ratio larger than 0.5.) These are PN 5, PN 8, PN 11, PN 14, PN 16, and

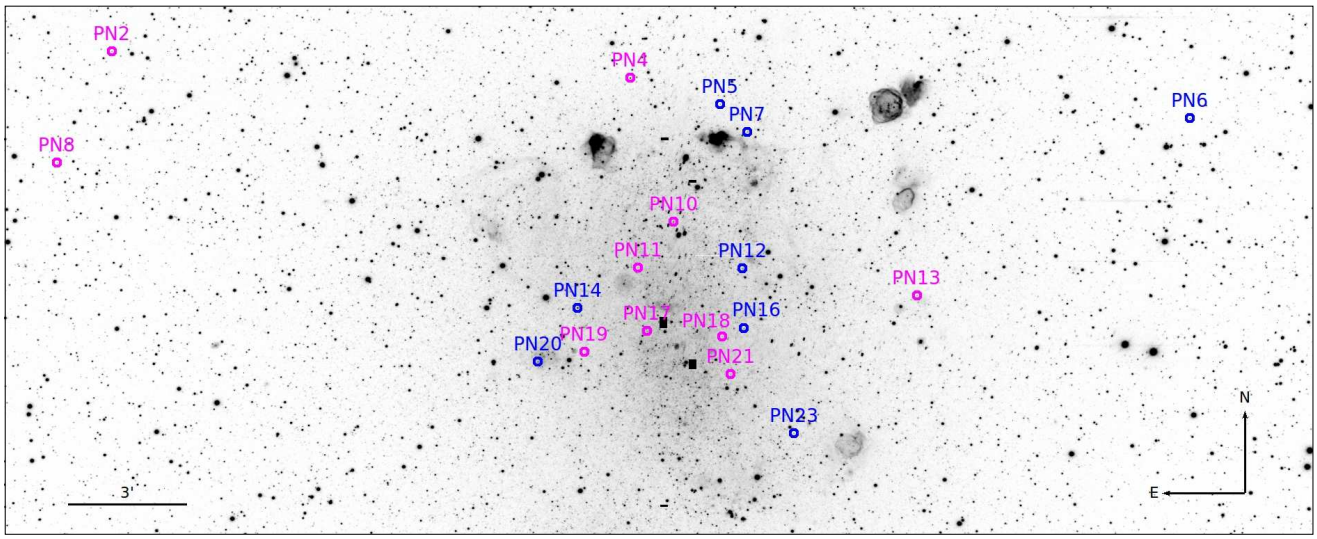

Fig. 12. Distribution of PNe in NGC 6822 in an Hα image. In pink the objects with low metallicity (12 + log (O/H) < 8 and 12 + log (Ar/H) < 5.7); in blue, the high-metallicity ones (12 + log (O/H) > 8 and 12 + log (Ar/H) > 5.7. PN 6, with 12 + log (Ar/H) of 5.71 is marginally a young object).

PN 18, representing over 31% of the analysed sample (very probably PN 25 is also a Type I PN; but it is not included here since we cannot calculate its chemical abundances, and it is potentially affected by atmospheric diffraction effects, see Sect. 2). This large number resembles the number of Type I PNe found in the galactic bulge, M 31 and the LMC (Stasińska et al. 1998). We recall that Type I PNe are He- and N-rich objects and they originated in stars that are more massive than in other PN types. Therefore it seems that we are detecting a large number of PNe produced by the more massive central stars, and the same is true for other galaxies. From the comparison of our N/O values and the predictions of stellar evolution models (Figs. 4 and 8), it is found that the initial masses of the central stars were lower than 4 $M_{\odot}$ and that Type I PNe had masses between 3 and 4 $M_{\odot}$.

Highly ionized PNe with a ionic fraction $He^{++}/He \geq 0.10$ are PN 4, PN 5, PN 8, PN 12, PN 14, PN 16, PN 23, PN 24, PN 13, PN 18, and PN 19, representing almost 60% of the sample. This high percentage of He^{++}/He implies the presence of a very hot central star. Models from the ample grid computed by Morisset et al. (2015) (Mexican Million Models data base, 3MdB) have been used to analyse this. We chose the 'Realistic' and matter-bounded PNe models (PNE-2014, Delgado-Inglada et al. 2014) that use a black body (BB) for the spectral energy distribution of the ionizing star. From this grid we have constructed Fig. 11, showing the behaviour of our objects in comparison with photoionization models, in an [O]λ5007/[O]λ7325 vs. He λ4686/Hβ diagram. The effective temperature for the models is shown in the colour bar. Our sample of PNe with $He^{++}/He \geq 0.10$ corresponds to objects with effective temperatures over 100 000 K. It is important to notice that we have a limited number of objects with [O]λ7325, but this is not a problem because in this figure we can clearly see that the ratio He λ4684/H$_{\beta}$ is the most important parameter for determining the effective temperature, which is almost independent of the [O]λ5007/[O]λ7325 ratio. The large number of highly ionized PNe in NGC 6822 seems unusual when compared to the PNe in our galaxy, but it is similar to what is found in the LMC (Stasińska et al. 1998). Type I PNe have been marked in green in this figure. It is evident that these PNe present

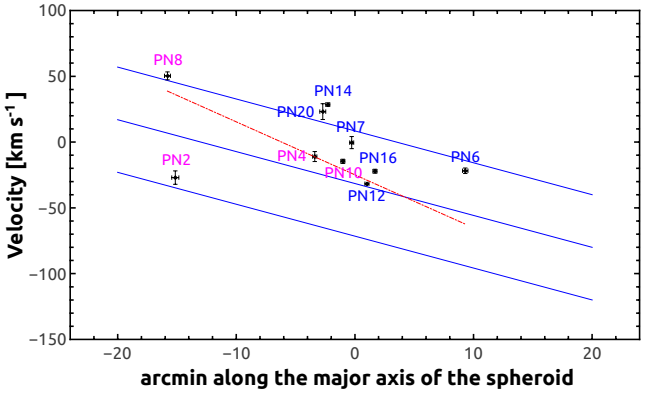

Fig. 13. Position-velocity of PNe in NGC 6822 with abundances determined, adapted from Flores-Durán et al. (2014). The position is projected on the long axis of the stellar spheroid. In pink the old objects (12 + log (Ar/H) ≤ 5.7); in blue the young objetcs.

the highest He λ4686/Hβ line intensity ratios and the highest stellar temperatures, which are in the range from 140 to 230 kK. If we compare such temperatures with the evolutionary tracks presented by Vassiliadis & Wood (1994) for the SMC metallicity (their Fig. 5), we conclude that the three hottest stars had initial masses higher than 2.5 $M_{\odot}$ (and would have present core masses higher than 0.69 $M_{\odot}$). This agrees with the initial masses derived for Type Is from the N/O ratio (Figs. 4 and 8).

Therefore our PN sample seems to have some biases: we find too many Type I PNe and very hot central stars (as compared to the galactic values). Our PN candidates were selected from a sample of [O]λ5007- and Hα- emitting objects (Hernández-Martínez & Peña 2009). Actually to be certain they are PN and to eliminate compact H regions, Ciardullo et al. (2002) suggested selecting PN candidates because they have [O] λ5007/Hα ratios over 1.6. In the sample by Hernández-Martínez & Peña (2009), there are a few candidates with [O] λ5007/Hα lower than 1.6, since other criteria

were used, such as the non-detection of the central star. Either way, possible low-ionization PNe with faint [O] λ5007 and therefore low stellar effective temperature (T_* lower than 40 kK) were ignored.

As already reported for the 11 PNe studied by Hernández-Martínez et al. (2009), here we again find an old population of PNe with 12 + log (O/H) < 8 and 12 + log (Ar/H) < 5.7 (see Figs. 3 and 6). These old objects are PN 2, PN 4, PN 8, PN 10, PN 11, PN 13, PN 18, PN 19, PN 21, and PN 17, representing half of the total sample. Seven PNe show 12 + log (O/H) greater than 8.0 and 12 + log (Ar/H) over 5.7, and these young PNe are PN 5, PN 6, PN 7, PN 12, PN 14, PN 16, PN 23, and PN 20. (It is worth noticing that PN 6 is marginally young as its 12 + log (Ar/H) is 5.71.) In Fig. 12 we show the spatial distribution of the two populations in the galaxy. It is observed than young PNe tend to lie in the central zone well inside the optical bar, while the old objects are more widely distributed. The same is true if we plot the PNe velocities (relative to the system) against the distance along the long axis of the stellar spheroid, presented in Fig. 13 (adapted from Flores-Durán et al. 2014); although no preference in velocity is found, the old population is distributed at both sides of the centre, while the young PNe are nearer the central region in the optical bar. We notice that PN 6 could be marginally an old object.

7. Summary

The PN sample analysed here (representing ~84% of the total sample detected in this galaxy) is biased towards nebulae with very hot central stars. Such a bias probably occurs also in the PN samples of many other external galaxies due to the way PN candidates are selected.

From comparison with stellar evolution models by Karakas (2010) and Fishlock et al. (2014) of the N/O abundance ratio, our PNe should have had initial masses lower than 4 $M_\odot$, although if the comparison is made with Ne/H vs. O/H abundances, the initial masses should have been lower than 2 $M_\odot$. It appears that the models of stars of 2−3 $M_\odot$ by Karakas (2010) and Fishlock et al. (2014) are producing too much ^{22}Ne in the stellar surface at the end of the AGB. On the other hand, the comparison with ATON models by Ventura et al. (2013, 2014a,b) – which differ from the previous models in the treatment of convection and on the assumptions concerning the overshoot of the convective core during the core H-burning phase – leads to reasonable agreement between the observed and predicted ratios of N/O and Ne/H if more massive stars are about 4 $M_\odot$. So far, none of the models reproduce the large He abundances found in many PNe of NGC 6822.

The Type I PNe were produced by stars of any metallicity (not necessarily the richer ones), and their initial masses were between 3 and 4 $M_\odot$. These objects show the highest effective temperatures.

The PNe in NGC 6822 span in metallicity from very poor objects (12 + log (Ar/H) ≤ 5.7) to nebulae showing the same metallicity as the H regions (12 + log (Ar/H) ~ 5.8). The poorer objects are more widely spread in the galaxy, while the young ones lie in or very near the optical bar.

Acknowledgements. This work is based on observations with the Gran Telescopio Canarias (GTC), installed in the Spanish Observatorio del Roque de los Muchachos of the Instituto de Astrofísica de Canarias on the island of La Palma. This work has been funded by the Spanish Ministry of Economy and Competitiveness (MINECO) under the grant AYA2011-22614 and also received partial support from the DGAPA-UNAM, Mexico under grant PAPIIT IN109614. We thank the referee, G. Stasińska, for her valuable comments that helped to improve the quality of the paper. JGR acknowledges support from the Severo Ochoa excellence programme (SEV-2011-0187) postdoctoral fellowship. We are very grateful to Dr. P. Ventura for providing the tables with the surface abundances of his AGB models, and to Dr. C. Morisset for his invaluable help and comments related to the 3Mdb. We also are grateful to A. Karakas from providing the detailed numbers of the models by Fishlock et al. (2014). We acknowledge fruitful discussions with D. A. García-Hernández, A. Karakas, and M. Lugaro.

References

Allen, C., Carigi, L., & Peimbert, M. 1998, ApJ, 494, 247
Battinelli, P., Demers, S., & Kunkel, W. E. 2006, A&A, 451, 905
Bhatia, A. K., & Doschek, G. A. 1993, At. Data Nucl. Data Tables, 55, 315
Blöcker, T. 1995, A&A, 297, 797
Butler, K., & Zeippen, C. J. 1989, A&A, 208, 337
Canuto, V. M., & Mazzitelli, I. 1991, ApJ, 370, 295
Carigi, L., Colin, P., & Peimbert, M. 2006, ApJ, 644, 924
Ciardullo, R., Feldmeier, J. J., Jacoby, G. H., et al. 2002, ApJ, 577, 31
Corradi, R. L. M., García-Rojas, J., Jones, D., & Rodríguez-Gil, P. 2015a, ApJ, 803, 99
Corradi, R. L. M., Kwitter, K. B., Balick, B., Henry, R. B. C, & Hensley, K. 2015b, ApJ, 807, 181
Dance, M., Palay, E., Nahar, S. N., & Pradhan, A. K. 2013, MNRAS, 435, 1576
de Blok, W. J. G., & Walter, F. 2000, ApJ, 537, L95
de Blok, W. J. G., & Walter, F. 2006, AJ, 131, 343
Delgado-Inglada, G., Morisset, C., & Stasińska, G. 2014, MNRAS, 440, 536
Delgado-Inglada, G., Rodríguez, M., Peimbert, M., Stasińska, G., & Morisset, C. 2015, MNRAS, 449, 1797
Dell'Agli, F., Ventura, P., Schneider, R., et al. 2015, MNRAS, 447, 2992
Demers, S., Battinelli, P., & Kunkel, W. E. 2006, ApJ, 636, L85
Esteban, C., Bresolin, F., Peimbert, M., et al. 2009, ApJ, 700, 654
Fishlock, C. K., Karakas, A. I., Lugaro, M., & Yong, D. 2014, ApJ, 797, 44
Flores-Durán, S., Peña, M., Hernández-Martínez, L. et al. 2014, A&A, 568, A82
Froese Fischer, C., & Tachiev, G. 2004, At. Data Nucl. Data Tables, 87, 1
Galavís, M. E., Mendoza, C., & Zeippen, C. J. 1995, A&AS, 111, 347
Galavís, M. E., Mendoza, C., & Zeippen, C. J. 1997, A&AS, 123, 159
García-Hernández, D. A., & Górny, S. K. 2014, A&A, 567, A12
García–Rojas, J., & Esteban, C. 2007, ApJ, 670, 457
Gieren, W., Pietrzyński, G., Nalewajko, K., et al. 2006, ApJ, 647, 1056
Hernández-Martínez, L., & Peña, M. 2009, A&A, 495, 447
Hernández-Martínez, L., Peña, M., Carigi, L., & García-Rojas, J. 2009, A&A, 505, 102
Hernández-Martínez , L., Carigi, L., Peña, M., & Peimbert, M. 2011, A&A, 535, A118
Henry, R. B. C. 1989, MNRAS, 241, 453
Henry, R. B. C., Kwitter, K. B., & Balick, B. 2004, AJ, 127, 2284
Hwang, N., Soo Park, H., Gyong Lee, M., et al. 2014, ApJ, 783, 49
Izotov, Y. I., Stasińska, G., Meynet, G., Guseva, N. G., & Thuan, T. X. 2006, A&A, 448, 955
Karakas, A. I. 2010, MNRAS, 403, 1413
Karakas, A. I., & Lattanzio, J. C. 2003, PASA, 20, 393
Karakas, A. I., van Raai, M. A., Lugaro, M., Sterling, N. C., & Dinerstein, H. L. 2009, ApJ, 690, 1130
Kaufman, V., & Sugar, J. 1986, J. Phys. Chem. Ref. Data, 15, 343
Kingsburgh R. L., & Barlow M. J. 1994, MNRAS, 271, 257
Kisielius, R., Storey, P. J., Ferland, G. J., & Keenan, F. P. 2009, MNRAS, 397, 903
LaJohn, L., & Luke, T. M. 1993, Phys. Scr., 47, 542
Leisy, P., & Dennefeld, M. 2006, A&A, 456, 451
Letarte, B., Demers, S., Batinelli, P., & Kunkel, W. E. 2002, AJ, 123, 832
Liu, X.-W. 2012, in Planetary Nebulae: An Eye to the Future, eds. A. Manchado, L. Stanghellini, & D. Schönberner, IAU Symp. 283, 131
Luridiana, V., Morisset, C., & Shaw, R. A. 2015, A&A, 573, A42
Magrini, L., Stanguellini, L., & Villaver, E. 2009, ApJ, 696, 729
Marigo, P. 2001, A&A, 370, 194
McLaughlin, B. M., & Bell, K. L. 2000, J. Phys. B, 33, 597
McNabb, I. A., Fang, X., Liu, X.-W., Bastin, R. J., & Storey, P. J. 2013, MNRAS, 428, 3443
Mendoza, C. 1983, IAU Symp., 103, 143
Mendoza, C., & Zeippen, C. J. 1982, MNRAS, 198, 127
Moe, M., & De Marco, O. 2006, ApJ, 650, 916
Morisset, C., Delgado-Inglada, G., & Flores-Fajardo, N. 2015, Rev. Mex. Astron. Astrofis., 51, 1093

Peimbert, A., Peimbert, M., & Ruiz, M. T. 2005, ApJ, 634, 1056
Peña, M., Stasińska, G., & Richer, M. G. 2007, A&A, 476, 745
Peña-Guerrero, M. A., Peimbert, A., & Peimbert, M. 2012, ApJ, 756, L14
Pignatari, M., Herwig, F., Hirschi, R., et al. 2013, ApJS, submitted [arXiv:1307.6961]
Podobedova, L. I., Kelleher, D. E., & Wiese, W. L. 2009, J. Phys. Chem. Ref. Data, 38, 171
Ramsbottom, C. A., & Bell, K. L. 1997, At. Data Nucl. Data Tables, 66, 1
Richer, M. G., & McCall, M. 2007, ApJ, 658, 328
Rodríguez-González, A., Hernández-Martínez, L., Esquivel, A., et al. 2015, A&A, 575, A19
Stasińska, G., Richer, M. G., & McCall, M. 1998, A&A, 336, 667
Stasińska, G., Peña, M., Bresolin, F., & Tsamis, Y. G. 2013, A&A, 552, A12
Storey, P. J., & Hummer, D. G. 1995, MNRAS, 272, 41
Storey P. J., & Zeippen C. J., 2000, MNRAS, 312, 813
Storey, P. J., Sochi, T., & Badnell, N. R. 2014, A&A, 441, 3028
Tayal, S. S. 2011, ApJS, 195, 12
Tayal, S. S., & Gupta, G. P. 1999, ApJ, 526, 544
Tayal, S. S., & Zatsarinny, O. 2010, ApJS, 188, 32
Vassiliadis, E., & Wood, P. R. 1994, ApJS, 92, 125
Ventura, P., Di Criscienzo, M., Carini, R., & D'Antona, F. 2013, MNRAS, 431, 3642
Ventura, P., Di Criscienzo, M., D'Antona, F., et al. 2014a, MNRAS, 437, 3274
Ventura, P., Dell'Agli, F., Schneider, R., et al. 2014b, MNRAS, 439, 977
Ventura, P., Stanghellini, L., Dell'Agli, F., García-Hernández, D. A., & Criscienzo, M. 2015, MNRAS, 452, 3679
Weldrake, D. T. F., de Blok, W. J. G., & Walter, F. 2003, MNRAS, 340, 12
Wyder, T. K. 2001, AJ, 122, 2490
Wyder, T. K. 2003, AJ, 125, 3097

Appendix A: Additional figures and tables

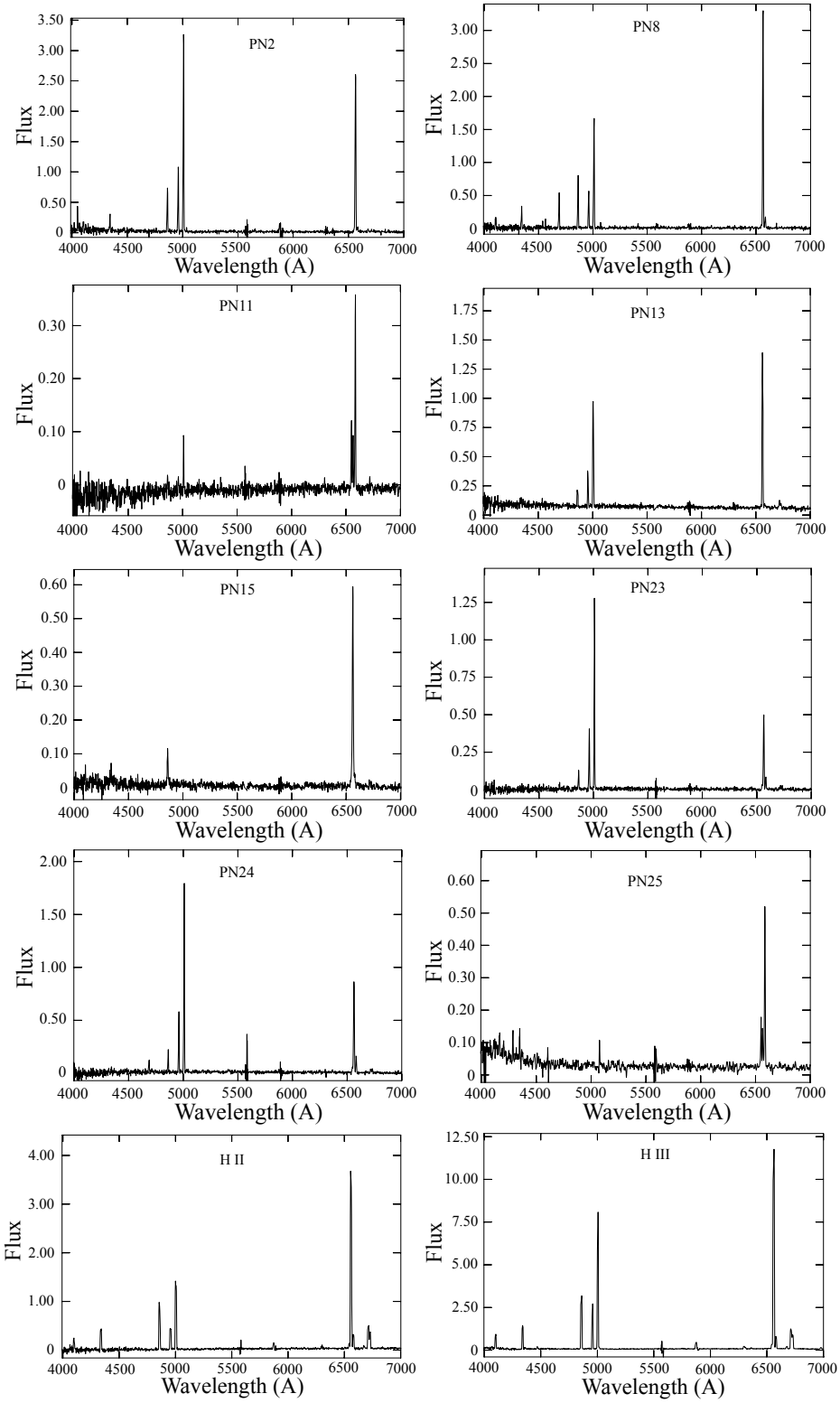

Fig. A.1. Calibrated spectra of PNe and H regions observed with GTC. Flux in units of 10^{-16} erg cm^{-2} s^{-1} A^{-1}.

Table A.1. Dereddened line intensities from GTC observations.

Object		PN 2		PN 8		PN 9		PN 11		PN 13		PN 15	
λ	ion	I/I(Hβ)	err	I/I(Hβ)	err	I/I(Hβ)	err	I/I(Hβ)	err	I/I(Hβ)	err	I/I(Hβ)	err
3727	[O]	<2.40E-01	–	–	–	–	–	–	–	noisy	–	–	–
3869	[Ne]	3.46E-01	39	<1.00E-01	–	noisy	–	noisy	–	–	–	–	–
3889	H8+He	–	–	2.16E-01	18	–	–	noisy	–	noisy	–	–	–
3970	H7+[Ne]	2.37E-01	30	1.76E-01	20	–	–	noisy	–	noisy	–	–	–
4102	Hδ	3.08E-01	30	2.42E-01	10	–	–	noisy	–	2.35E-01	47	2.27E-01	30
4340	Hγ	4.65E-01	10	4.22E-01	8	4.43E-01	30	noisy	–	4.82E-01	29	4.69E-01	11
4363	[O]	1.30E-01	40	7.28E-02	41	–	–	noisy	–	2.44E-01	30	–	–
4471	He	1.77E-01	40	<3.00E-02	–	–	–	noisy	–	–	–	–	–
4686	He	<6.00E-02	–	7.23E-01	5	–	–	noisy	–	<1.70E-01	–	–	–
4861	Hβ	1.00E+00	3	1.00E+00	5	1.00E+00	5	1.00E+00	20	1.00E+00	10	1.00E+00	3
4959	[O]	1.43E+00	2	7.09E-01	5	–	–	9.92E-01	20	2.53E+00	8	–	–
5007	[O]	4.49E+00	2	2.07E+00	5	2.50E-01	40	3.09E+00	3	7.25E+00	5	<1.00E-02	–
5412	He	–	–	5.25E-02	11	–	–	–	–	–	–	–	–
5755	[N]	<2.00E-02		<1.90E-02	–	–	–	4.00E-01	40	–	–	–	–
5876	He	1.29E-01	15	6.41E-02	25	–	–	noisy	–	1.47E-01	14	–	–
6548	[N]	3.00E-02	33	4.50E-02	22	–	–	3.06E+00	6	–	–	4.00E-02	50
6563	Hα	2.86E+00	2	2.85E+00	3	2.86E+00	1	2.86E+00	10	2.86E+00	5	2.86E+00	3
6583	[N]	7.73E-02	15	1.43E-01	6	<5.00E-02	–	1.06E+01	1	<5.20E-02	–	1.23E-01	15
6678	He	5.05E-02	20	2.70E-02	30	–	–	–	–	–	–	–	–
6716	[S]	<1.50E-02	–	6.60E-03	30	<4.00E-02	–	4.52E-01	24	5.23E-02	19	4.83E-02	19
6731	[S]	1.58E-02	37	1.21E-02	49	<4.00E-02	–	4.38E-01	25	1.77E-02	22	4.28E-02	21
7006	[Ar]	–	–	2.34E-02	38	–	–	–	–	–	–	–	–
7065	He	8.41E-02	20	1.66E-02	54	–	–	–	–	7.53E-02	20	–	–
7135	[Ar]	2.34E-02	21	2.49E-02	30	–	–	<1.90E-01	–	<6.60E-02	–	–	–
7325	[O]	6.07E-02	20	2.13E-02	42	1.00E-01	50	<3.00E-01	–	5.99E-02	20	–	–
F(Hβ)[b]		5.63E-16		5.94E-16		2.07E-16		2.50E-17		1.15E-16		1.12E-16	
c(Hβ)		0.58		0.75		1.45		0.126		1.88		1.17	

Notes. Errors in % . [(a)] observed flux in erg cm^{-2} s^{-1}.

Table A.1. continued.

Object		PN 22		PN 23		PN 24		PN 25[c]		H II		H III	
λ	ion	I/I(Hβ)	err	I/I(Hβ)	err	I/I(Hβ)	err	I/I(Hα)	err	I I/I(Hβ)	err	I/I(Hβ)	err
3727	[O]	–	–	–	–	–	–	–	–	5.01E+00	10	3.76E+00	7
3869	[Ne]	–	–	–	–	–	–	–	–	–	–	1.29E-01	12
3889	H8+He	–	–	–	–	–	–	–	–	–	–	1.56E-01	12
3970	H7+[Ne]	–	–	–	–	–	–	–	–	–	–	1.88E-01	10
4102	Hδ	–	–	–	–	–	–	–	–	2.45E-01	20	2.97E-01	10
4340	Hγ	9.80E-01	:	2.77E-01	:	4.60E-01	20	–	–	4.93E-01	10	4.83E-01	10
4363	[O]	–	–	<2.00E-01	–	1.80E-01	39	–	–	<3.3E-02		2.93E-02	20
4471	He	–	–	–	–	<1.00E-01	–	–	–	–	–	5.61E-02	10
4686	He	–	–	2.93E-01	27	7.04E-01	15	–	–	–	–	–	–
4861	Hβ	1.00E+00	10	1.00E+00	10	1.00E+00	5	<2.00E-01	–	1.00E+00	–	1.00E+00	5
4959	[O]	–	–	3.43E+00	5	2.51E+00	4	–	–	4.83E-01	7	7.58E-01	5
5007	[O]	<9.00E-02	–	1.07E+01	4	7.77E+00	3	<2.00E-01	–	1.38E+00	3	2.28E+00	3
5412	He	–	–	–	–	5.00E-02	50	–	–	–	–	–	–
5755	[N]	–	–	–	–	2.00E-02	50	<1.00E-01	–	–	–	–	–
5876	He	–	–	9.87E-02	30	<1.00E-01	–	<1.00E-01	–	1.09E-01	10	1.03E-01	8
6548	[N]	–	–	1.50E-01	33	1.80E-01	28	1.38E+00	10	7.39E-02	12	3.08E-02	12
6563	Hα	2.86E+00	5	2.86E+00	5	2.87E+00	3	1.00E+00	10	2.87E-01	3	2.89E+00	3
6583	[N]	3.10E-01	23	5.32E-01	11	5.37E-01	9	4.50E+00	3	2.24E-01	10	1.46E-01	8
6678	He	–	–	–	–	–	–	–	–	4.19E-2	20	3.06E-02	12
6716	[S]	5.80E-01	21	1.67E-01	20	1.06E-01	19	1.10E-01	20	3.58E-01	10	2.79E-01	8
6731	[S]	5.10E-01	20	1.27E-01	24	8.69E-02	23	8.10E-02	30	2.42E-01	12	2.05E-01	8
7006	[Ar]	–	–	–	–	–	–	–	–	–	–	–	–
7065	He	–	–	–	–	–	–	4.55E-02	44	9.75E-02	19	8.10E-02	10
7135	[Ar]	–	–	8.82E-02	29	9.34E-02	11	–	–	7.92E-02	20	8.19E-02	10
7325	[O]	4.00E-01	:	9.48E-02	32	–	–	–	–	1.36E-01	25	9.11E-02	10
F(Hβ)[a]		8.39E-17		8.12E-17		1.45E-16		9.00E-17		1.14E-15[c]		3.85E-15[c]	
c(Hβ)		0.61		0.79		0.89		>0.8		0.39		0.44	

Notes. Errors in %. Colons indicate errors greater than 50%. [(a)] Observed Hβ flux in erg cm^{-2} s^{-1}. [(b)] For PN 25 the reported fluxes are relative to Hα. F(Hα) is given. [(c)] Extended H region. Partial Hβ flux in a slit of 3×1.5 arcsec^2.

Table A.2. Ionic abundances[a] in NGC 6822 from VLT (11 PNe and one H II region) and CFH (PN 17 and PN 20) data and for H V and H X[b].

Object	PN 4	PN 5	PN 6	PN 7	PN 10	PN 12	PN 14	PN 16
T_e([O III]) (K)	17 950 ± 1250	<24 600	12 500 ± 750	13 270 ± 2400	18 200 ± 1150	12 900 ± 650	17 900 ± 1000	14 200 ± 700
T_e([N II]) (K)	14 200 ± 2650	15 350 ± 1500	11 600 ± 3100	–	–	–	20 500 ± 2500	–
n_e([S II]) (cm^{-3})	2450^{+1800}_{-1000}	700^{+1100}_{-450}	3700^{+5200}_{-2150}	2300^{+7000}_{-1700}	1000 (adopted)	2000 (adopted)	4500^{+8100}_{-2900}	900^{+1650}_{-600}
n_e([Ar IV]) (cm^{-3})	1900:	–	–	–	–	1700^{+4600}_{-1250}	11 500:	4500^{+7500}_{-2800}
Ion				12 + log (X^{+i}/H^+)				
He^+	10.81 ± 0.04	10.80 ± 0.16	10.98 ± 0.04	11.09 ± 0.10	11.15 ± 0.04	10.91 ± 0.06	10.72 ± 0.07	11.03 ± 0.05
He^{++}	10.29 ± 0.04	10.66 ± 0.05	$8.93^{+0.16}_{-0.25}$	<9.93	<9.36	10.30 ± 0.06	10.72 ± 0.02	10.42 ± 0.05
N^+	$6.52^{+0.18}_{-0.15}$	7.40 ± 0.09	$6.39^{+0.32}_{-0.25}$	$6.48^{+0.22}_{-0.13}$	5.46 ± 0.12	5.81 ± 0.09	$7.31^{+0.07}_{-0.04}$	6.21 ± 0.05
O^+	$6.85^{+0.27}_{-0.24}$	7.05 ± 0.24	7.15:	7.87:	6.74 ± 0.13	$6.53^{+0.24}_{-0.19}$	$6.94^{+0.11}_{-0.08}$	6.24 ± 0.13
O^{++}	7.68 ± 0.07	7.70 ± 0.11	8.11 ± 0.07	$8.01^{+0.23}_{-0.17}$	7.47 ± 0.06	8.20 ± 0.08	7.87 ± 0.05	8.15 ± 0.05
Ne^{++}	6.93 ± 0.08	–	7.34 ± 0.08	–	6.65 ± 0.08	7.36 ± 0.09	–	7.41 ± 0.07
Ne^{+4}	6.52 ± 0.16	–	–	–	–	–	–	–
S^+	$5.20^{+0.19}_{-0.16}$	5.79 ± 0.10	5.16:	$4.85^{+0.28}_{-0.24}$	–	$4.38^{+0.26}_{-0.23}$	$4.86^{+0.25}_{-0.16}$	$4.67^{+0.11}_{-0.09}$
S^{++}	5.89 ± 0.10	$6.21^{+0.20}_{-0.25}$	$5.91^{+0.16}_{-0.21}$	5.88 ± 0.29	–	6.15 ± 0.12	$5.56^{+0.16}_{-0.25}$	$5.86^{+0.12}_{-0.15}$
Ar^{++}	5.31 ± 0.07	5.64 ± 0.11	5.55 ± 0.06	5.79 ± 0.19	$4.88^{+0.12}_{-0.15}$	5.62 ± 0.09	5.39 ± 0.09	5.41 ± 0.08
Ar^{+3}	5.22 ± 0.09	–	5.23 ± 0.17	–	–	5.63 ± 0.11	5.32 ± 0.09	5.67 ± 0.08
Ar^{+4}	$4.50^{+0.13}_{-0.17}$	–	–	–	–	–	$5.13^{+0.10}_{-0.13}$	–
Object	PN 18	PN 19	PN 21	H II 15	PN 17	PN 20	H V	H X
T_e([O III]) (K)	18 950 ± 1900	22 050 ± 3300	16 200 ± 1200	12 150 ± 200	19 300 ± 3000	15 500 ± 4000	11 800 ± 250	11 950 ± 470
T_e([O II]) (K)	–	–	–	–	–	–	15 300 ± 900	14 300 ± 1100
T_e([N II]) (K)	–	–	–	12 000 ± 1800	–	–	15 800 ± 2850	–
n_e([S II]) (cm^{-3})	1150^{+3400}_{-850}	<100	180^{+470}_{-150}	170^{+240}_{-100}	180^{+370}_{-120}	2000 (adopted)	80^{+110}_{-50}	<20
n_e([O II]) (cm^{-3})	–	–	–	–	–	–	70^{+70}_{-40}	50^{+70}_{-30}
n_e([Cl III]) (cm^{-3})	–	–	–	300^{+800}_{-210}	–	–	600^{+1500}_{-430}	<20
n_e([Ar IV]) (cm^{-3})	–	–	–	–	–	–	–	–
He^+	<10.76	$11.09^{+0.15}_{-0.26}$	$11.11^{+0.06}_{-0.09}$	10.90 ± 0.02	$10.98^{+0.11}_{-0.16}$	$10.91^{+0.05}_{-0.07}$	10.92 ± 0.02	10.90 ± 0.04
He^{++}	10.82 ± 0.02	10.18 ± 0.07	$9.37^{+0.16}_{-0.26}$	–	10.54 ± 0.07	$9.97^{+0.17}_{-0.30}$	–	–
N^+	6.40 ± 0.09	$6.15^{+0.14}_{-0.10}$	$5.88^{+0.08}_{-0.10}$	$6.08^{+0.16}_{-0.14}$	6.06 ± 0.15	$5.38^{+0.17}_{-0.29}$	5.57 ± 0.15	5.80 ± 0.08
O^+	$5.72^{+0.18}_{-0.14}$	$7.15^{+0.21}_{-0.24}$	6.50 ± 0.16	$7.58^{+0.27}_{-0.21}$	$7.28^{+0.18}_{-0.19}$	$7.06^{+0.12}_{-0.17}$	$6.87^{+0.25}_{-0.20}$	7.14 ± 0.13
O^{++}	$7.23^{+0.10}_{-0.08}$	$7.19^{+0.17}_{-0.09}$	7.74 ± 0.08	7.86 ± 0.03	$7.66^{+0.18}_{-0.15}$	7.93 ± 0.02	8.04 ± 0.03	7.94 ± 0.06
Ne^{++}	$6.65^{+0.12}_{-0.14}$	–	$6.96^{+0.13}_{-0.10}$	7.12 ± 0.03	$6.99^{+0.26}_{-0.21}$	$7.40^{+0.10}_{-0.13}$	7.30 ± 0.04	7.18 ± 0.07
S^+	$5.09^{+0.21}_{-0.17}$	5.76:	5.06 ± 0.09	$5.45^{+0.15}_{-0.13}$	$5.78^{+0.13}_{-0.11}$	$4.83^{+0.08}_{-0.10}$	$5.09^{+0.15}_{-0.12}$	$5.29^{+0.11}_{-0.08}$
S^{++}	–	5.82:	<3.61	6.30 ± 0.06	–	–	6.34 ± 0.05	6.35 ± 0.10
Cl^{++}	–	–	–	$4.40^{+0.07}_{-0.09}$	–	–	4.43 ± 0.06	$4.38^{+0.11}_{-0.15}$
Ar^{++}	–	$5.30^{+0.17}_{-0.15}$	5.40 ± 0.11	5.76 ± 0.04	–	5.63 ± 0.06	5.76 ± 0.03	5.75 ± 0.05
Ar^{+3}	–	–	–	–	–	–	4.80 ± 0.10	–

Notes. Abundances in 12 + log (X^{+i}/H^+). H V and H X line intensities were adopted from Peimbert et al. (2005). Colons indicate errors larger than a factor of two.

Table A.3. Total abundances and $L(H\beta)$ for PNe from VLT and CFH data and for H V and H X.

Elem/object	PN 4	PN 5	PN 6	PN 7	PN 10	PN 12	PN 14	PN 16
He	10.92 ± 0.04	11.03 ± 0.10	10.99 ± 0.04	11.09 ± 0.08	11.16 ± 0.03	11.01 ± 0.05	11.02 ± 0.04	11.13 ± 0.04
N	7.43 ± 0.09	$8.21^{+0.17}_{-0.12}$	7.55 ± 0.18	$6.89^{+0.18}_{-0.16}$	$6.37^{+0.13}_{-0.15}$	7.50 ± 0.17	8.39 ± 0.12	8.13 ± 0.12
O	7.81 ± 0.10	7.94 ± 0.13	$8.16^{+0.13}_{-0.08}$	$8.27^{+0.23}_{-0.21}$	7.55 ± 0.07	8.26 ± 0.08	8.12 ± 0.04	8.21 ± 0.05
Ne	7.00 ± 0.08	–	7.65:	–	$6.75^{+0.20}_{-0.11}$	7.42 ± 0.08	–	7.47 ± 0.07
S	6.18 ± 0.10	$6.59^{+0.16}_{-0.19}$	6.17 ± 0.17	$5.92^{+0.30}_{-0.25}$	–	6.57 ± 0.12	$6.01^{+0.17}_{-0.22}$	6.37 ± 0.14
Ar	5.52 ± 0.08	5.90 ± 0.12	5.71 ± 0.09	5.84 ± 0.16	$5.01^{+0.11}_{-0.16}$	5.94 ± 0.10	5.74 ± 0.10	5.70 ± 0.08
$L(H\beta)/L_\odot$	33.92	3.27	20.16	7.32	26.95	3.18	15.98	5.73
Elem/object	PN 18	PN 19	PN 21	H II 15	PN 17	PN 20	H V	H X
He	11.09 ± 0.09	$11.14^{+0.14}_{-0.21}$	$11.11^{+0.05}_{-0.09}$	10.95 ± 0.03	$11.12^{+0.09}_{-0.11}$	$10.96^{+0.06}_{-0.07}$	10.94 ± 0.02	10.95 ± 0.03
N	$8.04^{+0.14}_{-0.12}$	$6.50^{+0.33}_{-0.11}$	$7.26^{+0.17}_{-0.13}$	6.54 ± 0.04	$6.62^{+0.15}_{-0.14}$	$6.33^{+0.21}_{-0.33}$	6.72 ± 0.05	6.63 ± 0.06
O	$7.48^{+0.16}_{-0.11}$	$7.50^{+0.17}_{-0.14}$	7.77 ± 0.08	$8.05^{+0.11}_{-0.07}$	7.89 ± 0.16	8.01 ± 0.03	8.07 ± 0.03	8.00 ± 0.05
Ne	$6.88^{+0.19}_{-0.16}$	–	$7.00^{+0.21}_{-0.16}$	7.18 ± 0.04	$7.07^{+0.24}_{-0.21}$	$7.42^{+0.11}_{-0.12}$	7.31 ± 0.04	7.21 ± 0.07
S	6.88 ± 0.13	6.10:	$6.63^{+0.17}_{-0.15}$	6.39 ± 0.05	$6.56^{+0.12}_{-0.11}$	$6.04^{+0.17}_{-0.16}$	6.63 ± 0.07	6.51 ± 0.10
Cl	–	–	–	4.50 ± 0.09	–	–	$4.86^{+0.10}_{-0.08}$	4.60 ± 0.14
Ar	–	5.34 ± 0.19	$5.60^{+0.09}_{-0.12}$	5.79 ± 0.04	–	5.80 ± 0.06	5.81 ± 0.03	5.84 ± 0.06
$L(H\beta)/L_\odot$	0.57	1.23	0.76	308.67	–	–	–	–

Notes. Abundances in 12 + log (X/H). Colons indicate errors larger than a factor of two.

4

Kinematic and chemical study of planetary nebulae in NGC 3109

4.1. Resumen.

Se obtuvieron datos de alta resolución con el espectrógrafo Magellan Inamori Kyocera Echelle (MIKE) de nueve NPs y una región H II. Con el Manchester Echelle Spectrometer (MES) se obtuvieron datos de tres NPs, seis regiones H II compactas y nueve nudos de regiones H II extendidas. Al igual que para NGC 6822, se revisó el SPM Kinematic Catalogue: Extragalactic Planetary Nebulae (SPM KINCAT) y se encontraron datos de una NP. En total se tienen datos de nueve de las veinte NPs detectadas en esta galaxia y varias regiones H II.

La velocidades radiales medidas de los espectros calibrados tienen una precisión mejor que 7.8 km s^{-1}. De la literatura se tomaron datos de estrellas supergigantes azules Evans et al. (2007) para incluirlas en el análisis. Con estos datos se pudo comparar las velocidades radiales heliocéntricas con las velocidades del disco de H I en la misma posición proyectada. Del análisis de las velocidades radiales en NGC 3109 se encontró que las regiones H II muestran el mismo comportamiento cinemático que el disco de H I en la misma posición proyectada con una dispersión de velocidades baja. Las NPs y las estrellas supergigantes azules rotan en la misma dirección que el disco de H I pero estos objetos presentan una dispersión de velocidades alta. Esta dispersión puede deberse al hecho de que estos objetos pertenecen a una población diferente que se localiza en la barra central reportada para esta galaxia.

Para el análisis químico de las NPs, fue posible determinar las condiciones físicas de cuatro NPs utilizando los de alta resolución obtenidos con MIKE. Para tres de éstas se determinaron las abundancia de algunos elementos químicos. Con el propósito de ampliar los datos de las NPs y compararlas con los modelos de evolución estelar se tomaron datos de la literatura Peña et al. (2007), donde se mostró que todas las NPs son más abundantes en O que las regiones H II por 0.39 dex. Se re-calcularon las abundancias químicas de O, N, Ne, Ar y S utilizando los factores de corrección por ionización (ICF, por sus siglas en ingles) de Delgado-Inglada et al. (2014). Las diferencias encontradas entre la literatura y este trabajo para el O/H son menores que 0.05 dex, para las abundancias de N/H las diferencias son menores que 0.1 dex, en el caso del Ne/H las diferencias son menores que 0.08 dex. En el caso de la abundancia de Ar/H encontramos diferencias más grandes de

hasta 0.3 dex y para la abundancia de S/H las diferencias fueron de hasta 0.35 dex. Con esto confirmamos que las abundancia de las NPs de NGC 3109 muestran enriquecimiento de O.

Se encontró que las NPs están enriquecidas también en Ne. La abundancia promedio de O en regiones H II es $12 + \log \mathrm{O/H} = 7.74 \pm 0.09$ y las NPs presentan una abundancia de O mayor por 0.43 dex en promedio. La abundancia de Ne es cerca de tres veces mayor en NPs que en regiones H II. Este es un resultado muy importante que apoya a los modelos que predicen que para estrellas de muy baja metalicidad y con masas iniciales entre 1.5 y 4 $M_{\odot}$, el Ne es enriquecidos por sus progenitoras (Karakas & Lattanzio, 2003). Las abundancias químicas de nuestras NPs se reproducen mejor por modelos de evolución estelar de Ventura et al. (2013, 2014) para una metalicidad de $Z = 0.001$, que es similar a la metalicidad de las regiones H II. La abundancia en regiones H II no muestra un gradiente de metalicidad en esta galaxia. También se discutió si existe una conexión entre la cinemática y la química de NGC 3109. Las poblacíones jóvenes y de edad intermedia-vieja muestran pequeñas diferencias en su cineámtica y presentan diferentes composiciones químicas, sin embargo no hay gradientes químicos. Por lo que no se encuentra una relación evidente entre la cinemática y la química.

A&A 601, A147 (2017)
DOI: 10.1051/0004-6361/201629040

Astronomy & Astrophysics

Kinematic and chemical study of planetary nebulae and H II regions in NGC 3109⋆,⋆⋆

S. N. Flores-Durán[1], M. Peña[1], and M. T. Ruiz[2]

[1] Instituto de Astronomía, Universidad Nacional Autónoma de México, Apdo. Postal 70264, 04510 Ciudad de México, Mexico
e-mail: sflores,miriam@astro.unam.mx
[2] Depto. de Astronomía, Universidad de Chile, Casilla 36D, Las Condes, Santiago, Chile
e-mail: mtruiz@das.uchile.cl

Received 1 June 2016 / Accepted 21 February 2017

ABSTRACT

Aims. We present high-resolution spectroscopy of a number of planetary nebulae (PNe) and H II regions distributed along the dwarf irregular galaxy NGC 3109 and compare their kinematical behavior with that of H I data. We aim to determine if there is a kinematical connection among these objects. We also aim to determine the chemical composition of some PNe and H II regions in this galaxy and discuss it in comparison with stellar evolution models.

Methods. Data for eight PNe and one H II region were obtained with the high-resolution spectrograph *Magellan* Inamori Kyocera Echelle (MIKE) at Las Campanas Observatory, Chile. Data for three PNe, six compact H II regions, and nine knots or clumps in extended H II regions were obtained with the high-resolution spectrograph Manchester Echelle Spectrometer (MES) attached to the 2.1m telescope at the Observatorio Astronómico Nacional, SPM, B.C., Mexico. An additional object was obtained from The SPM Catalogue of Extragalactic Planetary Nebulae. Thus, in total we have high-quality data for nine of the 20 PNe detected in this galaxy, and many H II regions. In the wavelength calibrated spectra, the heliocentric radial velocities were measured with a precision better than 7.8 km s^{-1}. Data for blue supergiant stars were collected from the literature to be included in the analysis. The heliocentric radial velocities of the different objects were compared to the velocities of the H I disk at the same position. Physical conditions and ionic abundances of PNe and H II regions were obtained from the emission lines, and we used recent ionization correction factors to derive the total chemical abundances.

Results. From the analysis of radial velocities we found that H II regions in NGC 3109 share the kinematics of the H I disk at the same projected position with very low dispersion in velocities. Blue supergiant stars and PNe rotate in the same direction as the H I disk but these objects have much larger dispersion; this larger dispersion is possibly because these objects belong to a different population that is located in the central stellar bar reported for this galaxy. From the chemical abundance determinations we demonstrate that PNe are enriched in O and Ne. The average O abundance in H II regions is 12 + log O/H = 7.74 ± 0.09 and PNe show significantly higher oxygen abundance by 0.43 dex in average. Ne abundance are about three times larger in PNe than in H II regions. This is a very important result showing that because of the low metallicity in the galaxy, O and Ne in PNe have been enriched by their progenitors in nucleosynthesis processes and brought to the surface during third dredge-up events. Our PN abundances are better reproduced by some nonstandard stellar evolution models for a metallicity of $Z = 0.001$, similar to the metallicity of H II regions. Abundances in H II regions show no metallicity gradient in this galaxy. We discuss a possible connection between the kinematics and chemistry.

Key words. ISM: abundances – ISM: kinematics and dynamics – H II regions – planetary nebulae: general – Galaxy: abundances – galaxies: dwarf

1. Introduction

The analysis of extragalactic PNe kinematics allows us to trace low-intermediate mass stars kinematics. Kinematics of PNe has been studied in elliptical, spiral, and S0 galaxies for comparison with the kinematics of other stellar populations and to determine the galactic mass (see, e.g., Merrett et al. 2006; Coccato et al. 2009; Cortesi et al. 2013; Longobardi et al. 2013, and references therein). For example, M31 has been deeply analyzed by Merrett et al. (2006) who found that PNe lying close to M31 major axis show a rotation curve with a wide spread in velocities at small radii, which is indicative of a contribution from the barred bulge. By contrast, Herrmann & Ciardullo (2009) studied 550 PNe belonging to five face-on spirals (IC 342, M74, M83, M94, and M101) to determined their kinematic mass.

The kinematics of PNe in dwarf irregular galaxies has been less studied. The Local Group member IC 10 was analyzed by Gonçalves et al. (2012), who studied the relation of the PN population and the H I envelope. For this case they reported a kinematical connection between both populations. In NGC 6822, PN kinematics was analyzed by Flores-Durán et al. (2014), who found significant differences between the PNe velocities and the velocities of the H I disk at the same position. These authors reported that, in NGC 6822, PNe share the rotation of the middle-age C stars.

NGC 3109 is a Magellanic-type galaxy classified as a late spiral SB(s)m. It is the dominant member of a group of galaxies at the edge of the Local Group, which includes the irregulars Sextans A, Sextans B, and the dwarf elliptical Antlia Dwarf.

⋆ Based on data obtained at Las Campanas Observatory, Carnegie Institution, Chile.
⋆⋆ Based on data collected at the Observatorio Astronómico Nacional, SPM, B.C., Mexico.

The structure of NGC 3109 is complex. In the optical it seems to contain a gas-rich rotating disk and a halo of old stars (Minniti et al. 1999). Such a disk seems to be oriented edge-on and has an elongated shape that is aligned almost E-W with an extension of about 17.4 × 3.5 arcmin. A huge disk of H I, which is aligned with the optical disk and encompasses it, was mapped by Barnes & de Blok (2001). These authors found that such a disk is warped and suggested that this could be evidence of a possible encounter with the Antlia Dwarf approximately one billion years ago. Peña et al. (2007a) reported the discovery of 20 PNe in NGC 3109 and Peña et al. (2007b) analyzed the chemistry of some of them and found that the O abundance in PNe is systematically higher than in H II regions, which is a very unusual situation.

H I disk kinematics was presented in detail by Ott et al. (2012) and analyzed extensively by Carignan et al. (2013), who extended the analysis up to a size of 58 × 27 arcmin.

Star formation has been very active in NGC 3109 as indicated by the large number of H II regions it contains. This is one of the most metal-poor galaxies in the vicinity of the Local Group with metallicity and luminosity that are lower than the values of the Small Magellanic Cloud. The main physical properties of NGC 3109 are listed in Table 1.

In this work we aim to study, in a global way, the PNe and compact H II regions in this galaxy with a twofold purpose. First we analyze the kinematics of these nebulae and compare them with the H I disk kinematics, and second, we determine chemical abundances of PNe in comparison with the abundances of H II regions to understand the chemical evolution of the central stars in a very low metallicity environment. Finally we discuss a possible relation between the kinematics of nebulae and their chemistry. The objects analyzed in this work are listed in Table 2.

A similar analysis was performed by our group in NGC 6822 (García-Rojas et al. 2016; Flores-Durán et al. 2014), where we studied the chemical behavior of photoionized nebulae and their kinematics relative to the H I disk and the huge spheroid of C stars in this galaxy. There we probed that the young population (H I and H II gas) and intermediate-age population (C stars and PNe) display different kinematics and chemistry. NGC 3109 does not possess such an extensive halo of C stars. The brightest members of such a population were studied by Demers et al. (2003) and these members are distributed in and near the disk of NGC 3109, as most of its stellar component.

This paper is organized as follows: in Sect. 2 we present the observations and data reduction, as well as the radial velocities derived for the different objects. In Sect. 3 the velocities of PNe, compact H II regions, and knots or clumps found in extended H II regions are discussed and compared to the velocities of the H I disk. In this section we also present the results of the kinematical analysis. In Sect. 4 the chemical abundances of PNe and H II regions are calculated and discussed. A discussion on a possible relation between the kinematics and chemistry in the galaxy is contained in Sect. 5. Our general conclusions are presented in Sect. 6.

2. Data acquisition and reduction

High spectral-resolution data for nine PNe (PN3, PN9, PN10, PN11, PN13, PN14, PN16, PN17, and PN20; here and in the following the object names are after Peña et al. 2007a) and one H II region were obtained with the double echelle *Magellan* Inamori Kyocera Echelle spectrograph (MIKE) attached to the 6.5 m *Magellan* Telescope Clay at Las Campanas Observatory (LCO), Chile. All but one of these objects were observed during the nights March 7 and 8, 2014. Another PN (PN10) was observed on May 9, 2006 (Peña et al. 2007a). The observed objects and their coordinates are listed in Table 2.

Table 1. Physical properties of NGC 3109.

Property	Value	Ref.
Hubble type	SB(s)m	(1)
Other ID	DDO 236, UGCA 194	
RA (J2000)	10h 03m 06.9s	(1)
Dec (J2000)	–26° 09′ 34″	(1)
Distance (Mpc)	1.30 ± 0.02	(2)
Systemic Vel. (km s^{-1})	404 ± 2	(3)
PA (deg)	95.0 ± 2.0	(3)
Inclination (deg)	69.5 ± 1.5	(3)
$E(B-V)$	0.087 ± 0.012	(2)
M_V	–14.9 ± 0.1	(4)
$M_\star$ (10^6 $M_\odot$)	76	(4)
$M_{\rm HI}$ (10^6 $M_\odot$)	460	(3)
12 + log(O/H), H II	7.77 ± 0.07	(5)
12 + log(O/H), PN	8.16 ± 0.19	(5)
12 + log(O/H), B-type	7.76 ± 0.07	(6)
Z	0.0015	
$Z/Z_\odot$	0.13	

References. (1) de Vaucouleurs et al. (1991); NASA/IPAC Extragalactic Database; (2) Soszyński et al. (2006); (3) Carignan et al. (2013); (4) McConnachie (2012), and references therein; (5) Peña et al. (2007b); (6) B-type supergiants analyzed by Evans et al. (2007).

The MIKE spectrograph operates with two arms, allowing one to obtain a blue and a red spectrum simultaneously (Berstein et al. 2003). The standard set of gratings was employed, thus the wavelength coverage was from 3350 to 5050 Å in the blue and from 4950 to 9400 Å in the red. During the observing runs the seeing was better than 1″, most of the time. A binning of 2 × 2 was used obtaining a spatial scale of 0.2608″/pix. For the PNe and H II regions a slit size of 1″ × 5″ was used, thus the spectral resolution obtained was from 0.14 to 0.17 Å in the blue and from 0.23 to 027 Å in the red. Three standard stars for flux calibration were acquired (HR 4468, Hilter 600, and HD 49798) with a slit size of 2″ × 5″, to include all the stellar flux.

Several compact H II regions and PNe (listed in Table 3), and some clumps in extended H II regions, not classified previously, were observed at the Observatorio Astronómico Nacional San Pedro Mártir (OAN-SPM), B.C., Mexico, with the 2.1 m telescope and the Manchester Echelle Spectrometer (MES; Meaburn et al. 1984, 2003) in the nights February 4 to 9, 2014.

The MES (OAN-SPM) is a long-slit echelle spectrometer that uses narrowband filters to isolate the orders containing the emission lines of interest. For our observations the order including the Hα and [N II] 6548, 6583 Å emission lines was used. All the observations were made with a slit width of 150 μm, equivalent to 1.9″ on the sky. The slit length is 6.5′ and it was oriented E-W, along the disk of NGC 3109, therefore several objects and H II knots were included in the slit (see Fig. 1).

The MES (OAN-SPM) was coupled with a 2048 × 2048 pix Marconi2 CCD with 13.5 μm pixel size, binned 2 × 2. The resulting plate scale was 0.356″/pixel, and the spectral resolution, approximately of 0.10 Å/pix, was equivalent to 11 km s^{-1}. Immediately before or after every science observation, a Th−Ar lamp spectrum was obtained for wavelength calibration. The internal precision of the lamp calibrations is better than ±1.0 km s^{-1}.

Table 2. PNe[a], compact H II regions[a], and H II knots or clumps analyzed in NGC 3109.

Object	RA (2000)	Dec (2000)	Other ID
PN3[b,c]	10:02:49.15	–26:09:10.1	–
PN9[b,c]	10:03:02.66	–26:08:50.3	–
PN10[b,c]	10:03:03.91	–26:09:42.3	PN6[d]
PN11[b]	10:03:05.04	–26:10:54.2	–
PN13[b,c]	10:03:08.52	–26:09:07.7	–
PN14[b]	10:03:10.34	–26:08:06.1	–
PN16[b]	10:03:18.67	–26:09:58.8	–
PN17[b]	10:03:18.74	–26:10:05.4	–
PN20[b,c]	10:03:25.51	–26:09:07.2	–
H II 4[c]	10:02:50.66	–26:09:35.9	near F2 H7[f]
H II 6[c]	10:02:52.03	–26:09:05.3	F2 H3[f]
H II 9a[c,g]	10:02:58.20	–26:08:45.8	PN7[a], PN1[d]
H II 10[c]	10:02:58.91	–26:08:48.3	RM 2[d], Ho 11[e]
H II 18[c]	10:03:03.77	–26:09:20.7	RM 6[d], D2 H5[f]
H II 30[b]	10:03:17.71	–26:09.59.4	near HII 10[d]
H II 37[c]	10:03:27.96	–26:09:19.9	–
H II 40[c]	10:03:28.51	–26:09:21.8	near F5 H4[f]
H II 41[c]	10:02:50.64	–26:08:44.0	F2 H5[f]
H II 42[c]	10:02:51.96	–26:09:24.4	F2 H6[f]
H II 43[c]	10:02:52.07	–26:09:08.1	F2 H3[f]
H II 44[c]	10:02:59.46	–26:08:48.2	–
H II 45[c]	10:02:59.47	–26:09:01.8	–
H II 46[c]	10:02:59.61	–26:08:45.6	–
H II 47[c]	10:03:03.86	–26:09:08.4	D2 H5[f]
H II 48[c]	10:03:12.45	–26:08:49.7	D2 H1[f]
H II 49[c]	10:03:27.84	–26:10:23.0	–

Notes. [(a)] Names as in Peña et al. (2007a). H II 41–49 are knots or clumps in extended H II regions. [(b)] Observed at LCO with MIKE. [(c)] Observed with MES. [(d)] Richer & McCall (1992), [(e)] Hodge (1969), [(f)] Bresolin et al. (1993). [(g)] This object, classified as a PN by Richer & McCall (1992), was finally identified as a H II region in Peña et al. (2007b), here we renamed it as H II 9a.

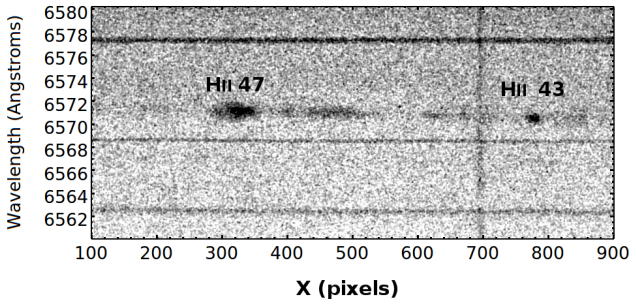

Fig. 1. Example of a Hα 2D image obtained with MES-SPM showing two H II clumps inside an extended H II region. The slit size was 1.9″ along the dispersion axis, and 6.5′ in the spatial direction, oriented E-W. The Hα emission of the galaxy shows a gradient in wavelength, relative to the sky lines, due to rotation.

The total exposure times for each object, observed with MIKE or MES, are presented in Table 3. Kinematic data for two additional objects (PN10 and H II 9a) were extracted from The San Pedro Mártir Kinematic Catalogue: Extragalactic Planetary Nebulae (SPM KINCAT) by Richer et al. (2010).

Table 3. Exposure times.

	Exp. time (s)	
id	MIKE	MES
PN3	1800	–
PN9, H II 44, H II 48	2700	900
PN10	6 × 900	3600[a]
PN11	2700	1800
PN13	1800	–
PN14	900	–
PN16	1800	–
PN17	900	–
PN20	3600	3600
H II 4, H II 41	–	3600
H II 9a	–	3600[a]
H II 6, H II 43	–	3600
H II 10, H II 45, H II 46	–	1800
H II 18	–	1800
H II 30	900	–
H II 37, H II 49	–	1200
H II 40	-	1800
H II 42, H II 47	–	1800

Notes. [(a)] Data from SPM KINCAT of PNe.

2.1. Data reduction

Data reduction of LCO Clay-MIKE spectra was carried out with IRAF[1] echelle reduction packages. Data were bias subtracted and flat fielded. Spectra were extracted from the 2D frames with an extraction window of 3.13″, which includes all the emission of stellar objects and an important fraction (if not all) of the emission of compact H II regions. Wavelength calibration was performed with a Th−Ar lamp, observed immediately after each science exposure. The flux calibration was carried out employing the spectrophotometric standard stars mentioned above.

The data from MES (OAN-SPM) were reduced via the noao.twodspec.longslit package of IRAF. First, 2D frames were bias substracted and second, the data were extracted and wavelength-calibrated using a Th−Ar lamp. No flat-field correction was applied. The fits files retrieved from the SPM KINCAT provide wavelength-calibrated spectra. These data are not flux calibrated. The heliocentric velocity correction was applied for all the spectra.

3. Radial velocities

In this section the radial velocity behavior of our objects is analyzed and compared with the velocities of the H I disk at the same projected position.

3.1. The H I disk

Detailed observations with high-velocity resolution (0.6–2.6 km s^{-1}) of neutral hydrogen (H I) emission were obtained by Ott et al. (2012) with the VLA-ANGST (Very Large Array survey of Advanced Camera for Surveys Nearby Galaxy Survey Treasury galaxies) for 35 nearby dwarf galaxies, including NGC 3109. It is possible to access their data on the web site[2].

[1] IRAF is distributed by the National Optical Astronomy Observatories, which is operated by the Association of Universities for Research in Astronomy, Inc., under contract to the National Science Foundation.
[2] https://science.nrao.edu/science/surveys/vla-angst

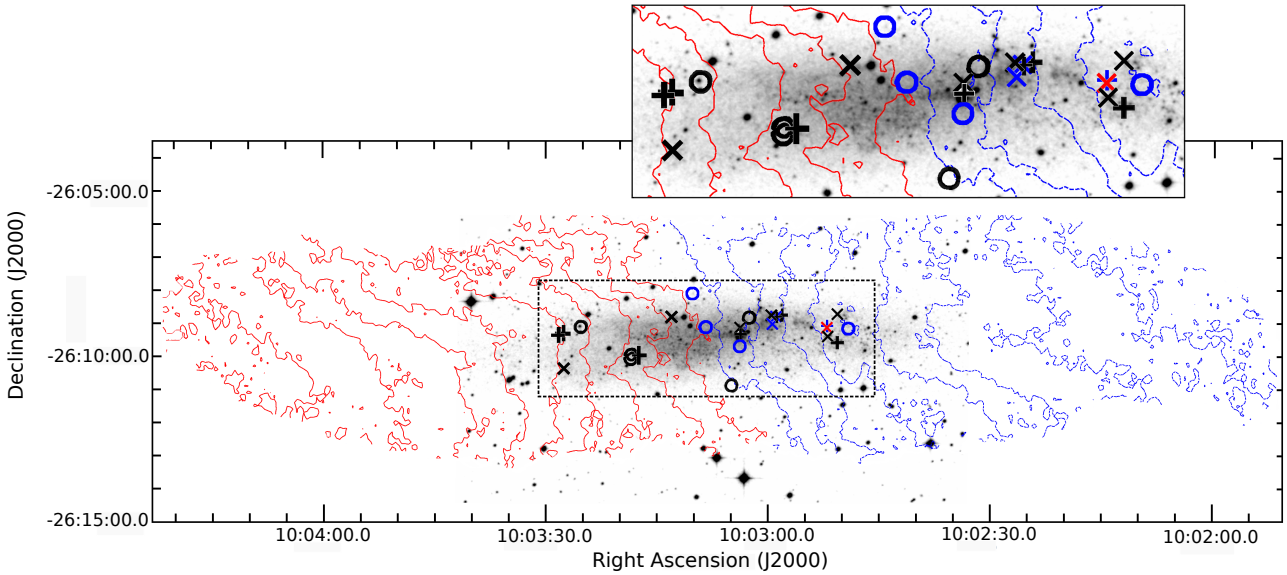

Fig. 2. Moment map of the H I in NGC 3109 (Ott et al. 2012). The blue contours run from 400 km s^{-1} in the center to 351 km s^{-1} in the west in steps of 7 km s^{-1}. Red contours run from 407 km s^{-1} in the *inner zone* to 463 km s^{-1} in the east. Positions of analyzed PNe (circles), H II regions (crosses), and H II knots (x symbols) are shown. Blue symbols indicate a negative difference and red symbols indicate a positive difference (larger than 12 km s^{-1}) between the observed objects and the H I velocities. We plot, in black, objects with a difference in velocity lower than 12 km s^{-1}, relative to H I disk.

Figure 2 is based on the H I data by Ott et al. (2012). This figure shows some interesting characteristics of the isovelocity contours of the H I disk, especially in the central zone. These contours are almost parallel to each other and almost orthogonal to the main axis of the disk, giving the appearance of a nearly solid-body type rotation. In addition it is clear that the H I disk is much larger in size than the optical galaxy, where the stars and the ionized gas reside. We refer to this in the following.

Previous to Ott et al. (2012), Jobin & Carignan (1990) obtained H I 21-cm line observations with the Very Large Array (VLA), and they constructed a position-velocity diagram from which they derived the rotation curve (RC) out to about 17 arcmin from the center; this is equivalent to 6 kpc if a distance of 1.3 Mpc is adopted. This early study reported a slowly rising RC, reaching a maximum rotational velocity of only 67 km s^{-1}. In addition, from surface photometry in the *I* band, these authors found that the orientation of the isophotes changes, giving strong evidence for the presence of a bar in NGC 3109.

Blais-Ouellette et al. (2003) combined high-resolution Fabry-Perot Hα emission, which is confined to the optical zone, with the H I 21-cm data to compute the RC. They showed that the ionized gas of NGC 3109 and the H I share the same kinematics. Their computed RC presents a nearly solid-body type behavior rising linearly and slowly up to a velocity of about 45 km s^{-1} at 2.5 kpc and then it rises more slowly getting 65 km s^{-1} at a distance of about 7 kpc from the center.

As mentioned in the introduction, Carignan et al. (2013) reported a H I disk of 58 × 27 arcmin in size, which is approximately four times larger than the optical disk. The RC calculated by Carignan et al. (2013) coincides very well with the RC derived by previous authors and it shows that the rotation velocity continues slowly increasing up to 12 kpc, where it gets a value of about 80 km s^{-1}. In addition, these authors analyzed the H I isophotes and photometric distribution in the *B*, *I*, and 3.6 μm bands, which are sampling different stellar populations; they found that the inclination and thickness of the disk changes with each band and that the H I disk is really composed of two disks with different inclinations.

Jobin & Carignan (1990), Blais-Ouellette et al. (2003), and Carignan et al. (2013) used the RC to model the mass distribution of the dark matter (DM) halo in the galaxy. Such models led the authors to conclude that NGC 3109 is entirely dominated by DM at nearly all radii. According to these authors, the model that best fit the RC is the observationally motivated pseudo-isothermal (ISO) DM halo with a flat-density core profile, contrary to the cosmological Navarro-Frenk-White models which predict a cuspy central halo for these type of galaxies. It is worthwhile to say that such a galaxy dominated by DM at all radii could not produce a bar since bars are formed by barionic matter (stars) and can be formed if the barionic matter centrally dominates (see references below).

A cosmologically motivated model for the DM halo distribution, containing a cuspy central DM density, was computed by Valenzuela et al. (2007) for NGC 3109. The DM component is globally dominant but the model is centrally dominated by barions, therefore it is unstable to bar formation. The best model by Valenzuela et al. (2007) develops a weak stellar bar that extends in radius to about 1 kpc, in about 100 Myr. The idea of a barred galaxy is supported by the change in orientation of the isophotes shown in the surface photometry (Jobin & Carignan 1990).

3.2. Is there a bar in the central zone of NGC 3109?

Several authors have suggested that NGC 3109 is a barred galaxy (see, e.g., the classification by de Vaucouleurs et al. 1991). As described above, the twist of the stellar isophotes in the *B* and *I* bands (Jobin & Carignan 1990) supports the idea of a barred galaxy. However a DM centrally dominated galaxy, as

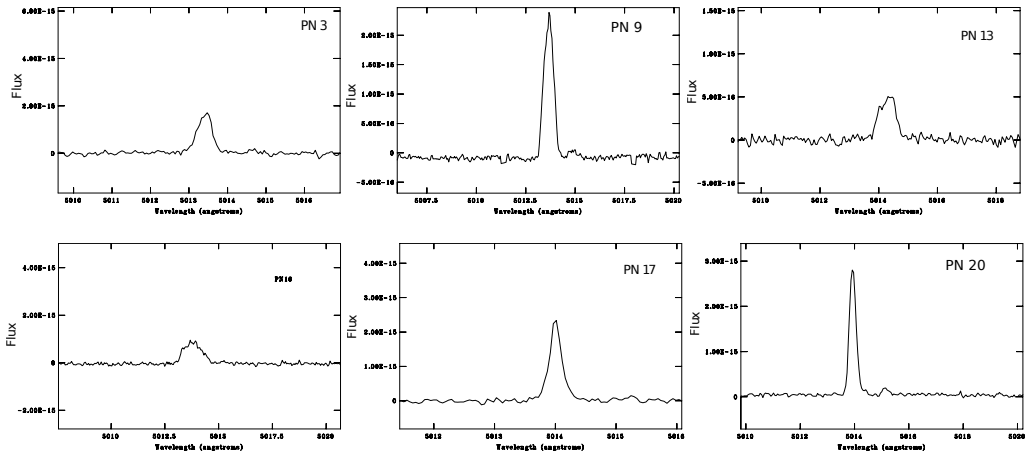

Fig. 3. [O III]λ5007 emission lines of PNe from the spectra obtained with MIKE spectrograph at LCO.

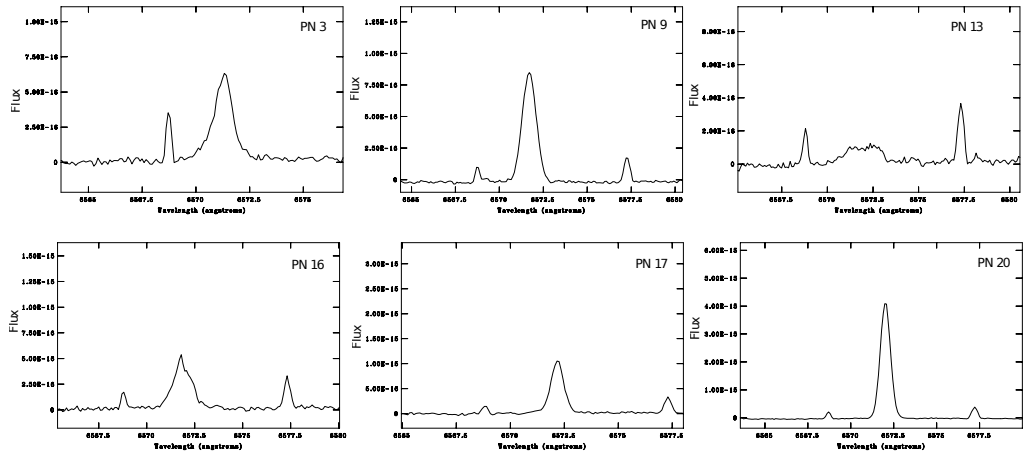

Fig. 4. Hα and [N II] emission lines of PNe from the spectra obtained with MIKE spectrograph at LCO.

the ISO model computed by, for example, Carignan et al. (2013), would not develop a bar. The physical reasons why a DM centrally dominated galaxy does not develop a bar can be found in Weinberg (1985), Debattista & Sellwood (2000), and references therein. Only the cosmological DM models by Valenzuela et al. (2007) predict the presence of a bar of 1 kpc long, which is small compared with the size of the optical zone in NGC 3109 of about 5 kpc.

The kinematics of a bar-like structure should be reflected in the RC as a linear increase in velocity. This agrees with the RC by Blais-Ouellette et al. (2003) for the ionized and neutral gas in the center. The RC increases linearly reaching 40 km s^{-1} at 2.5 kpc from the center and beyond this point it increases more slowly.

Therefore the evidence for a central bar seems solid. Such a structure would rotate with a linear RC, but the components would rotate in different directions inside the bar, showing a dispersion in velocities. Our PNe, as pertaining to the middle-age stellar population would be part of the bar and their kinematics could show this fact. But there are only nine objects and it is difficult to extract valid conclusions, therefore for the analysis we include the kinematical data for other stellar components, which are the blue supergiant stars studied by Evans et al. (2007).

3.3. Kinematics of PNe, compact H II regions, and blue supergiant stars

Several emission lines were measured in the MIKE high-resolution spectra of the observed nebulae to determine their radial velocities. In Figs. 3 and 4, the [O III] λ5007 and Hα and [N II] line profiles, obtained with this instrument, are presented. In the case of MES (OAN-SPM) data, Hα line was used to determine the observed objects velocities.

For all cases, radial velocities were calculated by a Gaussian fit to the emission lines, and they were corrected to heliocentric velocities, $V_{\rm helio}$. The uncertainties listed in Table 4 correspond to the standard deviation of the measurements. For some PNe we have independent observations with both instruments and we find that the differences in radial velocities are less than 6 km s^{-1} between both sets of observations. We therefore conclude that our radial velocities have an absolute precision better than the maximum error found which is 7.8 km s^{-1}.

Using the H I disk velocity field, we compared $V_{\rm helio}$ of PNe and H II regions with those of the H I gas at the same projected position. The results are shown in Table 4 where we present, for all our objects, the derived $V_{\rm helio}$ and its uncertainty at 1σ (Cols. 2 and 3), and the H I velocity (Col. 4) at the corresponding

Table 4. Heliocentric velocities of PNe, H II regions (Col. 12), and the H I gas at the same projected position.

Object	V_{helio} km s^{-1}	±error km s^{-1}	V_{HI} km s^{-1}	Δ km s^{-1}	Δ_{sys} km s^{-1}
PN3	376.4	6.0	371.8	–4.6	–27.6
PN9	402.4	3.9	394.1	–8.3	–1.6
PN10	409.0	2.0	396.5	–12.5	+5
PN11	403.8	3.4	403.3	–0.5	–0.2
PN13	429.5	2.1	405.8	–23.7	+25.5
PN14	465.2	7.8	405.3	–59.9	+61.2
PN16	412.3	5.2	418.1	+5.8	+8.3
PN17	426.4	1.5	418.7	–7.6	+22.4
PN20	424.7	4.5	430.1	+5.4	+20.7
H II 4	385.3	0.1	377.9	–7.4	–18.7
H II 9a	385.7	0.4	386.6	+0.9	–18.3
H II 6	390.5	0.1	375.9	–14.6	–13.5
H II 10	392.8	0.5	385.7	–7.1	–11.3
H II 18	395.3	0.1	396.7	+1.4	–8.7
H II 30	411.8	2.5	415.5	+3.7	+7.8
H II 37	428.9	0.2	434.1	+5.2	+24.9
H II 40	426.5	0.1	434.6	+8.1	+22.5
H II 41	375.7	0.1	377.0	+1.3	–28.4
H II 42	369.3	0.1	379.9	+7.6	–34.8
H II 43	356.9	0.1	375.7	+18.8	–47.1
H II 44	405.3	0.2	386.3	–19.1	+1.3
H II 45	408.3	0.4	389.3	–19.0	+4.3
H II 46	382.9	0.5	389.0	+6.1	–21.1
H II 47	388.3	0.1	395.3	+7.0	–15.8
H II 48	422.4	0.6	411.7	–10.7	+18.4
H II 49	424.1	0.6	431.7	+7.6	+20.1

Notes. Δ and Δ_{sys} are the differences $V_{HI} - V_{helio}$ and $V_{helio} - V_{sys}$, respectively.

position. Column 5 shows the difference $\Delta = V_{HI} - V_{helio}$, and in Col. 6 we present the difference between the observed velocity and systemic velocity (404 km s^{-1}).

The projected position of observed objects and their differences in velocity, relative to the H I disk, are illustrated in Fig. 2, where the velocity map of H I, as given by Ott et al. (2012), is shown. The difference in velocity of PNe and H II regions is indicated in blue or red if it is negative (objects approaching faster by more than 12 km s^{-1}) or positive (objects receding by more than 12 km s^{-1}), with respect to the H I disk. Objects with differences smaller than ±12 km s^{-1} are shown in black.

To better illustrate the differences in velocity among PNe, compact H II regions and knots in H II regions, and the H I disk, Fig. 5 shows their velocities (relative to the systemic velocity) versus their distance to the center (in kpc) projected along the major axis of the H I disk. Only the inner 5 kpc of the galaxy, where the stars and the ionized gas reside, are shown. The filled blue line represents the rotation of the H I disk and it shows some irregularities that so far have not been explained. At both sides of this line two dotted lines show the uncertainty given by Ott et al. (2012). From this figure the velocity gradient, at both sides of the center, can be calculated. We find that from the galactic center to the east the rotation velocity increases by 17.4 km s^{-1} kpc^{-1}, while from the center to the west, the velocity declines by 15.3 km s^{-1} kpc^{-1}. Both gradients are equal within the uncertainties given by the dotted lines.

In this figure it is clear that our H II regions (open squares) follow closely the rotation of the H I disk, this is in agreement with the results found by Blais-Ouellette et al. (2003) for the ionized gas. We find that the PNe (black dots) also rotate in the same

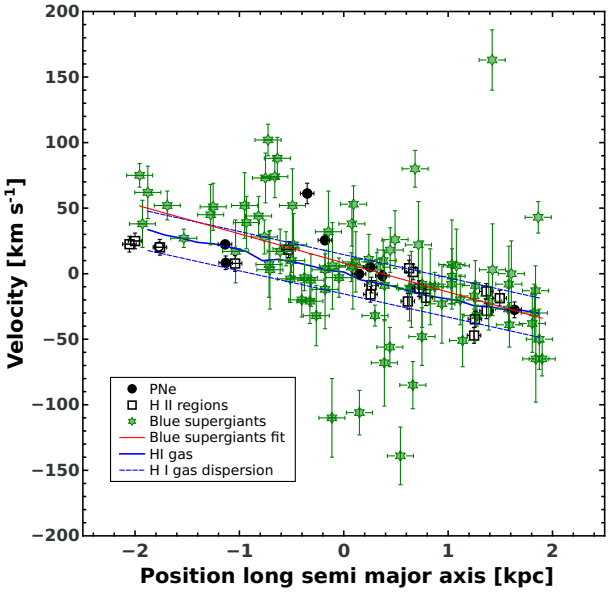

Fig. 5. Velocities of PNe, H II regions, and BSGs relative to the system versus their positions relative to the center, projected on the H I disk major axis. Solid and dotted blue lines show the rotation of the H I disk and its dispersion. The red line is a fit to the BSG velocities.

direction as the disk, although these objects present a much more disperse velocity field. One PN in particular shows a difference of about 60 km s^{-1}, relative to the system and to the H I disk; the projected location of this PN (PN14) is farthest away from the H I disk.

In the same figure, we included the radial velocities, relative to the system, of luminous blue supergiant stars (BSGs, green stars) as determined by Evans et al. (2007) from multiobject spectroscopy, although their data have lower resolution than the data in this work. The uncertainty given by Evans et al. (2007) for each object is shown; the mean uncertainty is of 19 km s^{-1}. The projected position of these objects along the major axis of the H I disk was calculated. As already indicated by Evans et al. (2007), the BSGs, that are relatively young objects and would belong to the stellar bar, show a rotation in the same direction as the H I rotation but with a large dispersion, even larger than that presented by our PN sample. If we trace a linear fit to the BSG data, a slightly steeper line is found (red line in Fig. 5). However, given the lower accuracy of the data for the BSGs, we consider that this small difference is not trustworthy. The distribution of BSGs in the galaxy (see Figs. 2 and 3 by Evans et al. 2007) spreads in a thicker zone than that of the H II regions, which also occurs with the distribution of PN candidates as presented by Peña et al. (2007a) in their Fig. 3. In our Fig. 2 this is not noticeable because only the objects analyzed in this paper are included there, and not the entire PN sample. It is clear that, from their distribution, BSGs and PNe represent different populations than the ionizing stars of H II regions.

4. Chemical abundances revisited

To analyze the chemical behavior of the photoionized nebulae in NGC 3109, we first need to calculate the physical conditions (electron temperature and density) and then the ionic abundances of elements present in the gas. In Table 5 we present dereddened line intensities for each object observed with MIKE-LCO. The

Table 5. Dereddened line intensities measured from MIKE spectra relative to Hβ = 1.00.

			PN3		PN9		PN11		PN13		PN14	
Ion	λ	$f(\lambda)$	$I/I(\mathrm{H}\beta)$	err	$I/I(\mathrm{H}\beta)$	err	$I/I(\mathrm{H}\beta)$	err	$I/I(\mathrm{H}\beta)$	err	$I/I(\mathrm{H}\beta)$	err
[O II]	3726.03	+0.280	–	–	–	–	–	–	–	–	–	–
[O II]	3728.82	+0.279	–	–	–	–	–	–	–	–	–	–
[Ne III]	3868.75	+0.241	–	–	0.37	0.13	0.82	0.15	–	–	–	–
Hϵ	3970.07	+0.214	–	–	–	–	0.47	0.61	–	–	–	–
Hδ	4101.74	+0.179	–	–	0.28	0.09	0.32	0.09	–	–	–	–
Hγ	4340.47	+0.119	–	–	0.45	0.09	0.45	0.07	–	–	–	–
[O III]	4363.21	+0.114	–	–	<0.06	–	0.11	0.06	–	–	–	–
He II	4685.68	+0.114	–	–	0.34	0.06	–	–	–	–	–	–
Hβ	4861.33	0	1.00	0.22	1.00	0.15	1.00	0.11	1.00	0.40	1.00	0.17
[O III]	4958.91	–0.021	0.77	0.13	1.65	0.24	2.92	0.32	1.11	0.50	–	–
[O III]	5006.84	–0.031	2.99	0.43	5.17	0.61	8.89	0.99	2.33	0.40	–	–
[Ar III]	5191.82	–0.069	–	–	–	–	0.09	0.02	–	–	–	–
He I	5875.64	–0.194	–	–	–	–	–	–	–	–	–	–
[N II]	6548.03	–0.298	–	–	0.12	0.05	0.05	0.02	–	–	–	–
Hα	6562.82	–0.301	2.87	0.33	2.86	0.33	2.91	0.31	2.73	0.40	2.60	0.66
[N II]	6583.41	–0.304	0.19	0.13	0.30	0.05	0.07	0.01	–	–	–	–
[S II]	6716.47	–0.323	0.53	0.30	0.20	0.04	–	–	–	–	–	–
[S II]	6730.85	–0.325	0.24	0.08	0.16	0.03	–	–	–	–	–	–
He I	7065.28	–0.369	–	–	–	–	0.15	0.03	–	–	–	–
[Ar III]	7135.78	–0.378	–	–	0.13	0.09	–	–	–	–	–	–
$c(\mathrm{H}\beta)$			0.7		0.09		0.41		–		–	
log $F(\mathrm{H}\beta)$			–15.58		–15.55		–15.47		–16.03		–16.41	

			PN16		PN17		PN20		H II 30	
Ion	λ	$f(\lambda)$	$I/I(\mathrm{H}\beta)$	err	$I/I(\mathrm{H}\beta)$	err	$I/I(\mathrm{H}\beta)$	err	$I/I(\mathrm{H}\beta)$	err
[O II]	3726.03	+0.280	–	–	–	–	1.35	0.21	1.69	0.31
[O II]	3728.82	+0.279	–	–	–	–	1.86	0.28	2.11	0.32
[Ne III]	3868.75	+0.241	–	–	–	–	0.11	0.04	–	–
Hϵ	3970.07	+0.214	–	–	–	–	0.20	0.06	–	–
Hδ	4101.74	+0.179	–	–	–	–	0.31	0.05	0.31	0.09
Hγ	4340.47	+0.119	0.34	0.09	0.45	0.13	0.47	0.06	0.52	0.08
[O III]	4363.21	+0.114	<0.06	–	<0.03	–	<0.02	–	–	–
He II	4685.68	+0.114	–	–	–	–	–	–	–	–
Hβ	4861.33	0	1.00	0.23	1.00	0.17	1.00	0.11	1.00	0.13
[O III]	4958.91	–0.021	1.81	0.36	0.78	0.11	0.33	0.04	0.28	0.05
[O III]	5006.84	–0.031	5.26	0.74	2.20	0.26	0.95	0.11	1.05	0.13
[Ar III]	5191.82	–0.069	–	–	–	–	–		–	–
He I	5875.64	–0.194	–	–	–	–	0.04	0.01	–	–
[N II]	6548.03	–0.298	–	–	–	–	0.05	0.01	–	–
Hα	6562.82	–0.301	2.86	0.36	2.87	0.35	2.90	0.30	2.96	0.31
[N II]	6583.41	–0.304	0.08	0.03	0.19	0.04	0.17	0.02	0.09	0.03
[S II]	6716.47	–0.323	0.16	0.10	–	–	0.18	0.02	0.12	0.02
[S II]	6730.85	–0.325	0.11	0.07	–	–	0.14	0.02	0.07	0.01
He I	7065.28	–0.369	–	–	–	–	–	–	–	–
[Ar III]	7135.78	–0.378	–	–	–	–	0.06	0.01	0.04	0.04
$c(\mathrm{H}\beta)$			0.03		0.05		0.28		0.79	
log $F(\mathrm{H}\beta)$			–15.68		–15.58		–15.05		–15.02	

table includes the logarithmic reddening correction, $c(\mathrm{H}\beta)$, and the Hβ observed flux, $F(\mathrm{H}\beta)$. The value $c(\mathrm{H}\beta)$ was derived from the Balmer ratio Hα/Hβ, by assuming case B recombination theory (Storey & Hummer 1995), the reddening law by Seaton (1979), and an electron temperature of 10^4 K. Uncertainties correspond to the standard deviation of the Gaussian fit for the line, plus 10% due to possible errors in the flux calibration procedure. In the third column we present the reddening function used. We used IRAF V2.16 for data reduction and analysis.

Owing to the faintness of these objects, the temperature sensitive [O III]$\lambda\lambda$4363/5007 line ratio was obtained in very few objects. Hence we recalculated physical conditions and ionic abundances of PNe and H II regions using the line intensities given by Peña et al. (2007b), which were acquired from observations performed with FORS1 spectrograph attached to the Very Large Telescope (ESO-VLT) in 2006. The calculations were obtained using the IRAF tasks TEMDEN and IONIC in the STSDAS package.

Electron temperatures (T_e) were derived from [O III] $\lambda\lambda$4363/5007 line ratios and electron densities (n_e), from the density-sensitive [S II]$\lambda\lambda$6717/6731 line ratios. When such [S II] line ratios were not available a density of 500 cm^{-3} was chosen for PNe and of 100 cm^{-3} for H II regions. We adopted the simplistic assumption that n_e is uniform in the nebula and equal to the value given by the [S II]$\lambda\lambda$6717/6731 ratio. We also assumed that T_e is uniform and equal to that given by the [O III]$\lambda\lambda$4363/5007 line ratio. Derived values are listed in Table 6.

Table 6. Electron temperatures, densities, and ionic abundances (10^{-6}).

	n_e (cm^{-3})	T_e(K)	He^+	He^{++}	O^+	O^{++}	N^+	Ne^{++}	S^+	Ar^{++}
PN3	140^{+800}_{-40}	$12\,013^{+1349}_{-1389}$	0.116	<0.003	8.2	110.6	0.99	19.28	0.11	0.24
PN4	500	$11\,846^{+897}_{-1276}$	<0.029	0.071	<2.70	116.6	<0.78	26.60	<0.20	–
PN9[a]	213^{+14}_{-22}	$<12\,336^{+643}_{-517}$	–	–	–	94.12	3.53	17.14	0.536	0.757
PN10	500	$10\,588^{+944}_{-1128}$	0.072	<0.005	<10.5	208.6	0.85	25.04	<0.25	0.48
PN11	500	$13\,495^{+1463}_{-1664}$	0.095	<0.003	–	125.3	0.78	18.27	<0.06	0.19
PN11[a]	500	$12\,387^{+1806}_{-2587}$	–	–	–	159.5	0.82	37.43	–	–
PN13	500	$16\,484^{+4834}_{-3772}$	0.141	<0.018	<2.27	119.8	2.03	9.82	–	–
PN16[a]	310^{+35}_{-50}	$12\,110^{+1280}_{1120}$	–	–	–	100.9	0.98	–	0.47	–
PN17	480^{+20}_{-30}	$12\,536^{+1278}_{-2082}$	0.085	<0.003	5.68	69.9	1.48	3.07	<0.09	0.11
PN20[a]	169^{+8}_{-10}	$14\,345^{+790}_{-637}$	0.029	–	31.82	11.38	1.45	3.03	0.35	0.26
H II 4	100^{+10}_{-10}	$16\,489^{+1366}_{-1976}$	0.082	–	–	20.4	0.9	2.5	0.30	0.22
H II 7	100^{+40}_{-10}	$15\,295^{+1157}_{-1107}$	0.082	–	13.7	31.6	0.6	4.3	0.24	0.30
H II 9[a]	520^{+1480}_{-420}	$15\,542^{+1298}_{-1542}$	0.097	–	7.81	54.5	0.6	8.8	0.12	–
H II 11	120^{+350}_{-20}	$14\,738^{+2068}_{-2021}$	0.090	–	22.0	28.4	0.9	3.4	0.36	–
H II 15	100	$13\,795^{+2259}_{-1741}$	0.104	–	18.5	47.1	1.2	6.9	0.58	–
H II 17	–	$14\,040^{+2236}_{-2464}$	0.084	–	20.5	34.5	1.1	2.9	–	–
H II 20	100	$13\,517^{+1499}_{-1733}$	0.108	–	20.7	55.1	1.1	5.3	0.37	–
H II 30	120^{+610}_{-20}	$11\,877^{+3196}_{-4428}$	0.082	–	33.9	30.8	1.0	4.0	0.36	0.31
H II 32	100	$13\,491^{+1135}_{-914}$	0.078	–	20.7	28.8	1.7	4.8	0.56	0.36
H II 37	100	$13\,689^{+1018}_{-1183}$	0.079	–	17.9	55.2	0.5	6.4	0.22	–
H II 40	160	$13\,682^{+1340}_{-1208}$	0.078	–	11.7	40.1	0.5	5.3	0.16	–

Notes. [(a)] From data obtained with MIKE spectrograph at LCO.

Ionic abundances were derived from the following line intensities: He I λ5876, He II λ4686, [O II]λ3727, [O III]λ5007, [N II]λ6583, [Ne III]λ3869, [S II]λ6717+6731, [Ar III]λ7135, relative to Hβ, and the physical conditions described above. When a line was not detected, its upper limit was used to compute an upper limit for the corresponding ionic abundance. The results are presented in Table 6.

To derive total abundances it is necessary to take unseen ions into account. Usually this correction is performed by means of ionization correction factors (ICFs). In this work, for PNe we use the expressions recently published by Delgado-Inglada et al. (2014; D-I.14) instead of those by Kingsburg & Barlow (1994; K&B), used by Peña et al. (2007b). The ICFs by D-I.14 represent an improvement relative to K&B ICFs because they are based on a huge number of photoionization models that explore a wide space of parameters and use the most updated atomic parameters and atomic physics, and they were successfully compared with observations. The ionic abundances listed in Table 6 were used. Total abundances derived this way are presented in Table 7. In most of the cases, D-I.14 ICFs can be applied; however, PN9 and PN11 show $\omega = O^{2+}/(O^+ + O^{2+}) \geq 0.95$, which is out of the validity range of such ICFs. A different procedure, described below, was used for these objects.

To evaluate the differences between D-I.14 ICFs and K&B ICFs, we applied the latter to the data in Table 6 to determine total abundances. It is found that differences in O/H abundances are lower than 0.05 dex, for N/H abundances differences are lower than 0.1 dex, and for Ne/H abundances differences are lower than 0.08 dex. Ar/H abundances however could present large differences up to 0.3 dex and S/H abundances show differences up to 0.35 dex.

Then, at least for N, O, and Ne, K&B ICFs can be used for those objects where D-I.14 ICFs are not valid. First let us consider the case of PN11, this is a high excitation nebula for which only O^{2+} was detected. Owing to its high excitation we can consider that O^+ abundance is very low, and if we take into account that He II λ4686 was not detected, then no O^{3+} is expected in this nebula. Hence it can be assumed that the total O abundance is slightly higher than the O^{2+} abundance. Under these considerations, it is obtained that $12 + \log$ O/H $\sim 8.20 \pm 0.10$ for PN11, which is, within uncertainties, similar to the value derived from VLT-FORS1 data of the same object. Ne and Ar were derived using K&B ICFs. Similar methods were used for PN9 and PN16.

The case of PN20 is different. This object is a very low excitation nebula where O^{2+} abundance is lower than O^+ abundance. Then its total O abundance is simply the addition of these two ionic abundances. Other elemental abundances were calculated with K&B ICFs. In following sections we argue that this object is more probably a H II region.

K&B ICFs were used for determining total abundances in H II regions.The total abundances calculated for the 8 PNe and 12 H II regions (PN20 is considered a H II region) are listed in Table 7. Their behavior is shown in Figs. 6–8, which are discussed in the following.

4.1. Oxygen abundances

Peña et al. (2007b) reported that O abundances in PNe of NGC 3109 are larger, by 0.39 dex on average, than those found in H II regions. In this work, for a larger sample of objects, we found that the average difference in O abundances is 0.43 dex larger for PNe than for H II regions, for which the average $12 + \log$ O/H value is 7.74 ± 0.09. Then, we confirmed that PNe in NGC 3109 are O rich compared to the present ISM, represented by H II regions. Interestingly, Evans et al. (2007) found

Table 7. Chemical abundances for the PNe and H II regions in NGC 3109.

	He/H	12 + log(O/H)	12 + log(N/H)	12 + log(Ne/H)	12 + log(S/H)	12 + log(Ar/H)
PN3	0.119 ± 0.032	8.08 ± 0.05	7.25 ± 0.25	7.31 ± 0.25	6.51 ± 0.29	5.57 ± 0.16
PN4	0.101 ± 0.009	8.48 ± 0.29	<7.80	7.86 ± 0.16	–	–
PN9[a]	–	>7.97[b]	–	7.23:[b]	–	6.15:[b]
PN10	0.077 ± 0.023	8.36 ± 0.13	7.29 ± 0.23	7.42 ± 0.23	6.75 ± 0.13	5.63 ± 0.18
PN11	0.098 ± 0.051	8.09 ± 0.05	–	–	–	5.55[b] ± 0.20
PN11[a]	0.098 ± 0.051	8.20[b] ± 0.10	–	7.57[b] ± 0.10	–	–
PN13	0.158 ± 0.074	8.12 ± 0.20	8.06 ± 0.39	7.02 ± 0.39	–	–
PN16[a]	–	> 8.00	–	–	–	–
PN17	0.088 ± 0.022	7.89 ± 0.11	7.37 ± 0.24	6.50 ± 0.26	<6.56 ± 0.20	5.42 ± 0.32
PNe statistics[c]	0.096 ± 0.030	8.17 ± 0.17	7.49 ± 0.28	7.27 ± 0.30	6.61 ± 0.20	5.67± 0.12
PN20[a,d]	>0.029	7.64 ± 0.15	6.29 ± 0.20	6.90 ± 0.21	6.35 ± 0.25	5.69 ± 0.14
H II 4	0.082 ± 0.013	>7.29	–	6.36 ± 0.13	–	5.59 ± 0.10
H II 7	0.082 ± 0.018	7.60 ± 0.11	6.31 ± 0.11	6.75 ± 0.12	6.29 ± 0.09	5.76 ± 0.10
H II 9a	0.098 ± 0.023	7.80 ± 0.25	6.67 ± 0.10	7.00 ± 0.08	6.14 ± 0.21	–
H II 11	0.090 ± 0.026	7.67 ± 0.16	6.32 ± 0.21	6.74 ± 0.24	6.39 ± 0.14	–
H II 15	0.104 ± 0.031	7.80 ± 0.20	6.63 ± 0.15	6.95 ± 0.23	6.68 ± 0.14	–
H II 17	0.084 ± 0.030	7.72 ± 0.21	6.50 ± 0.22	6.63 ± 0.26	–	–
H II 20	0.108 ± 0.024	7.86 ± 0.15	6.62 ± 0.18	6.82 ± 0.23	6.48 ± 0.13	–
H II 30	0.082 ± 0.030	7.79 ± 0.27	6.32 ± 0.39	6.92 ± 0.54	6.41 ± 0.38	5.76 ± 0.41
H II 32	0.078 ± 0.014	7.66 ± 0.11	6.61 ± 0.11	6.89 ± 0.20	6.61 ± 0.09	5.86 ± 0.12
H II 37	0.079 ± 0.013	7.85 ± 0.11	6.36 ± 0.15	6.90 ± 0.15	6.31 ± 0.10	–
H II 40	0.078 ± 0.013	7.70 ± 0.13	6.31 ± 0.13	6.81 ± 0.14	6.13 ± 0.10	–
H II statistics	0.088 ± 0.026	7.74 ± 0.09	6.45 ± 0.14	6.80 ± 0.13	6.38 ± 0.15	5.73 ± 0.08

Notes. [(a)] From data obtained with MIKE spectrograph at LCO. [(b)] ICFs from Kingsburgh & Barlow (1994). [(c)] PN11[a] is not included in the statistics. [(d)] PN20 is reclassified as a H II region.

that the O abundance in their sample of eight B-type supergiant stars, also a young population, is similar to the value for H II regions (see Table 1) and therefore lower than the O abundances in PNe.

In our average values for PNe we did not consider PN20 (shown as an open circle in the diagrams), which appears as a very low excitation nebula (different from what is expected for a PN) with low O abundance. Owing to its spectral characteristics and its chemistry, this nebula appears more similar to a H II region than to a PN. PN20 was classified as a PN because of its stellar appearance and low luminosity central star (Peña et al. 2007a), but in the following we consider it to be a compact H II region and place it outside the statistics for PNe.

The O enrichment of PNe relative to H II regions is a very important result, which makes evident that O (and also Ne as we will discuss later) has been synthesized and dredged up to the stellar surface during the evolution of the progenitors of these PNe. The nucleosynthesis of fresh ^{16}O is produced via the reaction $^{12}C(\alpha,\gamma)^{16}O$ and, according to some stellar evolution models (see, e.g., Marigo 2001), surface O enrichment occurs in low metallicity stars with initial mass lower than ∼3.5 $M_{\odot}$, as a consequence of dredge-up events during the thermal pulses in the AGB phase. This O enrichment becomes negative at higher masses because of hot bottom burning (HBB), phenomenon where extra N enrichment is produced through envelope-burning conversion to N of dredged-up primary C.

Our results constitute crucial evidence confirming that low-intermediate mass stars may produce positive yields of oxygen. In the next sections we discuss our results in comparison with the predictions of some stellar evolution models for low-intermediate mass stars.

In Figs. 6 and 7, which are discussed in detail later, standard stellar evolution models by Karakas (2010, K10) and Fishlock et al. (2014, F14), and nonstandard models by Ventura et al. (2013, 2014b, V1314), and Ventura et al. (2014a, V14) are presented. These models represent the evolution of stars with different initial masses at different initial metallicities, and model values correspond to the surface stellar abundances at the end of the AGB phase.

We consider that the best models for our objects are those with the metallicity of the ISM in NGC 3109, reproducing well the chemical composition of our PNe sample. For the case of O, it is evident that some models by K10, with very low metallicity $Z = 0.0001$, show large enrichment for stars of initial masses, at the ZAMS, from 1.5 to 3 $M_{\odot}$. But no enrichment (or only a small one) is predicted for models with $Z = 0.001$ and 0.004. On the other hand, models by Ventura et al., with $Z = 0.001$ and 0.004, show O enrichment in stars with ZAMS initial masses from 1.5 to 3.5 $M_{\odot}$.

Thus, in comparison with models and considering that the metallicity of H II regions in NGC 3109 is $Z \sim 0.0015$ (corresponding to 0.13 $Z_{\odot}$ if solar values by Asplund et al. 2005 are assumed), we found that the observed O enrichment in PNe of this galaxy is better reproduced by Ventura et al. models with $Z = 0.001$, and that the central stars of PNe have initial masses, at the ZAMS, from 1.5 to 3 $M_{\odot}$.

4.2. N/O abundance ratios

Figure 6 (left and right panels) shows the observed values of log (N/O) as a function of 12 + log (O/H) for PNe (black dots) and H II regions (open squares). In comparison with the H II regions, the O enrichment of PNe mentioned above is evident. In addition, all PNe with available data, are N rich relative to H II regions by a factor of 10 in average. Extreme N enrichment is obtained in PN13, which has a N/O larger than 0.8 and is also very He rich, therefore it corresponds to a Peimbert Type I PN. In principle PNe with the most massive central stars,

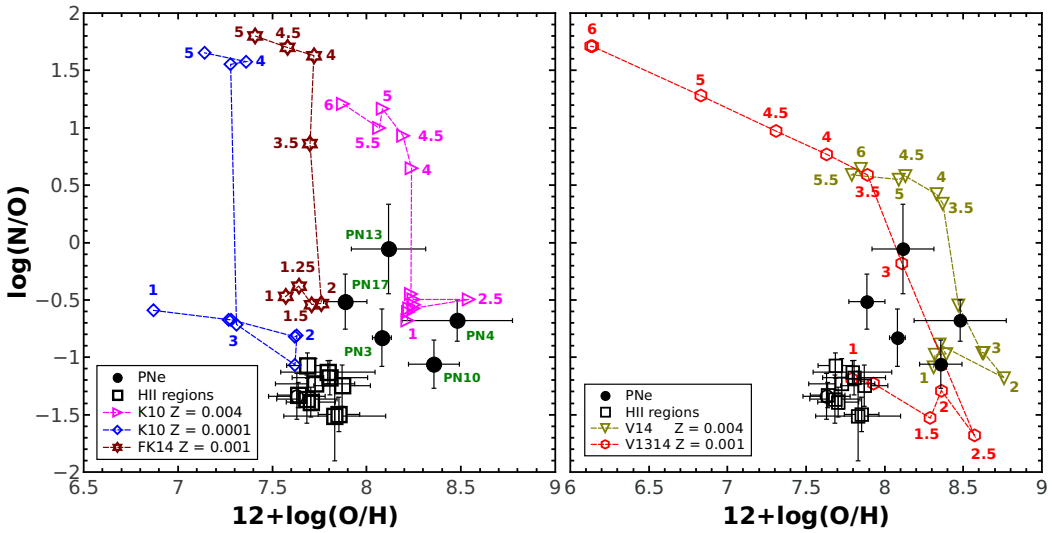

Fig. 6. log(N/O) versus 12 + log(O/H) for PNe (black dots), and H II regions (squares). The open circle corresponds to PN20, reclassified as a H II region. In the *left panel*, stellar evolution models for different metallicities by Karakas (2010, K10; $Z = 0.0001$, blue diamonds; $Z = 0.004$, magenta triangles) and Fishlock et al. (2014, F14; $Z = 0.001$, brown stars) have been included. In each metallicity sequence initial masses (at the ZAMS) of the progenitor stars are labeled for some models. In the *right panel* stellar evolution models for $Z = 0.001$ (red diamonds) by Ventura et al. (2013, 2014b, V1314) and $Z = 0.004$ (blue triangles) by Ventura et al. (2014a, V14) have been included. Again initial masses (at the ZAMS) of the progenitor stars are labeled for some models.

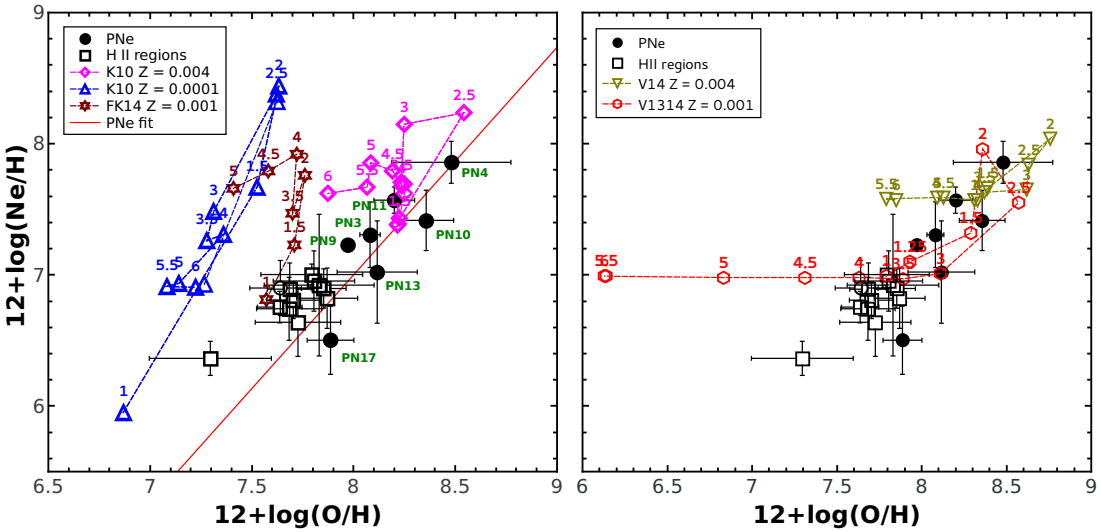

Fig. 7. 12 + log(Ne/H) versus 12 + log(O/H) for PNe (dots), and H II regions (open squares). Same stellar evolution models as in Fig. 6 have been included. In the *left panel* K10 models, with $Z = 0.0001$ (blue diamonds) and $Z = 0.004$ (magenta triangles), and FK14 models, with $Z = 0.001$ (brown stars), are presented. In the *right panel* models V1314 ($Z = 0.001$, red diamonds) and V14 ($Z = 0004$, green triangles) are shown. The ZAMS initial masses of the progenitor stars are labeled for some models in each metallicity sequence.

$M_{\odot} \geq 3\ M_{\odot}$, produce extra N enrichment by experiencing HBB, and this should be the case for PN13.

In Fig. 6, left panel, we show the behavior predicted by the stellar evolution models by K10 and F14 for metallicities $Z = 0.0001$, 0.001, and 0.004. In each metallicity sequence some models have been tagged with the ZAMS initial masses of stars. In this figure, it is found that our PNe lie nearer the models with metallicity $Z = 0.004$, which is in disagreement with the fact that the metallicity in NGC 3109 is about 0.0015. This occurs because models by F14 ($Z = 0.001$) and K10 ($Z = 0.004$) do not show O enrichment. In contrast, all these models predict that stars with initial masses larger than 2.5 $M_{\odot}$ produce large amounts of N, similar to the value shown by our Type I PN. According to the models, PN13 central star would have had an initial mass of about 3.5 $M_{\odot}$. However, K10 and F14 models do not reproduce the low N/O abundance ratio of PN3 and PN10.

In the right panel of Fig. 6 we explore the behavior of log (N/O), in comparison with the stellar evolution models by Ventura et al. (2013, 2014b, V1314), for $Z = 0.001$ and Ventura et al. (2014a, V14), for $Z = 0.004$. For the same progenitor stars, these models predict lower N/O ratios than the models by K10 and F14. Within uncertainties, our objects follow more closely models V1314, with $Z = 0.001$, which predict O enrichment for stars with initial masses, at the ZAMS, equal

or larger than 1.5 $M_{\odot}$. However V1314 models predict very low N/O abundance ratios for stars with masses between 1.5 and 2.5 $M_{\odot}$. N enrichment in V1314 models occurs only for stellar masses larger than 2.5 $M_{\odot}$. According to these models, our PNe would have had initial masses larger than 2.5 $M_{\odot}$ and the progenitor of our Type I PN (PN13) would have had initial mass of about 3.5 $M_{\odot}$. Models V14, with metallicity $Z = 0.004$, show O abundances that are too large compared to our objects.

Hence, regarding N/O abundance ratios, all the model sequences analyzed here seem inadequate as compared with our data.

4.3. Ne/O abundance ratios

Values of Ne/H versus O/H abundances for PNe and H II regions are presented in Fig. 7. It is interesting to note that PN17 shows the lowest O and Ne abundances, similar to the values of H II regions, while all the other PNe present higher O and Ne abundances.

A tight correlation is found between Ne and O abundances similar to that found in all other sample of PNe and H II regions (Henry 1989; García-Hernández & Górny 2014; García-Rojas et al. 2016). The linear fit for PNe is $12 + \log(\mathrm{Ne/H}) = (1.74 \pm 0.49) \times (12 + \log(\mathrm{O/H})) - (6.60 \pm 4.05)$, with $R^2 = 0.70$. Thus, we have found that O is enriched in our PN sample, but given the slope of 1.74 in the log Ne/H versus log O/H diagram, Ne is even more enriched. This is a very important result that supports the chemical evolution models predicting large Ne enhancements for stars with very low metallicity and initial masses between 1.5 and 4 $M_{\odot}$ (Karakas & Lattanzio 2003).

In the left panel of Fig. 7, we present the predictions of stellar evolution models by K10 and F14 for $Z = 0.0001$, 0.001, and 0.004. As in Fig. 6, some ZAMS initial masses have been tagged in each sequence of metallicity. All the models predict large Ne increments, although they do not predict large O enrichment. Such large Ne increments occur for stars with initial masses between 1.5 and 4 $M_{\odot}$, depending on Z. Ne increments are mainly due to the enrichment of the ^{22}Ne isotope. In these models the usually most abundant isotope, ^{20}Ne, is not significantly modified by nucleosynthesis, but during the AGB phase; the ^{22}Ne abundance highly increases by means of two α-capture of ^{14}N, which transforms it into ^{22}Ne. Such a recently produced ^{22}Ne could be brought to the surface during third dredge-up events, increasing the total Ne abundance (Karakas & Lattanzio 2003).

In the models, stars with higher masses are less efficient in Ne enrichment because ^{22}Ne diminishes as a consequence of an α capture that destroys it; thus, in Fig. 7, the evolution traces at a given metallicity are bent over themselves.

In the left panel Fig. 7, several of our PNe lie near the models with $Z = 0.004$ which again is in disagreement with the metallicity in NGC 3109. Besides that, Ne in PN3, PN9, and PN13 is better reproduced by $Z = 0.001$ models, although O is not, and no model reproduces the low Ne abundance shown by PN17. Models with $Z = 0.001$ predict that the initial masses of the PN central stars would have been in the range from 1 to 4.0 $M_{\odot}$, while models with $Z = 0.004$ indicate that the initial masses were in the range from 1 to 2.5 $M_{\odot}$. PN4 has the largest Ne abundance and, according to $Z = 0.004$ models, its initial mass was about 2.0−2.5 $M_{\odot}$.

In the right panel of Fig. 7, we explore the Ne/H versus O/H behavior predicted by models by V1314 for $Z = 0.001$ and V14 for $Z = 0.004$. Our objects lie near models with $Z = 0.001$. The observed Ne abundances are consistent with models for progenitors with initial masses of 1.25−3.5 $M_{\odot}$, but again no model predicts the low Ne found in PN17. In comparison with V1314 models, our Peimbert Type I PN13 would have had an initial mass of 3 $M_{\odot}$ while the extreme Ne-rich PN4 would have had an initial mass of about 2−2.5 $M_{\odot}$.

In conclusion, regarding the Ne/H versus O/H behavior, we find that V1314 models ($Z = 0.001$) agree better with our data, except for PN17, while F14 models ($Z = 0.001$) do not reproduce our PN data, as they predict too large Ne enrichment and too low O enrichment.

4.4. S and Ar abundances

Ar/H and S/H versus O/H abundances, for PNe and H II regions, are presented in Fig. 8 (left and right panels). In this graphs there are only a very few PNe with Ar and S abundance determinations and the uncertainties are large. No correlation with O is found for these α elements. Given the uncertainties, it is apparent that Ar and S abundances in PNe are similar to the abundances in H II regions.

Therefore, as expected, S and Ar are not enriched in PNe, and their values seems to correspond to a relatively young PN population.

4.5. Abundances in H II regions and chemical gradients

In Table 7 the chemical abundances for 11 H II regions, spreading over the entire region covered by the stars in the galaxy, are presented. It is evident that these young nebulae have remarkable uniform abundances, with an average 12 + log O/H of 7.74 ± 0.09; the lower limit for H II 4 was not considered. Therefore we can conclude that the ISM, in the central 5 kpc of this galaxy is chemically homogeneous. This homogeneity of the ISM is consistent with similar results in other irregular galaxies like the Magellanic Clouds (Pagel et al. 1978; Dufour 1984), NGC 6822 (Hernández-Martínez et al. 2009) and others. Considering all these examples, a nearly constant O abundance is expected for irregular galaxies, and this is found over the optical extension of NGC 3109. To illustrate this fact, we present Fig. 9 where O abundances for H II regions and PNe are shown versus distance to the galactic center. No gradient is appreciated in HII regions, nor in PNe, from the center up to a radius of 2.5 kpc.

5. Is there a relation between the kinematics and chemistry in NGC 3109?

As it described above and shown in Fig. 9, there is no chemical gradient for H II regions in NGC 3109. PNe show no gradient either, but this is expected as the central stars modified their original O abundance. A chemical gradient was not found by Evans et al. (2007) and Hosek et al. (2014) either in their analysis of the chemistry of supergiant stars.

Therefore all the material in the bar of the galaxy, which is rotating with a velocity gradient of about 17 km s^{-1} per kpc, seems well mixed (possibly due to the action of the bar). This material includes the presence of a very young population represented by H II regions, which is a slightly older population represented by the supergiant stars and an intermediate-age population represented by the PNe. The latter two are distributed in a thicker zone than the H II regions.

As mentioned before, the lack of chemical gradients is usually found in irregular galaxies where different populations,

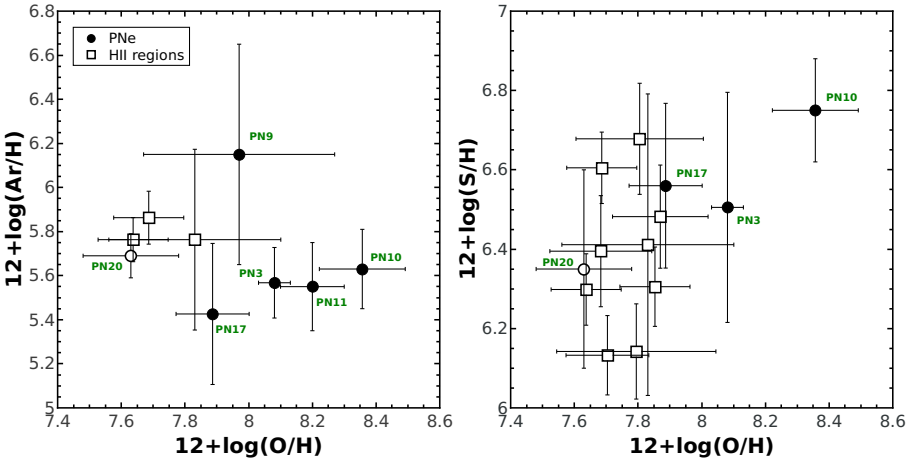

Fig. 8. 12 + log(Ar/H) versus 12 + log(O/H) and 12 + log S/H versus 12 + log(O/H) for PNe (dots), and H II regions (open squares).

often with different kinematics, are frequently found. This absence of a chemical gradient in irregular galaxies is contrary to what occurs in large spiral galaxies like the Milky Way, Andromeda, M 81, NGC 300, and others, where abundance gradients are clearly detected (Stasińska et al. 2013; Stanghellini et al. 2014, 2015; Magrini et al. 2016). The same authors have discussed the behavior of chemical gradients of H II regions in comparison with the gradients presented by PNe, finding that the latter are flatter than those presented by H II regions. They have attributed such a phenomenon to possible migration of PNe along the galactic disks.

It is interesting to mention here the situation in dwarf spheroidal (dSph) galaxies of the Local Group. Galaxies such as Fornax, Sculptor, Carina and Sextans have been analyzed and all of them display evidence for the coexistence of two or more populations with different metallicities (metal poor and metal rich), different spatial distribution, and different velocity dispersion profiles (see Zhu et al. 2016, and references therein). Chemodynamical models for some of these galaxies reveal that the dSphs have undergone different episodes of star formation in the past, the youngest of which gave origin to a richer population that is more centrally concentrated.

In NGC 3109 we are witnessing different episodes of star formation. Previous episodes generated the C-stars, PN central stars, and BSG stars, and the present episodes has generated OB stars ionizing H II regions. These populations (PNe, BSGs, and H II regions) apparently show slightly different dynamics (see Fig. 5) but not chemical gradients. In the irregular galaxy NGC 6822 different populations have also been found and in this case these populations do show different dynamics and different chemical composition, although no chemical gradients (Hernández-Martínez et al. 2009; Flores-Durán et al. 2014; García-Rojas et al. 2016).

Thus, it can be inferred that dwarf galaxies (spheroidals and irregulars) display in general complex structures that have several populations with different metallicities and dynamics. However no chemical gradients are evident in them. In the case of NGC 3109 deeper studies are needed to analyze the faint (presumable) old population to verify its metallicity and kinematics.

6. General conclusions

We study the kinematics of eight confirmed PNe and several H II regions that are distributed all over the entire region covered

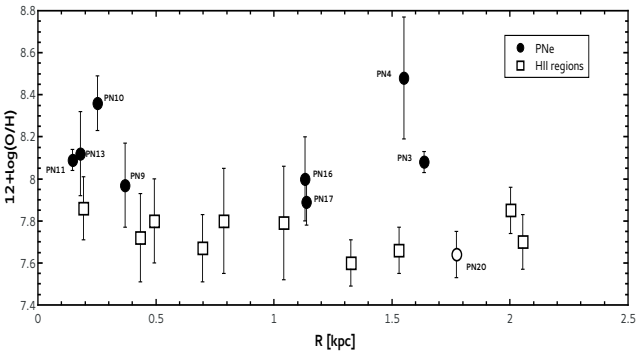

Fig. 9. O abundances of H II regions and PNe versus distance to the galactic center.

by stars in NGC 3109 using high spectral-resolution data obtained at OAN-SPM and LCO. The analyzed PNe represent more than 40% of the total sample of PN candidates known for this galaxy.

The kinematics of all these objects was analyzed in comparison with the kinematics of the huge H I disk that surrounds this galaxy. In addition, the kinematics of the blue supergiant stars (BSGs) of NGC 3109, as presented by Evans et al. (2007), was included in the analysis.

Our results show that H II regions share the H I gas kinematics with a dispersion velocity that is lower than 8.6 km s^{-1}. This is in agreement with the analysis of the ionized gas made by Blais-Ouellette et al. (2003). The rotation curve of these elements corresponds to that of a bar in the central zone of the galaxy. On the other hand, PNe and BSGs, even when they rotate in the same direction, show a very large dispersion in velocities. These objects could be even rotating with a slightly steeper rotation curve, although the low dispersion of data of BSGs prevents us from a conclusive result. This probable difference in kinematics, together with the fact that the distribution of PNe and BSGs corresponds to a thicker zone than the distribution of H II regions, indicates that these young and intermediate-age objects (BSGs and PNe) belong to different populations.

Using our observations with MIKE at LCO and the line intensities reported by Peña et al. (2007b), physical conditions and chemical abundances for the PNe were calculated using Delgado-Inglada et al. (2014) ICFs. No big differences in

abundances for O, N, and Ne were found using K&B94 or Delgado-Inglada et al. (2014) ICFs. Therefore in the cases where ICFs by Delgado-Inglada et al. (2014) cannot be used for these elements, we employed K&B ICFs. Chemical abundances in H II regions were also derived using K&B ICFs.

Our results reinforce that in NGC 3109, PNe are O enriched, relative to the H II regions, by an amount in average of 0.41 dex. This is important evidence that supports predictions of some stellar evolution models for low-intermediate mass stars, which indicate O enrichment at very low metallicity. It is worth mentioning that this is not the case in the more enriched galaxy NGC 6822, where PNe show O/H abundances in a large range, some being O richer and some O poorer than H II regions (García-Rojas et al. 2016).

In addition to O enrichment, we found that all but one of the observed PNe in NGC 3109 show Ne enrichment; this is in agreement with predictions of stellar evolution models, where total Ne is enriched via ^{22}Ne. This isotope can be nucleosynthesized through two α-capture of ^{14}N and brought to the surface by a third dredge-up episode in low-metallicity stars of ZAMS initial masses of 2−4 $M_{\odot}$.

We compare our data with models by Karakas (2010), Fishlock et al. (2014), and nonstandard models by Ventura et al. (2013, 2014a,b) for different metallicities. It is found that the best agreement, for O and Ne abundances happens, concerning nonstandard models by Ventura et al. (2013, 2014a) at Z = 0.001, because at the metallicity of NGC 3109 ($Z \sim 0.0015$) models by Karakas (2010) and Fishlock et al. (2014) predict very low O enrichment and excess of Ne enrichment. A similar result was found for NGC 6822, where García-Rojas et al. (2016) found that Karakas (2010) models predicted excess of Ne in comparison with observations while models by Ventura agree better with data.

All the analyzed PNe present N enrichment. From the comparison of the PN N/O abundance ratios with the stellar evolution models cited above, it is found that the models fail in different ways. Karakas (2010) and Fishlock et al. (2014) models predict too much N/O (probably because they do not predict O enrichment) while Ventura et al. (2013, 2014a,b) models predict too low N/O values for stars with masses between 1.5 and 2.5 $M_{\odot}$. Therefore regarding N/O abundance ratios, the models analyzed here are inadequate. In order to build better models to reproduce PN observations it would be necessary to improve the yields for N. For the case of Ne, the inclusion of nonstandard effects like those by Ventura et al. (2013, 2014a,b) models helps to reproduce better the observational data.

Sulfur and argon were determined in a few PNe of our sample, which show abundances similar to the values in H II regions in NGC 3109. That is, contrary to N, O, and Ne, these two α elements show the original values at the moment of formation of the PN central stars. They could therefore be used instead of oxygen or neon as good tracers of chemical evolution with time.

One PN (PN17) in our sample has a very low Ne abundance. No evolution model predicts such a low Ne abundance at the metallicity of NGC 3109. This PN does not show large O enrichment either, therefore, it seems possible that such an object belongs to an older PN population or has a progenitor with an initial mass of about 1 $M_{\odot}$.

As derived from the spectroscopy, the PN candidate PN20 presented by Peña et al. (2007a) resulted to be a H II region and it was reclassified.

The abundances in H II regions were analyzed searching for a possible abundance gradient in the central zone of NGC 3109. No abundance gradient was found neither in NGC 3109 nor in the supergiants stars analyzed by Evans et al. (2007) and Hosek et al. (2014). Therefore, even when NGC 3109 presents several different populations showing different chemistry and possibly different kinematics, no chemical gradient is found; this is similar to what occurs in other irregular galaxies of the Local Group, where very different populations exist (stellar clusters, old and young stars, H II regions, etc.) showing different kinematics, but no evidence for a chemical gradient is found.

As a result of this work we find that the predicted O, N, and Ne enrichment in PNe should be analyzed more deeply in stellar evolution models. The different models explored here agree in some aspects with the results of observations and disagree in others. In particular O enrichment should be reconsidered because some PNe in the solar vicinity, with carbon-rich dust, have shown such an O enrichment, by about 0.3 dex, compared to the H II regions in the same vicinity (Delgado-Inglada et al. 2015).

Acknowledgements. This work received financial support from DGAPA-PAPIIT (UNAM) grant IN109614. We thank the daytime and night support staff, G. Melgoza, F. Montalvo, and S. Monrroy at the OAN-SPM for facilitating and helping to obtain our observations. S.N.F.-D. received scholarship from CONACyT-México. We thank the referee for her/his comments. We are very grateful to Dr. P. Ventura for providing the tables with the surface abundances of his AGB models. We are grateful to Dr. A. Karakas for providing detailed numbers of the models by Fishlock et al. (2014). We are grateful to Dr. J. García-Rojas for the support provided. Very valuable comments by Dr. B. Pichardo and Prof. C. Carignan are deeply acknowledged.

References

Asplund, M., Grevesse, N., & Sauval, A. J. 2005, in Cosmic Abundances as Records of Stellar Evolution and Nucleosynthesis, eds. T. G. Barnes, III, & F. N. Bash, ASP Conf. Ser., 336, 25
Barnes, D. G., & de Blok, W. J. G. 2001, AJ, 122, 825
Berstein, R. A., Shectman, S. A., Gunnels, S., Mochnacki, S., & Athey, A. 2002, Proc. SPIE, 4841, 1694
Blais-Ouellette, S., Amram, P., & Carignan, C. 2003, ApJ, 121, 1952
Bresolin, F., Capaccioli, M., & Piotto, G. 1993, AJ, 105, 1779
Carignan, C., Frank, B. S., Hess, K. M., et al. 2013, AJ, 146, 48
Coccato, L., Gerhard, O., Arnaboldi, M., et al. 2009, MNRAS, 394, 1249
Cortesi, A., Arnaboldi, M., Coccato, L., et al. 2013, A&A, 549, A115
de Vaucouleurs, G., de Vaucouleurs, A., Corwin, H. G., et al. 1991, Third Reference Catalogue of Bright Galaxies (Berlin, Heidelberg, New York: Springer-Verlag)
Debattista, V. P., & Sellwood, J. A. 2000, ApJ, 543, 704
Delgado-Inglada, G., Morisset, C. & Stasińska, G. 2014, MNRAS, 440, 536
Delgado-Inglada, G., Rodríguez, M., Peimbert, M., Stasińska, G. & Morisset, C. 2015, MNRAS, 449, 1797
Demers, S., Battinelli, P. & Letarte, B. 2003, A&A, 410, 795
Dufour, R. J. 1984, in Structure and evolution of the Magellanic Clouds, IAU Symp., 108, 353
Evans, C. J., Bresolin, F., Urbaneja, M. A., Pietrzyński, G., & Gieren, W. 2007, ApJ, 659, 1198
Fishlock, C. K., Karakas, A. I., Lugaro, M., & Yong, D. 2014, ApJ, 797, 44
Flores-Durán, S. N., Peña, M., Hernández-Martínez, L., et al. 2014, A&A, 568, A82
García-Hernández, D. A., & Górny, S. K. 2014, A&A, 567, A12
García-Rojas, J., Peña, M., Flores-Durán, S., & Hernández-Martínez, L. 2016, A&A, 586, A59
Gonçalves, D. R., Teodorescu, A. M., Alves-Brito, A., Méndez, R. H., & Magrini, L. 2012, MNRAS, 425, 2557
Henry, R. B. C. 1989, MNRAS, 241, 453
Herrmann, K., & Ciardullo, R. 2009, ApJ, 705, 1686
Hernández-Martínez, L., Peña, M., Carigi, L., & García-Rojas, J. 2009, A&A, 505, 102
Hodge, P. W. 1969, ApJS, 18, 73
Hosek Jr., M. W., Kudritzki, R.-P., Bresolin, F., et al. 2014, ApJ, 785, 151
Jobin, M., & Carignan, C. 1990, AJ, 100, 3
Karakas, A. I. 2010, MNRAS, 403, 1413
Karakas, A. I., & Lattanzio, J. C. 2003, Publ. Astron. Soc. Aust., 20, 393
Kingsburg, R. L., & Barlow, M. J. 1994, MNRAS, 271, 257
Longobardi, A., Arnaboldi, M., Gerhard, O., et al. 2013, A&A, 558, A42

Magrini, L., Coccato, L., Stanghellini, L., Casasola, V., & Galli, D. 2016, A&A, 588, A91
Marigo, P. 2001, A&A, 370, 194
McConnachie, A. W. 2012, AJ, 144, 4
Meaburn, J., Blundell, B., Carling, R., et al. 1984, MNRAS, 210, 463
Meaburn, J., López, J. A., Gutiérez, L., et al. 2003, Rev. Mex. Astron. Astrofis., 39, 185
Merrett, H. R., Merrifield, M. R., Douglas, N. G., et al. 2006, MNRAS, 369, 120
Minniti, D., Zijlstra, A. A., & Alonso. V. M. 1999, AJ, 117, 881
Ott, J., Stilp, A. M., Warren, S. R., et al. 2012, AJ, 144, 123
Pagel, B. E. J., Edmunds, M. G., Fosbury, R. A. E., & Webster B. L. 1978, MNRAS, 184, 569
Peña, M., Richer, M. G, & Stasińska, G. 2007a, A&A, 466, 75
Peña, M., Stasińska, G., & Richer, M. G. 2007b, A&A, 476, 745
Richer, M. G., & McCall, M. L. 1992, AJ, 103, 54
Richer, M. G., López, J. A., Díaz-Méndez, E., et al. 2010, Rev. Mex. Astron. Astrofis., 46, 191
Seaton, M. 1979, MNRAS, 187, 73
Soszyński, I., Gieren, W., Pietrztyński, G., et al. 2006, ApJ, 648, 375
Stanghellini, L., Magrini, L., Casasola, V., & Villaver, E. 2014, A&A, 567, A88
Stanghellini, L., Magrini, L., & Casasola, V. 2015, ApJ, 812, 39
Stasińska, G., Peña, M., Bresolin, F., & Tsamis, Y. G. 2013, A&A, 552, A12
Storey, P. J., & Hummer, D. G. 1995, MNRAS, 272, 41
Valenzuela, O., Rhee, G., Anatoly, K., et al. 2007, ApJ, 657, 773
Ventura, P., Di Criscienzo, M., Carini, R., & D'Antona, F. 2013, MNRAS, 431, 3642
Ventura, P., Di Criscienzo, M., D'Antona, F., et al. 2014a, MNRAS, 437, 3274
Ventura, P., Dell'Agli, F., Schneider, R., et al. 2014b, MNRAS, 439, 977
Weinberg, M. D. 1985, MNRAS, 213, 451
Zhu, L., van de Ven, G., Watkins, L. l., & Posti, L. 2016, MNRAS, 463, 1117

5

Conclusiones

Estudiamos la cinemática y la química de varias NPs y regiones H II distribuidas a lo largo de todo el cuerpo óptico de dos galaxias Irregulares del grupo local, NGC 6822 y NGC 3109. En términos generales los resultados más importantes obtenidos son:

A partir del uso de datos espectroscópicos de alta resolución nos fue posible comparar el comportamiento cinemático de diez NPs (∼40 % del total de NPs conocidas en esta galaxia) y cuatro regiones H II con el disco de H I y el esferoide estelar presentes en NGC 6822. A este análisis se agregaron dos estrellas supergigantes tipo A, representantes de la población joven. Encontramos que la cinemática de las NPs no corresponde a la cinemática del disco de H I, estos objetos se mueven como el elipsoide de estrellas de C, de edad intermedia. Mientras que los objetos jóvenes, es decir, las regiones H II (H V, H X y H II 15) y las estrellas supergigantes tipo A sí presentan un comportamiento cinemático similar al del disco de H I.

Debido a sus velocidades sistémicas las NPs parecen formar parte del esferoide estelar de edad intermedia que posee NGC 6822. Sin embargo la velocidad promedio de las NPs es -57.8 km s^{-1}, por lo que comparte la velocidad sistemica de la galaxia. Por otro lado el esferoide estelar tiene una velocidad promedio de -32.9 km s^{-1} y los cúmulos estelares reportados por Hwang et al. (2014) tienen una velocidad promedio de -88.3 km s^{-1}. De esto, NGC 6822 parece tener diferentes sistemas cinemáticos, uno compuesto por la población joven y el gas H I y el otro con objetos de edad intermedia-vieja.

A partir de datos espectrofotométricos obtenidos con los telescopios GTC, VLT y CFH, se calcularon las condiciones físicas y las abundancias químicas de 19 NPs pertenecientes a NGC 6822 (esto es ∼84 % del total de NPs). Además se incluyeron las abundancias químicas de cuatro regiones H II para compararlas con las abundancias de las NPs. Las NPs presentan composiciones químicas variadas, desde objetos pobres, 12+log O/H = 7.4 hasta objetos con abundancias similares a la población de regiones H II en la galaxia (12+log O/H = 7.8).

La comparación de los modelos de Karakas (2010) y Fishlock et al. (2014) con las abundancias observadas nos da resultados discrepantes sobre las masas iniciales de las progenitoras de las NPs en NGC 6822. Por ejemplo, el cociente de abundancia N/O sugiere masas iniciales menores que 4 $M_\odot$ mientras que la abundancia del Ne/H indica

masas iniciales menores a 2 M⊙. Además en esta galaxia los modelos para estrellas de 2-3M⊙ Karakas (2010) y Fishlock et al. (2014) producen demasiado ^{22}Ne, por lo que fallan en reproducir el Ne/H de las NPs. En el caso de los modelos de Ventura et al. (2013, 2014,?) se observa una mejor concordancia en las masas iniciales que predicen los cocientes de N/O y Ne/H siempre que las estrellas más masivas estén cerca de 4 M⊙.

Obtuvimos datos de alta resolución en OAN-SPM y en LCO de ocho NPs (equivalentes al 40 % de las NPs conocidas) y varias regiones H II pertenecientes a NGC 3109, con estos datos fue posible realizar la comparación de su comportamiento cinemático con el del disco de H I. Además agregamos a la muestra datos cinemáticos de baja resolución de la literatura (Evans et al. 2007) para estrellas supergigantes azules de NGC 3109. Encontramos que las regiones H II comparten la cinemática del disco de H I con una dispersión menor que 8.6 km s^{-1}. Por otro lado las NPs y las estrellas supergigantes azules, rotan en la misma dirección que el disco de H I pero con una dispersión de velocidades mucho mayor.

De las observaciones obtenidas con MIKE en LCO y de los datos reportados por Peña et al. (2007), Peña et al. (2007b), calculamos las condiciones físicas y las abundancias químicas utilizando los ICFs de Delgado-Inglada et al. (2014). Confirmamos que en NGC 3109, las NPs están enriquecidas en O en comparación con las regiones H II, por una cantidad en promedio de 0.43 dex. Este resultado es una evidencia importante que apoya la predicción de algunos modelos de evolución estelar (por ejemplo, Marigo (2001)) de estrellas con masas iniciales menores que ∼3.5 M$_\odot$ enriquecen el O. Además encontramos que a excepción de una NP, las NPs están enriquecidas también en Ne, **con un valor promedio de 12+log(Ne/H) = 7.27 ± 0.30 mientras que para las regiones H II la abundancia de Ne es 12+log(Ne/H) = 6.80 ± 0.13.**

La PN20 es una nebulosa de baja excitación donde la abundancia de O^{2+} es menor que la de O^+ y su abundancia total es 12+log(O/H) = 7.64 ± 0.15. Dadas sus características espectrales y de abundancia fue clasificada como una región H II.

En NGC 3109 también comparamos nuestros datos observacionales con los modelos de Karakas (2010) y Fishlock et al. (2014). En este caso los modelos fallan en reproducir el enriquecimiento de O y predicen en exceso el enriquecimiento de Ne. Los modelos

de Ventura et al. (2013, 2014,?) para $Z = 0{,}001$ estan en mejor concordancia con las abundancias de O y Ne de las NPs.

Estas galaxias son bastante peculiares y con diferencias interesantes entre si. En el caso de NGC 6822 encontramos evidencia de que la población de edad intermedia-vieja (NPs, estrellas de carbono) forma un sistema cinemático distinto al de la población joven (regiones H II, estrellas azules supergigantes). Entonces, esta galaxia está compuesta por más de un sistema dinámico y su química es muy homogénea en la parte central y no presenta evidencia de que las estrellas de masa baja a intermedia enriquezcan el O. Por otro lado NGC 3109 presenta un comportamiento cinemático muy similar entre su población joven y de edad intermedia-vieja, ambos siguen de cerca al disco de H I. En el caso de la química de las NPs, encontramos que el O y el Ne están siendo enriquecidos en un ambiente de baja metalicidad.

Del análisis cinemático de las NPs de ambas galaxias encontramos que presentan rotación de cuerpo rígido en su centro, lo cual indica estas galaxias poseen una barra. Las poblaciones estelares jóvenes presentan una menor dispersión de velocidades que la población de edad intermedia-vieja.

Los modelos de Karakas (2010) y Fishlock et al. (2014) fallan en reproducir el Ne/H de NGC 6822 y en NGC 3109, y predicen mucho N/O, probablemente porque no predicen el enriquecimiento del O. Los modelos de Ventura et al. (2013, 2014,?) reproducen mejor la abundancia del O y Ne en NPs. Pero predicen poco N/O para estrellas entre 1.5-2.5 $M_{\odot}$.

Bibliografía

Hubble, E. P. (1925). NGC 6822, a remote stellar system. *ApJ*, 62.

Baade, W. (1955). Planetary nebulae in M 31. *AJ*, 60:151.

Hodge, P. W. (1977). The structure and content of NGC 6822. *ApJS*, 33:69–82.

Iben, Jr., I. & Renzini, A. (1983). Asymptotic giant branch evolution and beyond. *ARA&A*, 21:271–342.

Demers, S., Irwin, M. J., & Kunkel, W. E. (1985). Automated photometry of NGC 3109. *AJ*, 90:1967–1981.

Nolthenius, R. & Ford, H. (1986). The mass and halo dispersion profile of M32. *ApJ*, 305:600–608.

Dennefeld, M. (1989). Abundances Derived from Gaseous Nebulae in the Magellanic Clouds. In de Boer, K. S., Spite, F., & Stasińska, G., editors, *Recent Developments of Magellanic Cloud Research*, page 107.

de Vaucouleurs, G., de Vaucouleurs, A., Corwin, Jr., H. G., Buta, R. J., Paturel, G., & Fouqué, P. (1991). *Third Reference Catalogue of Bright Galaxies. Volume I: Explanations and references. Volume II: Data for galaxies between 0^h and 12^h. Volume III: Data for galaxies between 12^h and 24^h.*

Dopita, M. A., Vassiliadis, E., Wood, P. R., Meatheringham, S. J., Harrington, J. P., Bohlin, R. C., Ford, H. C., Stecher, T. P., & Maran, S. P. (1997). Hubble Space

Telescope Observations of Planetary Nebulae in the Magellanic Clouds. V. Mass Dependence of Dredge-up and the Chemical History of the Large Magellanic Cloud. *ApJ*, 474:188–204.

Allen, C., Carigi, L., & Peimbert, M. (1998). Chemodynamical Model of the Galaxy: Abundance Gradients Predicted for H II Regions and Planetary Nebulae. *ApJ*, 494:247–255.

Mateo, M. L. (1998). Dwarf Galaxies of the Local Group. *ARA&A*, 36:435–506.

Stasińska, G., Richer, M. G., & McCall, M. L. (1998). The planetary nebulae populations in five galaxies: abundance patterns and evolution. *A&A*, 336:667–681.

Garnett, D. R. (1999). Element Abundances in Magellanic Cloud H II Regions from Carbon to Argon. In Chu, Y.-H., Suntzeff, N., Hesser, J., & Bohlender, D., editors, *New Views of the Magellanic Clouds*, volume 190 of *IAU Symposium*, page 266.

Minniti, D., Zijlstra, A. A., & Alonso, M. V. (1999). The Stellar Populations of NGC 3109: Another Dwarf Irregular Galaxy with a Population II Stellar Halo. *AJ*, 117:881–893.

Muschielok, B., Kudritzki, R. P., Appenzeller, I., Bresolin, F., Butler, K., Gässler, W., Häfner, R., Hess, H. J., Hummel, W., Lennon, D. J., Mantel, K.-H., Meisl, W., Seifert, W., Smartt, S. J., Szeifert, T., & Tarantik, K. (1999). VLT FORS spectra of blue supergiants in the Local Group galaxy NGC 6822. *A&A*, 352:L40–L44.

de Blok, W. J. G. & Walter, F. (2000). Evidence for Tidal Interaction and a Supergiant H I Shell in the Local Group Dwarf Galaxy NGC 6822. *ApJ*, 537:L95–L98.

Kwok, S. (2000). *The Origin and Evolution of Planetary Nebulae*.

Marigo, P. (2001). Chemical yields from low- and intermediate-mass stars: Model predictions and basic observational constraints. *A&A*, 370:194–217.

Venn, K. A., Lennon, D. J., Kaufer, A., McCarthy, J. K., Przybilla, N., Kudritzki, R. P., Lemke, M., Skillman, E. D., & Smartt, S. J. (2001). First Stellar Abundances in NGC 6822 from VLT-UVES and Keck-HIRES Spectroscopy. *ApJ*, 547:765–776.

Barnes, D. G. & de Blok, W. J. G. (2001). On the Neutral Gas Content and Environment of NGC 3109 and the Antlia Dwarf Galaxy. *AJ*, 122:825–829.

Olsen, K. A. G. & Salyk, C. (2002). A Warp in the Large Magellanic Cloud Disk? *AJ*, 124:2045–2053.

Ciardullo, R., Feldmeier, J. J., Jacoby, G. H., Kuzio de Naray, R., Laychak, M. B., & Durrell, P. R. (2002). Planetary Nebulae as Standard Candles. XII. Connecting the Population I and Population II Distance Scales. *ApJ*, 577:31–50.

Letarte, B., Demers, S., Battinelli, P., & Kunkel, W. E. (2002). The Extent of NGC 6822 Revealed by Its C Star Population. *AJ*, 123:832–839.

Weldrake, D. T. F., de Blok, W. J. G., & Walter, F. (2003). A high-resolution rotation curve of NGC 6822: a test-case for cold dark matter. *MNRAS*, 340:12–28.

Karakas, A. I. & Lattanzio, J. C. (2003). AGB Stars and the Observed Abundance of Neon in Planetary Nebulae. *PASA*, 20:393–400.

Karttunen, H., Kroeger, P., Oja, H., Poutanen, M., & Donner, K. J. (2003). *Fundamental astronomy*.

Koribalski, B. S., Staveley-Smith, L., Kilborn, V. A., Ryder, S. D., Kraan-Korteweg, R. C., Ryan-Weber, E. V., Ekers, R. D., Jerjen, H., Henning, P. A., Putman, M. E., Zwaan, M. A., de Blok, W. J. G., Calabretta, M. R., Disney, M. J., Minchin, R. F., Bhathal, R., Boyce, P. J., Drinkwater, M. J., Freeman, K. C., Gibson, B. K., Green, A. J., Haynes, R. F., Juraszek, S., Kesteven, M. J., Knezek, P. M., Mader, S., Marquarding, M., Meyer, M., Mould, J. R., Oosterloo, T., O'Brien, J., Price, R. M., Sadler, E. M., Schröder, A., Stewart, I. M., Stootman, F., Waugh, M., Warren, B. E., Webster, R. L., & Wright, A. E. (2004). The 1000 Brightest HIPASS Galaxies: H I Properties. *AJ*, 128:16–46.

Demers, S., Battinelli, P., & Kunkel, W. E. (2006). A Local Group Polar Ring Galaxy: NGC 6822. *ApJ*, 636:L85–L88.

Reid, W. A. & Parker, Q. A. (2006). A new population of planetary nebulae discovered in the Large Magellanic Cloud - II. Complete PN catalogue. *MNRAS*, 373:521–550.

Osterbrock, D. E. & Ferland, G. J. (2006). *Astrophysics of gaseous nebulae and active galactic nuclei*.

Salaris, M. & Cassisi, S. (2006). *Evolution of Stars and Stellar Populations*.

Battinelli, P., Demers, S., & Kunkel, W. E. (2006). Photometric survey of the polar ring galaxy NGC 6822. *A&A*, 451:99–108.

Soszyński, I., Gieren, W., Pietrzyński, G., Bresolin, F., Kudritzki, R.-P., & Storm, J. (2006). The Araucaria Project: Distance to the Local Group Galaxy NGC 3109 from Near-Infrared Photometry of Cepheids. *ApJ*, 648:375–382.

Corradi, R. L. M. & Magrini, L. (2006). The Census of Planetary Nebulae in the Local Group. In Stanghellini, L., Walsh, J. R., & Douglas, N. G., editors, *Planetary Nebulae Beyond the Milky Way*, page 36.

de Blok, W. J. G. & Walter, F. (2006). The Stellar Population and Interstellar Medium in NGC 6822. *AJ*, 131:343–362.

Peña, M., Richer, M. G., & Stasińska, G. (2007). A catalog of planetary nebula candidates and HII regions in NGC 3109. *A&A*, 466:75–82.

Carroll, B. & Ostlie, D. (2007). *An Introduction to Modern Astrophysics*. Pearson international edition. Pearson Addison-Wesley.

Evans, C. J., Bresolin, F., Urbaneja, M. A., Pietrzyński, G., Gieren, W., & Kudritzki, R.-P. (2007). The ARAUCARIA Project: VLT-FORS Spectroscopy of Blue Supergiants in NGC 3109-Classifications, First Abundances, and Kinematics. *ApJ*, 659:1198–1211.

Peña, M., Stasińska, G., & Richer, M. G. (2007). The chemical composition of planetary nebulae and HII regions in NGC 3109. *A&A*, 476:745–758.

Gerhard, O., Arnaboldi, M., Freeman, K. C., Okamura, S., Kashikawa, N., & Yasuda, N. (2007). The kinematics of intracluster planetary nebulae and the on-going subcluster merger in the Coma cluster core. *A&A*, 468:815–822.

Richer, M. G. & McCall, M. L. (2007). The Progenitors of Planetary Nebulae in Dwarf Irregular Galaxies. *ApJ*, 658:328–336.

Ventimiglia, G., Arnaboldi, M., & Gerhard, O. (2008). Intracluster Planetary Nebulae in the Hydra I cluster. *Astronomische Nachrichten*, 329:1057.

Hernández-Martínez, L., Peña, M., Carigi, L., & García-Rojas, J. (2009). Chemical behavior of the dwarf irregular galaxy NGC6822. Its PN and HII region abundances. *A&A*, 505:1027–1039.

Hernández-Martínez, L. & Peña, M. (2009). Emission line objects in NGC 6822. New planetary nebula candidates. *A&A*, 495:447–455.

Herrmann, K. A., Ciardullo, R., & Sigurdsson, S. (2009). Kinematic Evidence for Halo Substructure in Spiral Galaxies. *ApJ*, 693:L19–L22.

Coccato, L., Gerhard, O., Arnaboldi, M., Das, P., Douglas, N. G., Kuijken, K., Merrifield, M. R., Napolitano, N. R., Noordermeer, E., Romanowsky, A. J., Capaccioli, M., Cortesi, A., De Lorenzi, F., & Freeman, K. C. (2009). Kinematic properties of early-type galaxy haloes using planetary nebulae*. *MNRAS*, 394:1249–1283.

Méndez, R. H., Teodorescu, A. M., Kudritzki, R.-P., & Burkert, A. (2009). Kinematics of Planetary Nebulae in the Outskirts of the Elliptical Galaxy NGC 4697. *ApJ*, 691:228–240.

Schönberner, D., Jacob, R., Sandin, C., & Steffen, M. (2010). The evolution of planetary nebulae. VII. Modelling planetary nebulae of distant stellar systems. *A&A*, 523:A86.

Richer, M. G., López, J. A., Díaz-Méndez, E., Riesgo, H., Báez, S.-H., García-Díaz, M. T., Meaburn, J., Clark, D. M., Calderón Olvera, R. M., López Soto, G., & Toledano Rebolo, O. (2010). The San Pedro Mártir Planetary Nebula Kinematic Catalogue: Extragalactic Planetary Nebulae. *Rev. Mexicana Astron. Astrofis.*, 46:191–214.

Karakas, A. I. (2010). Updated stellar yields from asymptotic giant branch models. *MNRAS*, 403:1413–1425.

Teodorescu, A. M., Méndez, R. H., Bernardi, F., Thomas, J., Das, P., & Gerhard, O. (2011). Planetary Nebulae in the Elliptical Galaxy NGC 4649 (M 60): Kinematics and Distance Redetermination. *ApJ*, 736:65.

Hernández-Martínez, L., Carigi, L., Peña, M., & Peimbert, M. (2011). PNe as observational constraints in chemical evolution models for NGC 6822. In *Revista Mexicana de Astronomia y Astrofisica Conference Series*, volume 40 of *Revista Mexicana de Astronomia y Astrofisica Conference Series*, pages 171–172.

Ventimiglia, G., Arnaboldi, M., & Gerhard, O. (2011). The unmixed kinematics and origins of diffuse stellar light in the core of the Hydra I cluster (Abell 1060). *A&A*, 528:A24.

Gonçalves, D. R., Teodorescu, A. M., Alves-Brito, A., Méndez, R. H., & Magrini, L. (2012). A kinematic study of planetary nebulae in the dwarf irregular galaxy IC10. *MNRAS*, 425:2557–2566.

McNeil-Moylan, E. K., Freeman, K. C., Arnaboldi, M., & Gerhard, O. E. (2012). Planetary nebula kinematics in NGC 1316: a young Sombrero. *A&A*, 539:A11.

Ott, J., Stilp, A. M., Warren, S. R., Skillman, E. D., Dalcanton, J. J., Walter, F., de Blok, W. J. G., Koribalski, B., & West, A. A. (2012). VLA-ANGST: A High-resolution H I Survey of Nearby Dwarf Galaxies. *AJ*, 144:123.

Carignan, C., Frank, B. S., Hess, K. M., Lucero, D. M., Randriamampandry, T. H., Goedhart, S., & Passmoor, S. S. (2013). KAT-7 Science Verification: Using H I

Observations of NGC 3109 to Understand its Kinematics and Mass Distribution. *AJ*, 146:48.

Stasińska, G., Peña, M., Bresolin, F., & Tsamis, Y. G. (2013). Planetary nebulae and H ii regions in the spiral galaxy NGC 300. Clues on the evolution of abundance gradients and on AGB nucleosynthesis. *A&A*, 552:A12.

Pereyra, M., Richer, M. G., & López, J. A. (2013). The Deceleration of Nebular Shells in Evolved Planetary Nebulae. *ApJ*, 771:114.

Ventura, P., Di Criscienzo, M., Carini, R., & D'Antona, F. (2013). Yields of AGB and SAGB models with chemistry of low- and high-metallicity globular clusters. *MNRAS*, 431:3642–3653.

Ventura, P., Dell'Agli, F., Schneider, R., Di Criscienzo, M., Rossi, C., La Franca, F., Gallerani, S., & Valiante, R. (2014). Dust from asymptotic giant branch stars: relevant factors and modelling uncertainties. *MNRAS*, 439:977–989.

Fishlock, C. K., Karakas, A. I., Lugaro, M., & Yong, D. (2014). Evolution and Nucleosynthesis of Asymptotic Giant Branch Stellar Models of Low Metallicity. *ApJ*, 797:44.

Delgado-Inglada, G., Morisset, C., & Stasińska, G. (2014). Ionization correction factors for planetary nebulae - I. Using optical spectra. *MNRAS*, 440:536–554.

Hwang, N., Park, H. S., Lee, M. G., Lim, S., Hodge, P. W., Kim, S. C., Miller, B., & Weisz, D. (2014). Spectroscopic Study of Extended Star Clusters in Dwarf Galaxy NGC 6822. *ApJ*, 783:49.

Ventura, P., Criscienzo, M. D., D'Antona, F., Vesperini, E., Tailo, M., Dell'Agli, F., & D'Ercole, A. (2014). The formation of multiple populations in the globular cluster 47 Tuc. *MNRAS*, 437:3274–3282.

Magrini, L., Coccato, L., Stanghellini, L., Casasola, V., & Galli, D. (2016). Metallicity gradients in local Universe galaxies: Time evolution and effects of radial migration. *A&A*, 588:A91.

Kreckel, K., Groves, B., Bigiel, F., Blanc, G. A., Kruijssen, J. M. D., Hughes, A., Schruba, A., & Schinnerer, E. (2017). A Revised Planetary Nebula Luminosity Function Distance to NGC 628 Using MUSE. *ApJ*, 834:174.